Earth-Science Reviews 268 (2025) 105169

Contents lists available at ScienceDirect

Earth-Science Reviews

journal homepage: www.elsevier.com/locate/earscirev

Foundational uncertainties in terminal Ediacaran chronostratigraphy revealed by high-precision zircon U-Pb geochronology of the Nama Group, Namibia

Fred T. Bowyer [a,b,*,1], Fabio Messori [c], Rachel Wood [b], Ulf Linnemann [d], Esther Rojo-Perez [d], Mandy Zieger-Hofmann [d], Johannes Zieger [d], Junias Ndeunyema [e], Martin Shipanga [e], Bontle Mataboge [f], Dan Condon [g], Catherine V. Rose [h], Collen-Issia Uahengo [e], Sean P. Gaynor [c,i], Inigo A. Müller [c,j], Gerd Geyer [k], Torsten Vennemann [l], Joshua H.F.L. Davies [m], Maria Ovtcharova [c,**,1]

[a] School of Earth and Environment, University of Leeds, Woodhouse Lane, Leeds LS2 9JT, UK
[b] School of GeoSciences, University of Edinburgh, James Hutton Road, Edinburgh EH9 3FE, UK
[c] Department of Earth Sciences, University of Geneva, CH-1205 Geneva, Switzerland
[d] Senckenberg Naturhistorische Sammlungen Dresden, Museum für Mineralogie und Geologie, GeoPlasmaLab, Königsbücker Landstraße 159, D-01109 Dresden, Germany
[e] Department of Geosciences, University of Namibia, Keetmanshoop, Namibia
[f] Department of Geological Sciences, University of Cape Town, Cape Town, South Africa
[g] British Geological Survey, Keyworth NG12 5GG, UK
[h] School of Earth and Environmental Sciences, University of St Andrews, KY16 9TS, UK
[i] United States Geological Survey, Geology, Geophysics & Geochemistry Science Center, Denver, CO, United States of America
[j] AMGC Group, Vrije Universiteit Brussel, 1050 Brussels, Belgium
[k] Institut für Geographie und Geologie, Universität Würzburg, 97074 Würzburg, Germany
[l] Institute of Earth Surface Dynamics, University of Lausanne, 1015 Dorigny, Switzerland
[m] Département des Sciences de la Terre et de l'Atmosphère/Geotop, Université du Québec à Montréal, QC H3C 3PA, Canada

ARTICLE INFO

Keywords:
Ediacaran
Geochronology
Zircon U-Pb CA-ID-TIMS
Nama Group
Namibia

ABSTRACT

The Nama Group of southern Namibia and northwestern South Africa hosts the best-dated mixed carbonate-siliciclastic foreland basin succession of the terminal Ediacaran [ca. 551 million years (Ma) ago to <538 Ma] and is key for resolving the chronology of early metazoan evolution. Numerous silicified volcanic tuff interbeds are present, but differing interpretations regarding the fidelity of their ages lead to different regional stratigraphic correlations, especially for the Urusis Formation of the Schwarzrand Subgroup. An expanded record of the Urusis Formation is found in the Swartpunt area of southern Namibia, which has yielded an important metazoan biota. But the succession in this area is preserved as a series of thrusts at the leading edge of the Gariep orogenic belt and zircon U-Pb data show systematic age repetition. We use regional stratigraphic and structural mapping, integrated with carbonate carbon isotope ($\delta^{13}C_{carb}$) chemostratigraphy and high-precision radioisotope U-Pb zircon geochronology from outcrop and recently acquired drill core to develop a temporally calibrated basin-wide depositional model. This integrated dataset either reflects complex zircon reworking, inheritance, or potential analytical biases (Scenario 1) or the presence of a Gariep-related cryptic décollement within the Spitskop Member that has resulted in stratigraphic repetition (Scenario 2). We investigate the evidence for and against both scenarios and consider their implications for stratigraphic and $\delta^{13}C_{carb}$ correlations between the Swartpunt area and coeval exposures along the Orange River border with South Africa.

Given that these issues are in an area that hosts numerous silicified ash beds and extensive exposure, an inability to confidently discount either scenario highlights a level of compounding uncertainty in zircon U-Pb geochronology that must be considered when attempting to build global chronostratigraphic frameworks.

* Corresponding author at: School of Earth and Environment, University of Leeds, Woodhouse Lane, Leeds LS2 9JT, UK.
** Corresponding author.
E-mail addresses: f.t.bowyer@leeds.ac.uk (F.T. Bowyer), maria.ovtcharova@unige.ch (M. Ovtcharova).
[1] These authors contributed equally to this work.

https://doi.org/10.1016/j.earscirev.2025.105169
Received 7 February 2025; Received in revised form 18 May 2025; Accepted 20 May 2025
Available online 23 May 2025

Scenario 1 implies that some of the weighted mean ages and Bayesian eruption ages from the Swartpunt area may be >1 Myr older than the depositional age of their respective ash beds when assuming existing stratigraphic correlations. If this scenario is preferred, then a cautious approach would be to consider all weighted mean zircon U-Pb ages from ash beds to reflect maximum depositional ages. Both scenarios support deposition of the Huns Member >540 Ma in the Swartpunt area if the oldest weighted mean age reported here represents a near-depositional age, which has significant implications for the temporal calibration of important terminal Ediacaran ichnofossil assemblages and future cyclostratigraphic studies.

Stratigraphic correlations common to both scenarios allow us to temporally calibrate a basin evolution model for the Nama Group. Temporal trends in initial hafnium isotope (εHf) compositions of zircon grains from ash beds throughout the succession may support progressive crustal thickening associated with underplating of the Damara orogenic belt along the northern periphery of the Kalahari craton from ca. 547 Ma to ca. 538 Ma. The compilation of new and published zircon U-Pb ages may also imply that the locus of carbonate platform development migrated from north to south (present co-ordinates), tracking the migration of foredeep subsidence.

Contents

1. Introduction

The terminal Ediacaran to earliest Cambrian (ca. 551–532 million years ago, Ma) encompasses a critical interval of early metazoan evolution (Fig. 1). Marine sedimentary rocks of this age record the disappearance of the soft-bodied 'Ediacara biota' alongside the majority of biomineralizing Ediacaran taxa, the appearance of Cambrian-type small shelly fossils (SSFs), and an increase in ichnofossil diversity and bioturbation intensity (e.g., Fedonkin et al., 2007; Wilson et al., 2012; Zhu et al., 2017; Cribb et al., 2019; Darroch et al., 2021, 2023; Topper et al., 2022; Turk et al., 2022; Nelson et al., 2023). Several hypotheses to explain the sequence of last and first appearances of biota across this interval have been proposed, and include a mass extinction of the Ediacara biota driven by external, environmental stressors or a combination of environmental and ecological drivers with protracted biotic replacement, or a series of successive but transitional biotic radiations without catastrophic mass extinction (Knoll and Carroll, 1999; Zhu et al., 2017; Darroch et al., 2018, 2023; Wood et al., 2019). At least two chronostratigraphic frameworks exist across the Ediacaran-Cambrian transition based on differing durations for the globally recognized 'Basal Cambrian negative carbon isotope excursion' (BACE; Fig. 1), resulting in different maximum extinction/origination rates calculated using estimates of mean generic richness from fossil range-through data (e.g., Bowyer et al., 2024).

Greater than fifty years of research incorporating litho-, chemo-, tectono- and sequence stratigraphic, sedimentological, paleontological, and high-precision geochronological investigations have resulted in the Nama Group, of Namibia and South Africa, being the most temporally well-constrained mixed carbonate-siliciclastic succession of the entire Ediacaran Period (Figs. 1–3, Germs, 1972, 1983; Gresse and Germs, 1993; Grotzinger et al., 1995; Saylor et al., 1995, 1998, 2005; Saylor, 1996, 2003; Narbonne et al., 1997; Jensen et al., 2000; Wood et al., 2015; Linnemann et al., 2019; Nelson et al., 2022; O'Connell et al., 2025). Marine sedimentary rocks of the Nama Group host body and trace fossils that document a fundamental macroevolutionary transition across the terminal Ediacaran to earliest Cambrian interval (e.g., Germs, 1983; Wilson et al., 2012). Near-complete exposure of the Nama Group succession over >30,000 km^2 (Fig. 2A), in addition to the occurrence of numerous volcanic ash interbeds suitable for U-Pb zircon geochronology (Fig. 3), have allowed for an unparalleled understanding of Ediacaran to Cambrian paleoenvironmental conditions and basin evolution (e.g., Kröner and Germs, 1971; Germs, 1972, 1983; Gong et al., 2025; Grotzinger et al., 1995; Saylor et al., 1995, 1998; Saylor, 1996, 2003; Saylor and Grotzinger, 1996; Narbonne et al., 1997; O'Connell et al., 2025; Jensen et al., 2000; Darroch et al., 2015, 2021; Wood et al., 2015, 2023; Buatois et al., 2018; Cribb et al., 2019; Linnemann et al., 2019; Nelson et al., 2022; Bowyer et al., 2023; Spiering et al., 2023). In particular, the mixed carbonate-siliciclastic Urusis Formation of the Nama Group has yielded a significant $\delta^{13}C_{carb}$, $^{87}Sr/^{86}Sr$ and paleontological dataset, which has been well constrained by U-Pb geochronology and used to determine a maximum date of ca. 539–538 Ma for onset of the BACE (Fig. 1; Saylor et al., 1998; Zhu et al., 2006; Wood et al., 2015; Linnemann et al., 2019; Bowyer et al., 2022; Nelson et al., 2022; Mtonda et al., 2024). As a result, the Urusis Formation is a key reference succession for terminal Ediacaran chronostratigraphy.

Attempts to reduce chronostratigraphic uncertainty across this interval require fully integrated chemostratigraphic and fossil occurrence datasets to be calibrated in time by high-precision radioisotopic ages (Bowring et al., 2007; Maloof et al., 2010a, 2010b; Smith et al., 2016; Parry et al., 2017; Linnemann et al., 2019; Hodgin et al., 2020; Nelson et al., 2022, 2023; Topper et al., 2022; Bowyer et al., 2022, 2023, 2024). Methodological refinements in U-Pb ID-TIMS (isotope dilution-thermal ionization mass spectrometry) geochronology over the past two decades, such as the improvement of zircon chemical abrasion (CA-ID-TIMS) procedures (Mattinson, 2005; Widmann et al., 2019; McKanna et al., 2022) and calibration of a globally shared EARTHTIME tracer solution (Condon et al., 2015), have led to unprecedented precision and accuracy, yielding weighted mean $^{206}Pb/^{238}U$ ages with uncertainties of ±0.05 % or less (Schaltegger et al., 2015). Accurate correlation of global records first requires that regional datasets are interpreted within holistic frameworks that combine lithostratigraphic with tectonostratigraphic data to inform models of *syn*-depositional basin evolution and post-depositional structural evolution. Within these frameworks, the fidelity of associated U-Pb ages to reflect maximum depositional ages for zircon-bearing interbeds is also fundamentally important when attempting to constrain rates of change in the co-evolution of life and environment.

Here, we report new zircon U-Pb CA-ID-TIMS ages and zircon

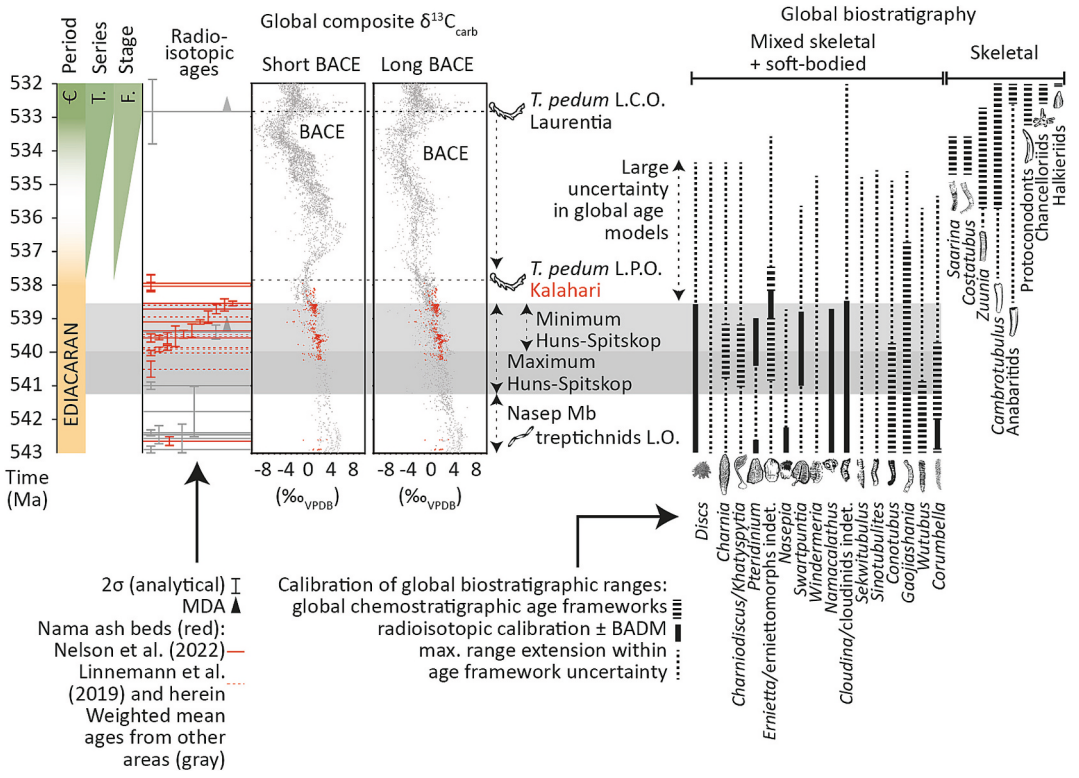

Fig. 1. Global chronostratigraphy across the terminal Ediacaran to earliest Cambrian interval (543–532 Ma). Global $\delta^{13}C_{carb}$ chemostratigraphic age framework and calibrated fossil occurrence information for 'short BACE' model after Bowyer et al. (2023) and Nelson et al. (2022). 'Long BACE' model is provided herein and remains consistent with all published radioisotopic ages. Age for global lowest calibrated occurrence (LCO) of *Treptichnus pedum* after Nelson et al. (2023). Radioisotopic ages (after Bowring et al., 2007; Parry et al., 2017; Linnemann et al., 2019; Hodgin et al., 2020; Nelson et al., 2022, 2023, and herein). Gray data points and radioisotopic ages correspond to the global compilation and age framework of Bowyer et al. (2023), while red data points and radioisotopic ages correspond to Nama Group data compilation herein (multiple sources referenced throughout text). BACE – 'Basal Cambrian negative carbon isotope excursion'. MDA – maximum depositional age. LPO – Lowest possible occurrence (based on the absence of *T. pedum* from the informal 'lower' Nomtsas Formation of the NNP, after Nelson et al., 2022). LO – lowest occurrence of treptichnids in the Nama Group after Darroch et al. (2021 and references therein). BADM – Bayesian age-depth model for the Neint Nababeep Plateau (NNP) after Nelson et al. (2022). T. – Terreneuvian Series; F. – Fortunian Stage. Fossil symbols after Bowyer et al. (2023). Mb. – Member. (For interpretation of the references to colour in this figure legend, the reader is referred to the web version of this article.)

hafnium (Hf) isotope compositions from nine volcanic tuff interbeds in three Nama Group study areas in southern Namibia (Fig. 2A–D). We also report $\delta^{13}C_{carb}$ chemostratigraphic data from outcrop and drill core, integrated with stratigraphic and structural observations from regional geological mapping. These new data are considered within models that reconstruct carbonate platform and post-depositional tectonostratigraphic evolution to explore the potential influence of reworking and/or tectonic repetition on each ash bed, in addition to zircon provenance from, and development of, proximal orogenic belts (e.g., the Damara orogenic belt). The overall goal of this study is to help clarify uncertainties in our understanding of the tempo of metazoan evolution in the terminal Ediacaran, which may be reduced through

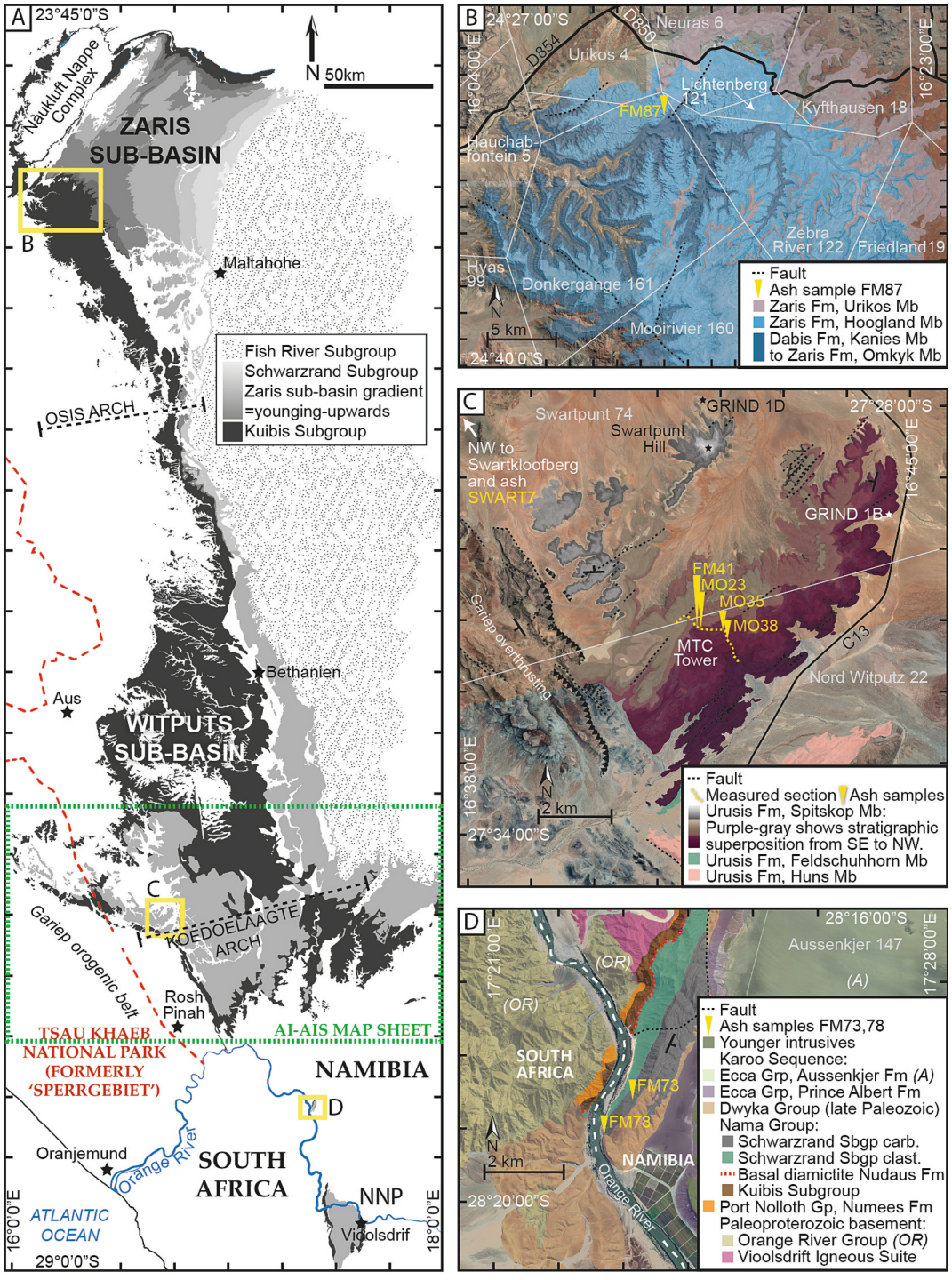

Fig. 2. Geological setting of the Nama Group in southern Namibia and northwestern South Africa. **(A)** The Ediacaran-aged Kuibis and Schwarzrand Subgroups of the Nama Group, showing the areal extent of the Zaris and Witputs sub-basins, sections along the Orange River and regional context of studied areas (modified after Bowyer et al., 2023). NNP: Neint Nababeep Plateau. **(B)** Geological map showing the regional context of the ash bed in the lower Hoogland Member, and position of the sample analyzed in this study (modified after Supplementary Materials of Bowyer et al., 2023). **(C)** Geological map of the Urusis Formation in the vicinity of MTC Tower and Swartpunt Hill, showing the positions of sampled ash beds (discussed further in Sections 4 and 5). **(D)** Geological map of the Aussenkjer section on the Orange River border between Namibia and South Africa, showing the position of sampled ash beds (geological map modified and updated after Kröner and Germs, 1971). White labels and lines indicate farm names and boundaries, respectively. Grp. – Group; Sbgp. – Subgroup; Fm. – Formation; Mb. – Member.

future targeted studies.

2. Geological Background

2.1. The Nama Group: subdivision, tectonic setting and summarized paleontology

The Nama Group is a late Ediacaran to earliest Cambrian (ca. 551 Ma to <538 Ma) mixed carbonate-siliciclastic, fluvio-deltaic to open shallow marine succession that was deposited on basement of the Kalahari craton in an active foreland basin setting (Germs, 1983; Saylor et al., 1998; Nelson et al., 2022). The Nama foreland developed in response to compressional stress associated with the collision of the Congo and Kalahari cratons along the Damara orogenic belt to the present north, and incipient flexure associated with the onset of collision between the Kalahari and Rio de la Plata cratons along the Gariep orogen to the present southwest (Germs, 1983; Germs and Gresse, 1991; Gresse and Germs, 1993). Basement forebulges created by active orogenic compression formed paleobathymetric highs in the Nama foreland (Germs, 1983). These include the 'Osis Arch', which separated the Zaris sub-basin from the Witputs sub-basin to varying degrees throughout Nama deposition (Fig. 2A) and the 'Koedoelaagte Arch', which may have formed within the Witputs sub-basin before deposition of the Early Cambrian Fish River Subgroup (Fig. 2A, Kröner and Germs, 1971; Germs and Gresse, 1991; Gresse and Germs, 1993; Germs et al., 2009; Nelson et al., 2022). Subsequent erosion has resulted in widespread removal of the Nama succession between the outcrops of the Ai-Ais map sheet area and sections along the Orange River (Fig. 2A).

Stratigraphic correlations across the Osis Arch through detailed geological mapping and measured section correlation has informed sequence stratigraphy and $\delta^{13}C_{carb}$ chemostratigraphy of the Nama Group (Grotzinger et al., 1995; Saylor et al., 1995, 1998; Bowring et al., 2007; Linnemann et al., 2019; Maloney et al., 2020; Nelson et al., 2022). Due to the absence of laterally traceable units, stratigraphic correlation between the Swartpunt area and the Neint Nababeep Plateau (NNP) is based on lithostratigraphic thicknesses and sequence similarity, as well as $\delta^{13}C_{carb}$ chemostratigraphy and geochronology of volcanic ash interbeds (Fig. 3, Kröner and Germs, 1971; Germs and Gresse, 1991; Gresse and Germs, 1993; Nelson et al., 2022). Differences in the thicknesses of measured sections are interpreted to reflect distance from the Kalahari craton and basement forebulges, in addition to temporally variable rates of active tectonic subsidence within and between each sub-basin (Germs, 1983; Gresse and Germs, 1993; Saylor, 2003).

The Nama Group is subdivided, in ascending order, into the Kuibis, Schwarzrand and Fish River Subgroups (Figs. 3, S1 and S2, Germs, 1983). The Kuibis and Schwarzrand Subgroups are dominantly late Ediacaran in age, and contain fossils of Ediacaran soft-bodied rangeomorphs, erniettomorphs and numerous problematica that are mostly

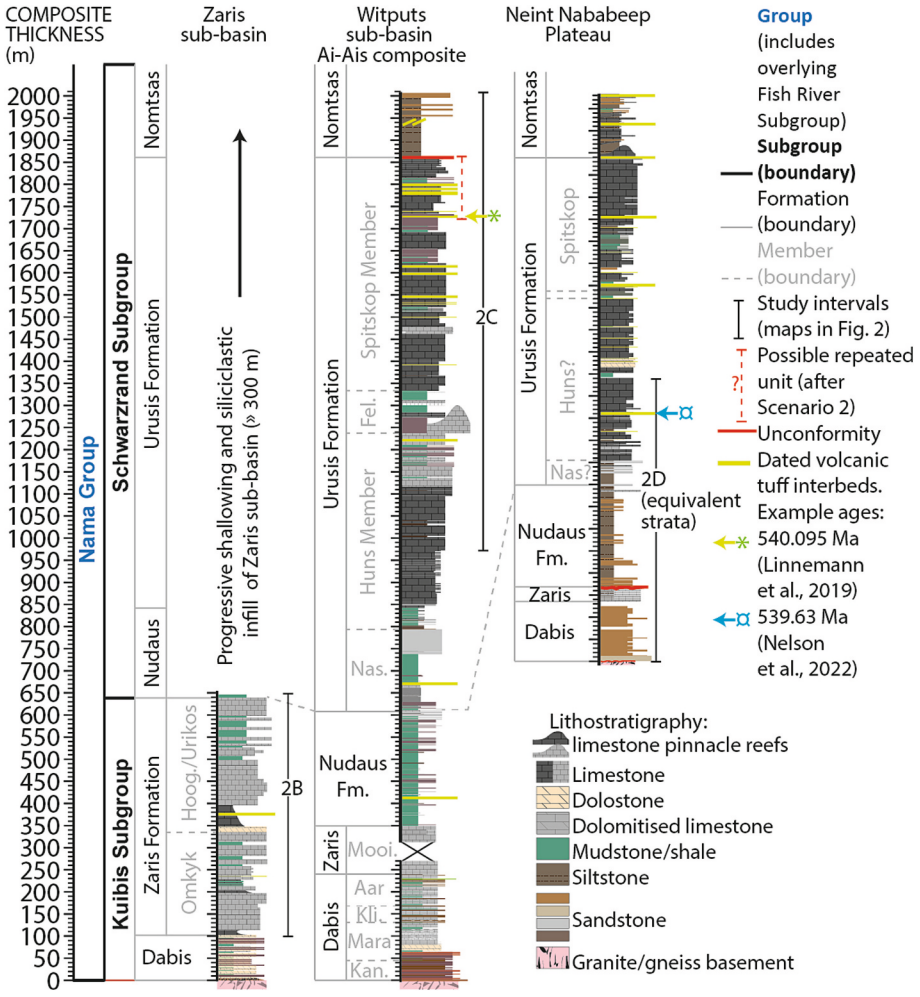

Fig. 3. Composite stratigraphic columns for the Zaris sub-basin, Ai-Ais map sheet area of the Witputs sub-basin, and sections of the Orange River (simplified after Fig. S1). Member subdivision of the Urusis Formation in the Orange River succession follows Nelson et al. (2022). Maximum thickness of the Ai-Ais composite of the Witputs sub-basin follows 'Scenario 1' (i.e., no stratigraphic repetition, see discussion). Hoog. – Hoogland Member, Kan. – Kanies Member, Kli. – Kliphoek Member, Mooi. – Mooifontein Member, Nas. – Nasep Member, Fel. – Feldschuhhorn Member. Fm. – Formation; Mb. – Member.

preserved in siliciclastic rocks (Gürich, 1930a, 1930b, 1933; Pflug, 1966, 1970; Germs, 1973; Hahn and Pflug, 1985; Narbonne et al., 1997; Grazhdankin and Seilacher, 2002; Elliott et al., 2011, 2016; Hall et al., 2013; Vickers-Rich et al., 2013; Meyer et al., 2014; Nelson et al., 2022; Wood et al., 2023; Runnegar et al., 2024). Tubular cloudinids, which distinguish the eponymous terminal Ediacaran 'Nama assemblage' (Wood et al., 2023), include the skeletal *Cloudina* in carbonates hosted in the lower part of the Kuibis to upper part of the Schwarzrand Subgroups (Germs, 1972; Penny et al., 2014; Kaufman et al., 2019; Nelson et al., 2022; Bowyer et al., 2023), and siliciclastic-hosted *Corumbella* in the middle interval of the Schwarzrand Subgroup (Turk et al., 2022). Schwarzrand Subgroup siliciclastic rocks also preserve an important ichnofossil assemblage that records an increase in terminal Ediacaran bioturbation intensity and increasingly diverse styles of animal-substrate interaction (Buatois et al., 2018; Cribb et al., 2019; Darroch et al., 2021; Turk et al., 2022, 2024).

Sedimentary rocks of the Kuibis Subgroup document a diachronous marine transgression across the Kalahari basement, with initial fluvio-deltaic to shallow subtidal siliciclastic-dominated facies locally giving way to semi-restricted carbonate facies, and finally to open shallow marine carbonate facies and laterally correlative siliciclastic rocks (Saylor et al., 1995; Maloney et al., 2020). This subgroup is subdivided into the Dabis Formation and overlying Zaris Formation (Fig. 3), which together comprise at least two large-scale depositional sequences, often with coarse siliciclastic-dominated lowstand deposits, mixed carbonate and fine grained siliciclastic-dominated transgressive deposits and carbonate-dominated highstand deposits (Fig. S1, Saylor et al., 1995; O'Connell et al., 2025).

Three scales of sequences have been identified in the Nama Group succession that range from less than one to ten meters (small-scale sequence), several tens of meters (medium-scale sequence), to up to hundreds of meters in thickness (large-scale sequence, Saylor, 2003; Spiering et al., 2023). Given that these sequences represent deposition within an active tectonic setting, assessing depositional duration from relative thickness is complicated through intervals of the succession that lack bracketing radioisotopic ages. However, based on currently available global chronostratigraphic frameworks (e.g., Bowyer et al., 2024), the large-scale sequences of the Kuibis Subgroup may each represent up to 2 million years of deposition, while medium-scale sequences may represent on the order of a few hundred thousand years of deposition. However, for the Kuibis Subgroup, these estimates rely upon extrapolation of radioisotopic ages and carbon isotope chemostratigraphic correlation between globally distributed regions, which remains speculative.

In the Witputs sub-basin the Dabis Formation is subdivided into the Kanies, Mara, Kliphoek and Aar Members, while the Zaris Formation is represented by the Mooifontein Member (Fig. 3, Germs, 1983; Saylor et al., 1995; Hall et al., 2013). Here, the first large-scale sequence of the Kuibis Subgroup comprises, in stratigraphic order: pebble conglomerate, sandstone and siltstone of the Kanies Member; siltstone and mudstone of the lowermost part of the Mara Member, deposited in a marine environment during early transgression; dolostone and dolomitic limestone of the middle part of the Mara Member; and the limestone-dominated upper part of the Mara Member (Saylor et al., 1995; Bowyer et al., 2023). The upper part of the Mara Member contains a nested medium-scale sequence, informally termed the Pockenbank Member (Fig. S1, Kaufman et al., 2019). The second large-scale sequence comprises siltstone, sandstone and quartzite (occasionally with limestone interbeds) of the lowstand Kliphoek Member; interbedded sandstone, shale, limestone and subordinate dolostone of the transgressive Aar Member; and dark gray to black limestone of the Mooifontein Member (Saylor et al., 1995; Hall et al., 2013; O'Connell et al., 2025).

In the Zaris sub-basin, the Dabis Formation is commonly represented by a unit of pebble conglomerate and coarse siliciclastic rocks assigned to the Kanies Member but regionally includes an overlying unit of Mara Member-equivalent dolostone in more distal sections (e.g., Brak, Fig. S1; Wood et al., 2015). The overlying Zaris Formation is more extensive in the Zaris sub-basin relative to the Witputs sub-basin and consists of open marine inner-mid ramp carbonate platform deposits of the Omkyk and Hoogland Members, and outer ramp siliciclastics of the Urikos Member (Figs. 3, S1; Smith, 1999; Adams et al., 2004, 2005; Dibenedetto and Grotzinger, 2005). Sequence stratigraphic and $\delta^{13}C_{carb}$ chemostratigraphic studies suggest that the Omkyk Member correlates with the Aar-Mooifontein Members of the Witputs sub-basin, while carbonate deposits correlative to the Hoogland Member are largely absent from the Witputs sub-basin (Fig. S1; Saylor et al., 1995). The spatial distribution of Kuibis Subgroup carbonate deposition between the Zaris and Witputs sub-basins is thought to reflect relative proximity within and between sub-basins to the loci of flexural foredeep subsidence and forebulge uplift (Germs and Gresse, 1991).

The Schwarzrand Subgroup is subdivided into the siliciclastic-dominated Nudaus Formation (Niederhagen and Vingerbreek Members), the mixed siliciclastic-carbonate Urusis Formation (siliciclastic-dominated Nasep Member, carbonate-dominated Huns Member, siliciclastic-dominated Feldschuhhorn Member and mixed siliciclastic-carbonate Spitskop Member), and the siliciclastic-dominated Nomtsas Formation (Fig. 3; Germs, 1983; Saylor et al., 1995). In the Zaris sub-basin, the Schwarzrand Subgroup is dominantly siliciclastic due to weathering and erosion of both the Kalahari craton and additional input associated with gradual unroofing of the Damara hinterland, which led to shallowing and sub-basin infill (Germs, 1983). However, carbonate deposition corresponding to the Urusis Formation continued in the Witputs sub-basin from <542.65 Ma until ca. 538.6 Ma, during pulsed accommodation increase driven by active tectonic subsidence in addition to intervals of eustatic sea level rise (Saylor, 2003; Nelson et al., 2022).

The informal 'upper' Nomtsas Formation in the Witputs sub-basin hosts the lowest regional occurrence of the Early Cambrian ichnofossil *Treptichnus pedum* (e.g., Wilson et al., 2012) above an erosive unconformity. A tentative maximum age of ≤538 Ma for this occurrence (and possibly for the global first appearance) is based on the youngest U-Pb zircon age from an ash bed within the informal 'lower' Nomtsas Formation near Vioolsdrif, where *T. pedum* is absent (Fig. 1, Nelson et al., 2022). A Cambrian age for fluvial to shallow-marine siliciclastic rocks of the overlying Fish River Subgroup is confirmed by their associated ichnofossil assemblages (Geyer, 2005).

2.2. The stratigraphic position of Urusis Formation ash beds in the Swartpunt area

In the Witputs sub-basin (Fig. 4), numerous measured sections of the Urusis Formation, from the landward margin in the east, through the depocenter to the seaward margin in the west, reveal a series of stratal stacking patterns that have informed sequence stratigraphic subdivision into a nested series of unconformity-bounded depositional sequences (Fig. 5A, Saylor, 2003). Five large-scale sequences (A–E) are distinguished, with further subdivision of sequences B-E into eighteen medium-scale sequences (B1–3, C4–9, D10–12, and E13–18), and numerous small-scale sequences (Fig. 5A, Saylor, 2003). Large-scale sequences broadly distinguish member subdivision of the Urusis Formation, whereby sequence A corresponds to the siliciclastic-dominated Nasep Member, sequences B and C to the carbonate-dominated Huns Member, sequence D to the siliciclastic-dominated Feldschuhhorn Member and carbonate-dominated lower part of the Spitskop Member, and sequence E to the mixed carbonate-siliciclastic middle-upper part of the Spitskop Member (Fig. 5A, Saylor, 2003). Medium-scale sequences define shallowing-upwards cycles, commonly with siliciclastic bases and carbonate tops (Saylor et al., 1995; Saylor, 2003), that have recently been used for initial cyclostratigraphic study of the Schwarzrand Subgroup (Spiering et al., 2023). A minimum of twelve silicified volcanic tuff deposits are interbedded within E13–E18.

However, in the vicinity of farms Swartkloofberg, Swartpunt and

Nord Witputz, exposure of stratigraphic sections that reveal these sequences is complicated by structural dissection (Figs. 4B, 5B). This area hosts a series of major northwest-southeast striking thrust faults that record northeast-vergent compression driven by the Gariep orogeny (Fig. 4B, Saylor, 1993; Saylor and Grotzinger, 1996). A major thrust fault, traceable in outcrop over >100 km, separates what has been termed the 'lower thrust plate' (LTP) in the Swartpunt area, from the Nama autochthon to the east (Figs. 4B, 5B). Allochthonous thrust blocks to the west of this dividing fault record sequential out-of-sequence overthrusting of the LTP by what was defined as the 'middle thrust plate' (MTP) and, finally the 'upper thrust plate' (UTP, Saylor and Grotzinger, 1996). While progressive thrusting and erosion have removed the Feldschuhhorn and Spitskop Members and Nomtsas Formation from most of the UTP, these units are preserved, to varying degree, in both the MTP and LTP successions (Figs. 4B, 5B). Displacements along fault planes that separate each thrust plate have been estimated to have been on the order of 1–3 km based on hanging wall cut-offs and anticlines for specific lithological units (Saylor and Grotzinger, 1996).

2.3. Existing Nama Group geochronology

High-precision U-Pb zircon geochronology from volcanic ash beds has been used to determine the age of the Ediacaran stratigraphy of Namibia, and then subsequently used to aid correlation of lithostratigraphic units between separate Nama Group exposures, to better understand the evolution of this biota and geology. Early geochronological investigations in the vicinity of farms Nord Witputz, Swartpunt and Swartkloofberg used zircon U-Pb air abrasion ID-TIMS (Grotzinger et al., 1995), but these data have since been superseded by analyses pretreated with chemical abrasion (CA-ID-TIMS), as this technique is much better at removing domains of Pb-loss and therefore produces more accurate data. While considering such data throughout this manuscript, we discuss all uncertainties at the 95 % confidence level, and largely report them in *X/Y/Z* format (Schoene et al., 2006), where *X* represents the internal/analytical uncertainty, *Y* represents *X* plus the tracer calibration uncertainty, and *Z* incorporates *Y* plus the ^{238}U decay constant uncertainty of Jaffey et al. (1971).

However, increased publication of high-precision geochronology data and their resulting interpretations, compounded by the more precise analytical data via more analytically advanced measurements, have created a complicated suite of interpretations for Nama Group chronostratigraphy. This is exemplified by the correlation of the Urusis Formation between the Ai-Ais map sheet area and exposures along the Orange River, further south (Figs. 2 and 3). The Urusis Formation is subdivided, in ascending order, into the Nasep, Huns, Feldschuhhorn and Spitskop Members, and is overlain by the Nomtsas Formation (Fig. 3). In the Witputs sub-basin near Swartpunt (Figs. 2A, C), deposition of the upper part of the Spitskop Member through Nomtsas Formation has been constrained between 540.095 ± 0.099 (0.17) [0.60] Ma and 538.58 ± 0.19 (0.24) [0.62] Ma (Linnemann et al., 2019). However, on the Neint Nababeep Plateau (Fig. 2A), the deposition of the lower part of the Huns Member through Nomtsas Formation is constrained between 539.63 ± 0.15 (0.27) [0.64] Ma and 537.95 ± 0.28 (0.36) [0.68] Ma (Nelson et al., 2022). In the Swartpunt area, the stratigraphic thickness between the base of the Huns Member and the 540.095 ± 0.099 Ma ash bed in the upper part of the Spitskop Member is >700 m (Figs. 3, S1 and S2). As a result, there is significant discrepancy in the absolute ages that constrain deposition of the lower part of the Huns Member through Spitskop Member between successions of the Swartpunt area and the Neint Nababeep Plateau, based on published lithostratigraphic correlation schemes that assume limited diachroneity between these two areas. Nelson et al. (2022) suggested that some, or

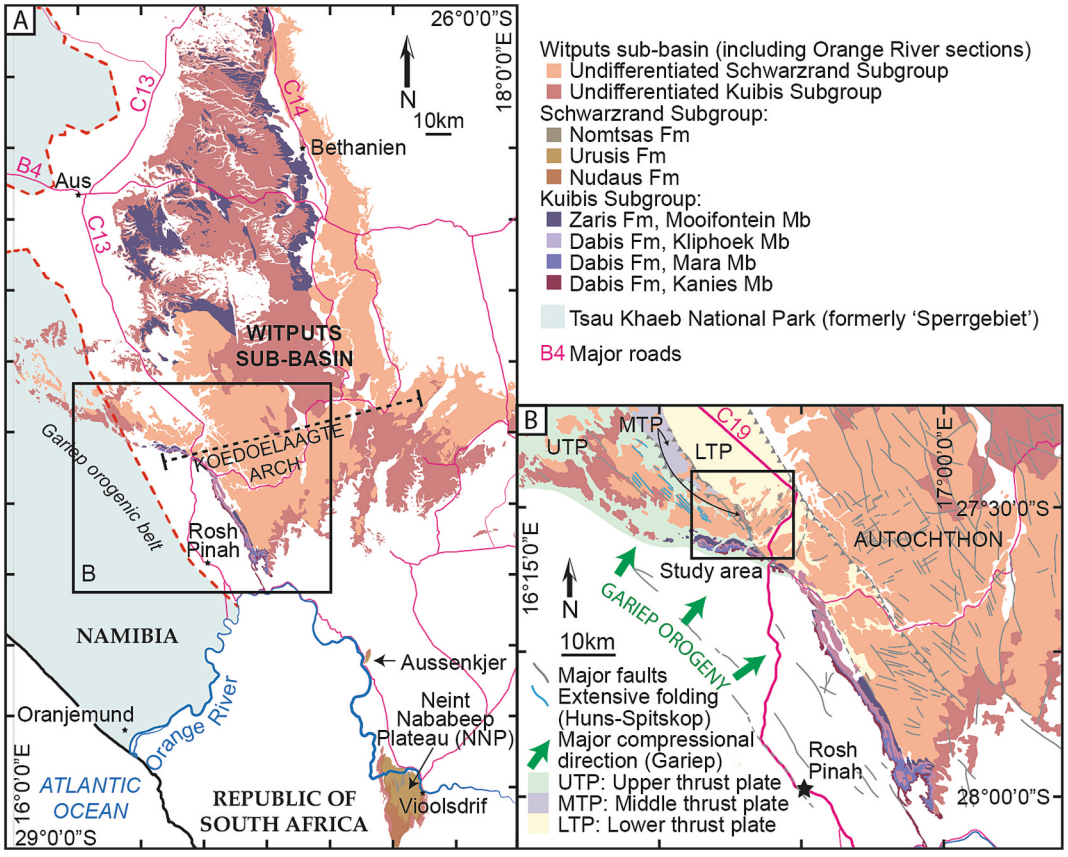

Fig. 4. **(A)** Simplified geological map of the Witputs sub-basin, modified after Bowyer et al. (2023), with map of the NNP after Nelson et al. (2022). **(B)** Expanded view, showing regional tectonostratigraphic context of the study area. UTP, MTP and LTP after Saylor and Grotzinger (1996). Fm. – Formation; Mb. – Member.

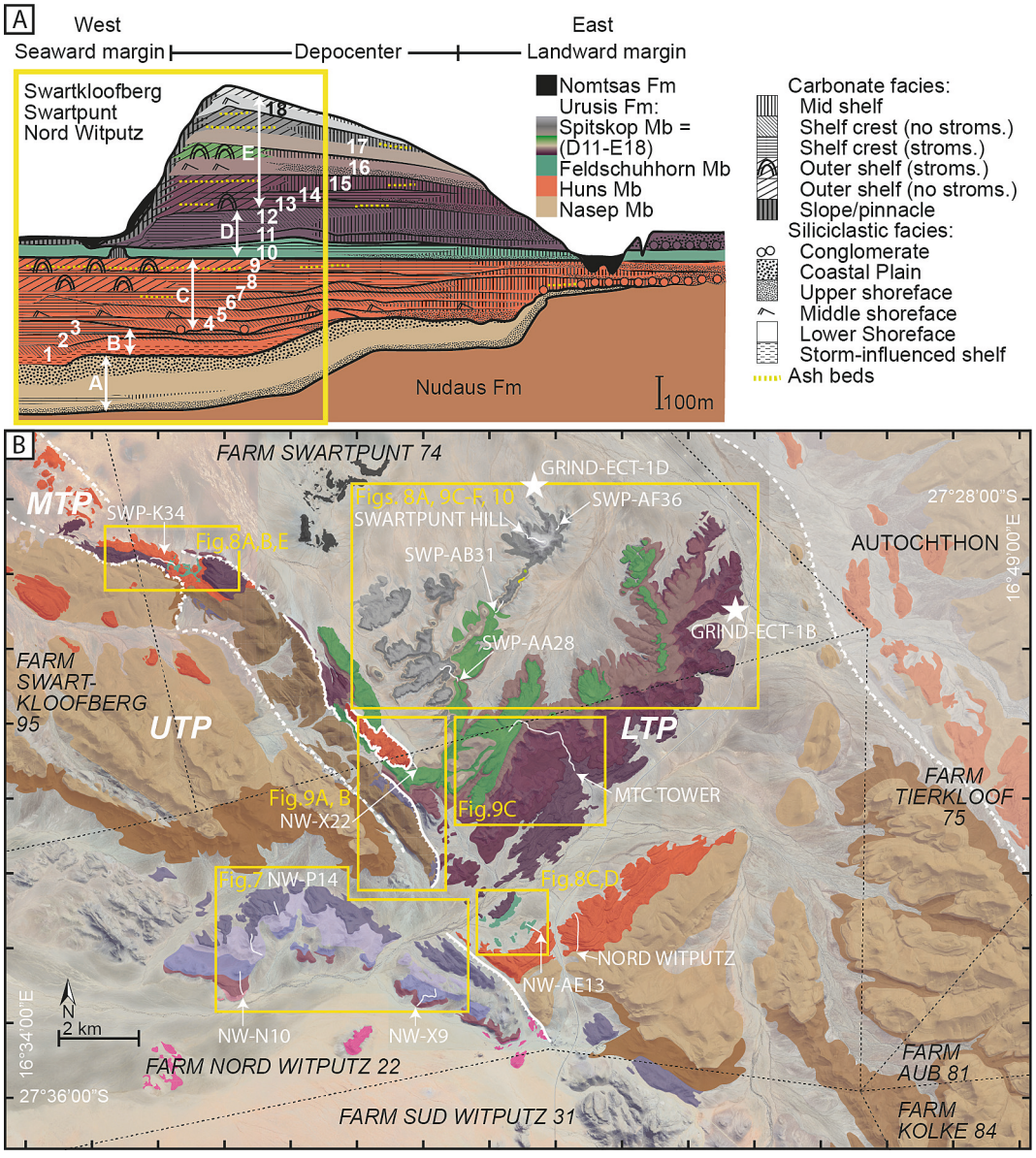

Fig. 5. **(A)** Schematic cross-section of the Nudaus Formation, Urusis Formation and Nomtsas Formation across the Witputs sub-basin, with large-scale (A–E) and medium-scale (1–18) depositional sequences, modified after Saylor (2003). Yellow box marks succession exposed in the vicinity of farms Swartkloofberg, Swartpunt and Nord Witputz. **(B)** Regional map of the study area, showing geological subdivision of the lower thrust plate after canonical model of stratigraphic superposition (e.g., Saylor and Grotzinger, 1996), consistent with 'Scenario 1' herein. Colour of individual formations and members, and colors of Spitskop Member subdivision, are the same between (A) and (B). Arrows point to the bases of measured sections. Key to colored units in (B) that stratigraphically underlie the Nudaus Formation is shown in Fig. 4. Fm. – Formation; Mb. – Member. (For interpretation of the references to colour in this figure legend, the reader is referred to the web version of this article.)

all, ages in the Urusis Formation of the Witputs sub-basin near Swartpunt (e.g., the 540.095 Ma ash bed dated by Linnemann et al., 2019) are maximum depositional ages, rather than the eruptive age of those ash beds. This may be the case if zircon populations in these ashes are dominated by reworked, older grains, and would imply that the youngest zircon grains in these ash beds have not be included in the age spectra from the data set of Linnemann et al. (2019). The possibility of ash bed ages in the Witputs sub-basin to be skewed by zircon reworking, without any reworking in other sub-basins, or the potential of interpretations based on zircon that do not represent the eruptive age of ash horizons, has led to uncertainty in the inter-basinal correlation scheme for the Nama Group.

3. Methods

We present new data from outcrop sections in three geographic areas that cover key stratigraphic intervals of the Kuibis and Schwarzrand Subgroups in the Zaris and Witputs sub-basins, including an isolated outcrop to the north of the NNP on the east (Namibian) side of the Orange River (Figs. 2–3, S1). We also present new data from one core of the International Continental Drilling Project 'GRIND-ECT' (Geological Research through Integrated Neoproterozoic Drilling – Ediacaran-Cambrian Transition, Rose et al., 2019).

3.1. Geological mapping, stratigraphic logging and sampling

Ash beds were collected at Donkergange and Aussenkjer using published measured section information (Figs. 2A, B, D, 6, Kröner and

Germs, 1971; Smith, 1999), but the main focus of our fieldwork was on farms Nord Witputz and Swartpunt (hereafter referred to as the 'Swartpunt area', farm numbers 22 and 74, respectively, Figs. 2C, 4, 5B). Sedimentary logging and geochemical sampling focused on measured sections in the UTP, MTP and LTP, with section measurements and samples systematically recorded through use of a folding meter stick. Fossils on float samples and exposed bedding planes were photographed in the field. We also present new data from ICDP GRIND-ECT drill core 1B, which covers a stratigraphic interval of the LTP (Fig. 5B). Geological mapping was carried out at various scales, both in the field and using observations from high-resolution satellite imagery (Google Earth, Maxar Technologies, and Sentinel-2). The results of mapping and measured sections are presented as composite lithostratigraphic profiles and field photographs (Figs. 6–10, S3–6), alongside a geological map superimposed upon a satellite image, and a regional structural cross-section (Fig. S7).

Carbonate samples (ca. 25–40 g) were collected in the field from measured sections SWP-K34 and MTC Tower (Fig. 5B) and sampled from GRIND-ECT core 1B at the core repository of the Bundesanstalt für Geowissenschaften und Rohstoffe, Berlin-Spandau, Germany. Sampling was undertaken at 0.5–10 m resolution through carbonate-dominated intervals of SWP-K34 and MTC Tower, and at 0.5–15 m resolution through carbonate-dominated intervals of core 1B and low-resolution data through the dominantly siliciclastic core 1A profile (Supplementary Materials). Sampling resolution was largely dictated by thickness of carbonate interbeds and the potential importance of target sections to infill data in understudied intervals of the Schwarzrand Subgroup record. Silicified volcanic tuff deposits range from 8 cm to >80 cm-thick in outcrop, and are identified by their blocky, weathering-resistant character, pale green-gray color on broken surfaces and buff-tan color on weathered surfaces (Fig. S3). In cores 1B and 1D, silicified ash beds are pale green-gray, often characterized by planar to wavy laminations with sharp bases and coarser lower intervals that fine upwards, and range from 1 cm to ca. 30 cm thick (Fig. S4).

Of the geochronology samples, the stratigraphically lowest sample was taken from an ash bed in the lower part of the Hoogland Member (sample FM87, Figs. 2B, S3A) at a section exposed on the northern edge of Farm Donkergange in the Zaris sub-basin (24° 30′ 26.7" S, 16° 12' 5.0" E, Figs. 2B, 3). The same ash bed was previously sampled from a neighboring section on Farm Donkergange to the southwest of our section and dated using air abrasion ID-TIMS by Grotzinger et al. (1995) and chemical abrasion ID-TIMS by Bowring et al. (2007).

We also present zircon geochronology for five ash beds in the area of farms Swartpunt and Nord Witputz. Four of these are from a measured outcrop section to the west of core 1B (MTC Tower, top of section: 27° 31′ 3.2" S, 16° 41' 21.5" E, Figs. 2C, 3, S3B–E) and one is from near the middle of the core 1B profile (Fig. S4).

Additional zircon separates were re-analyzed from a sample (SWART7, previously dated by Linnemann et al., 2019) of the Nomtsas Formation from Farm Swartkloofberg, ca. 15 km northwest of the summit of the MTC Tower section (Figs. 2C, S3F). This ash bed fragment is from an olistolith that overlies a matrix-supported conglomerate dominated by cobble-sized rounded to sub-rounded limestone clasts. This conglomerate corresponds to the lowermost part of the Nomtsas Formation in this area and locally overlies a major erosive unconformity (Saylor and Grotzinger, 1996; Linnemann et al., 2019).

Finally, we sampled two closely spaced and previously undated silicified ash beds from an extensive section at Aussenkjer (base of section: 28° 17′ 37.3" S, 17° 22' 51.4" E; Figs. 2D, 6A), along the Orange River to the north of the NNP. This section (first described by Kröner and Germs, 1971) dips towards the SE and reaches a total thickness of ca. 900 m. It comprises, in ascending order, Cryogenian diamictite and siliciclastic deposits of the Numees Formation of the Port Nolloth Group, which are separated from overlying deposits of the Dabis Formation by an angular unconformity (Fig. 6B). The base of the overlying Nudaus Formation at Aussenkjer unconformably overlies the Dabis Formation and hosts a prominent conglomerate, which was termed the 'basal Schwarzrand diamictite' by Kröner and Germs (1971) or Vingerbreek diamictite by Zieger-Hofmann et al. (2022). It contains rounded and subrounded boulder- and pebble-sized clasts dominated by reworked carbonate from the underlying Kuibis Subgroup in an iron-rich calcareous-siliciclastic matrix (Fig. 6C; Kröner and Germs, 1971). While the Kuibis Subgroup is condensed and truncated in this section, both the Nudaus and Urusis Formations of the Schwarzrand Subgroup are extensive and reach a total thickness of up to 700 m (Figs. S1, S2). Here, subdivision of the carbonate-dominated upper part of the Urusis Formation into the Huns, Feldschuhhorn, and Spitskop Members is unclear. No significantly thick siliciclastic units are noted that might help to distinguish the Feldschuhhorn Member or siliciclastic interbeds of the Spitskop Member (Fig. S1). Therefore, the carbonate-dominated interval of the Urusis Formation at Aussenkjer, which is dominantly limestone, either represents deposits coeval to the Huns Member only, or strata coeval to the middle–upper part of the Urusis Formation of the Swartpunt area but in a setting where siliciclastic deposition was limited. Two ash bed samples (samples FM78 and FM73, Fig. S3G-H) were collected from the middle–upper interval of Urusis Formation carbonate in this section (Figs. 2D, 6A).

3.2. Zircon U-Pb CA-ID-TIMS

U-Pb geochronology was carried out on single zircon crystals following the methods detailed in the supplementary text. Zircon crystals were separated from silicified ash deposits using standard techniques (either crushing, milling and sieving to <300 μm or SelFrag, followed by density separation using a Wilfley Table, Frantz magnetic separation, and methylene iodide heavy-liquid separation). Zircon crystals were optically examined, and prismatic grains were selected that showed no signs of detrital abrasion and did not have distinct inherited core morphologies.

Selected zircon grains were annealed and pre-treated via chemical abrasion at 180–210 °C for 10–12 h, following the methods of Mattinson (2005, full laboratory-specific methodological details are provided in the Supplementary Materials). Individual zircon grains were dissolved in HF and spiked with 4–6 mg of the EARTHTIME ^{202}Pb-^{205}Pb-^{233}U-^{235}U tracer solution (calibration version 3; Condon et al., 2015; McLean et al., 2015). Uranium and lead purification was done using anion-exchange chromatography, and Pb and U were subsequently loaded onto single outgassed Re filaments using a silica-gel emitter and measured via thermal ionization mass spectrometry (TIMS, see Supplementary Materials for further laboratory procedures and analytical details). Lead isotopes were measured on a secondary electron multiplier (SEM) in peak hopping mode, while uranium was measured on faraday cups equipped with 10^{13} Ω resistors and in rare cases of insufficient intensities measured on SEM. Measured Pb and U isotopic ratios were corrected for mass fractionation using the double spike ratios. Isobaric interferences from UO_2 isotopologues were corrected using $^{18}O/^{16}O$ ratio of 0.00205 ± 0.9 %. The measured uranium isotopic ratios were corrected assuming a sample $^{238}U/^{235}U$ ratio of 137.818 ± 0.045 (2σ; Hiess et al., 2012). All common Pb in the zircon analyses was attributed to the procedural blank, while the U blank was <0.1 pg and a value of 0.05 pg ± 50 % was used in all data reduction.

Zircon geochronology of ash beds from outcrop sections (Donkergange, MTC Tower, Swartkloofberg and Aussenkjer) was completed at the University of Geneva, and one ash sample from GRIND-ECT core 1B was processed at the National Environment Isotope Facility (NEIF) at the British Geological Survey (BGS), Keyworth. Data reduction and uncertainty propagation were carried out using the TRIPOLI and Redux software (Bowring et al., 2011). All data are reported using the community accepted distinctions between dates and ages (e.g., Condon et al., 2024). Data reporting and detailed procedural information are available in the Supplementary Materials and Table S2.

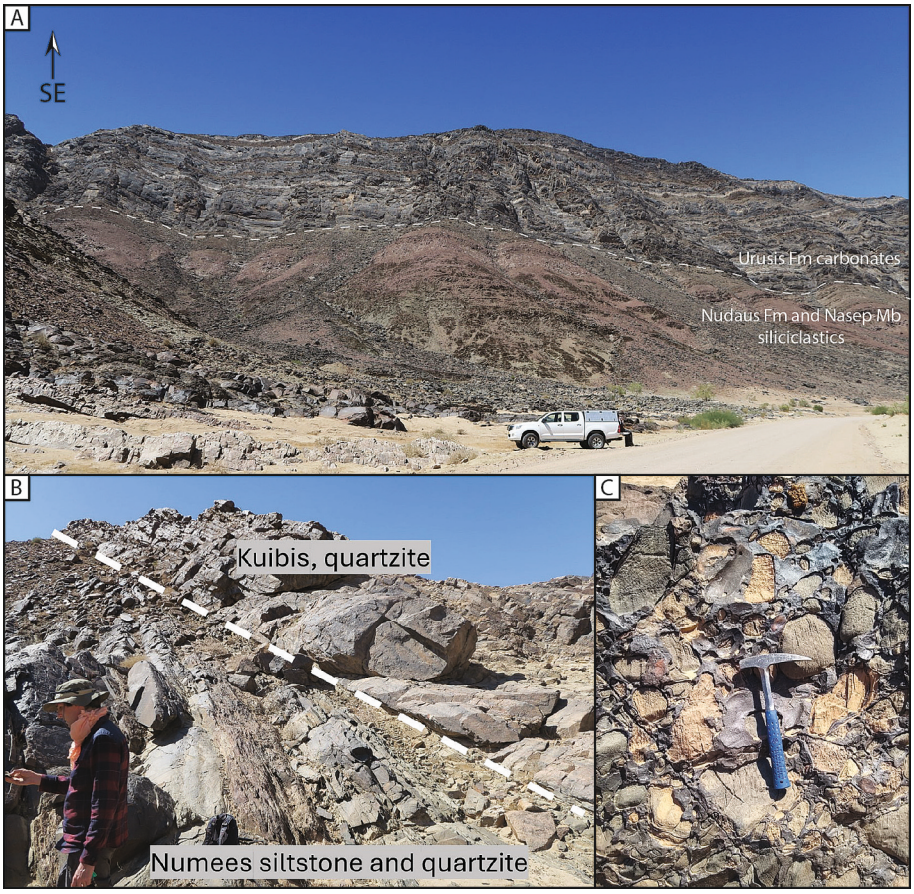

Fig. 6. Outcrop photographs of the section at Aussenkjer, along the Orange River. **(A)** Outcrop view in SE direction, showing dipping strata dominated by siliciclastics of the lower part of the Schwarzrand Subgroup (Nudaus Formation and Nasep Member of the Urusis Formation) and bedded carbonates of the upper part of the Schwarzrand Subgroup (Urusis Formation). **(B)** Angular unconformity separating the Numees Formation of the Cryogenian Port Nolloth Group from overlying coarse siliciclastics of the basal part of the Kuibis Subgroup (Dabis Formation). **(C)** Conglomerate at the base of the Nudaus Formation, which unconformably overlies the Kuibis Subgroup and contains reworked carbonate clasts in a calcareous-ferruginous matrix. Fm. – Formation; Mb. – Member.

3.3. Hafnium isotopic composition

Following U-Pb column purification, the trace element elutions of the dissolved zircon grains were analyzed for Hf isotope compositions following the methods in Gaynor et al. (2023) and detailed in the Supplementary Materials. Samples analyzed for Hf composition include those that underwent U-Pb geochronology at the University of Geneva for this study, as well as additional analyses that were performed on a selection of samples with U-Pb data previously published in Linnemann et al. (2019). Data reduction to obtain the $^{176}Hf/^{177}Hf$ ratio included on-peak zero baseline correction, correction for mass bias induced by the mass spectrometer measurement, correction of isobaric interferences of ^{176}Lu and ^{176}Yb on ^{176}Hf, and an offset correction by adjusting the $^{176}Hf/^{177}Hf$ ratio of the sample for the difference between the measured (0.272167 ± 0.000018, $n = 60$) and standardized value of the JMC475 Hf standard (i.e. 0.282160, Nowell et al., 1998). The average $^{176}Hf/^{177}Hf$ ratio of all measured Plešovice solutions used as standards during the period of sample analyses was 0.282488 ± 0.000017 ($n = 25$), which translates to an $\varepsilon Hf_{(t)}$ value of -3.0 ± 0.6 (2SD) at an age of 337 Ma, which is identical within error to the proposed value in the literature of $\varepsilon Hf_{(t)} = -3.5 \pm 1.5$ (Sláma et al., 2008). All $\varepsilon Hf_{(t)}$ uncertainties discussed in the text and shown in figures are reported at the 2σ uncertainty level. For individual analyses with uncertainties below the variation of the secondary standards, we report those uncertainties as ± 0.6 $\varepsilon Hf_{(t)}$, equivalent to the repeatability of Plešovice standard measurements during the analytical period. Uncertainties of analyses varied due to individual analyte abundances (see supplementary text for details).

3.4. Carbon and oxygen isotopes

Carbonate samples were collected through carbonate-dominated intervals of the Urusis Formation on farms Swartpunt and Nord Witputz from MTC Tower, SWP-K34 and core 1B, for $\delta^{13}C_{carb}$ chemostratigraphy. Powders were micro-drilled from fresh surfaces targeting homogeneous micritic carbonate matrix, and avoiding veins, fractures, siliciclastic components, and areas with visible signs of alteration. Sample powders from MTC Tower were analyzed for their $\delta^{13}C_{carb}$ and oxygen isotope ($\delta^{18}O_{carb}$) compositions at the Stable Isotope Laboratory of the Institute of Earth Surface Dynamics at the University of Lausanne, Switzerland, using a Gas Bench II carbonate preparation device connected to a Delta V isotope ratio mass spectrometer (Spötl and Vennemann, 2003). All isotopic ratios are reported in the delta (δ) notation as per mil (‰) relative to the Vienna Pee Dee Belemnite (VPDB) standard. Replicate analyses of NBS 19 (limestone; $\delta^{13}C = 1.95$ ‰, $\delta^{18}O = -2.19$ ‰) and an in-house standard (Carrara marble; $\delta^{13}C = 2.05$ ‰, $\delta^{18}O = -1.7$ ‰) had standard deviations (1σ) of better than ±0.05 ‰ for $\delta^{13}C$ and better than ±0.1 ‰ for $\delta^{18}O$.

Carbonate powders from SWP-K34 and core 1B were analyzed by continuous flow elemental analyzer isotope ratio mass spectrometry at either the University of Edinburgh Wolfson Laboratory, or at Iso-Analytical Ltd. Replicate analyses of samples and standards yielded

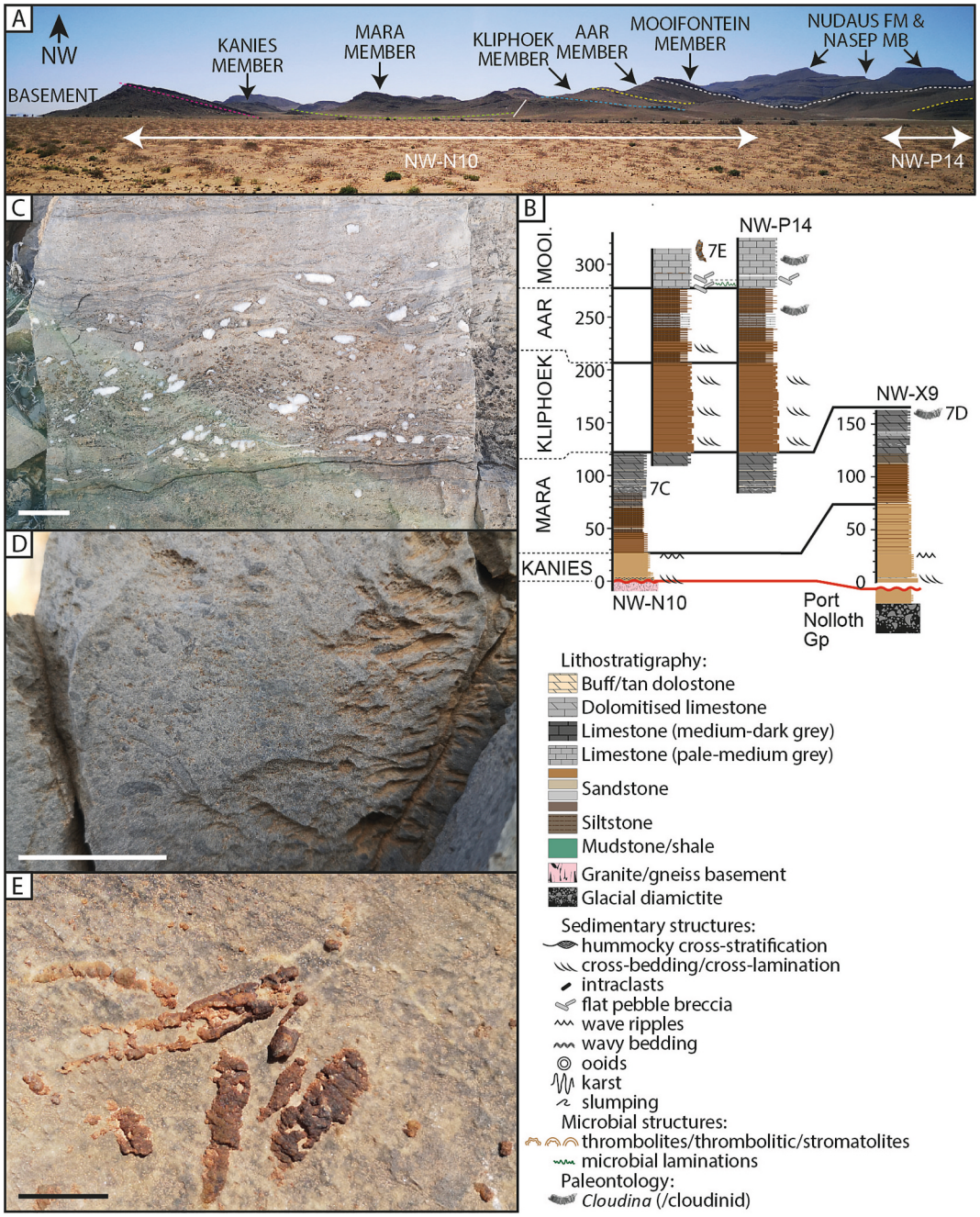

Fig. 7. **(A)** Outcrop photograph of dipping strata of the Kuibis Subgroup of the upper thrust plate on Farm Nord Witputz. **(B)** Measured sections through the Kuibis Subgroup of the upper thrust plate on Farm Nord Witputz. **(C)** Calcite-filled vugs in evaporitic dolostone of the Mara Member. Scale bar = 10 cm. **(D)** Small, reworked cloudinids in dolostone of the upper part of the Mara Member [re-discovered in section NW-X9 by F.B. after initial discovery by A. Liu and B. O'Connell (Department of Earth Sciences, University of Cambridge), oral pers. com., 2023]. Cloudinids are distinguished by their broadly cylindrical morphology and circular cross-sections, but remnant cone-in-cone structure is not visible on outcrop surfaces. Scale bar = 1 cm. **(E)** Cloudinids of the Mooifontein Member at section NW-N10, with external walls that preserve cone-in-cone structure as iron oxide. Mooi. – Mooifontein Member. Scale bar = 2 cm. Fm. – Formation; Mb. – Member.

standard deviations (1σ) of better than ±0.08 ‰ for $\delta^{13}C$ and better than ±0.12 ‰ for $\delta^{18}O$. Raw data are provided in Table S1. These new geochemical data cover the Huns Member through middle part of the Spitskop Member in the Swartpunt area (Fig. 2C).

4. Results

4.1. Lithostratigraphy and chemostratigraphy of the Swartpunt area

We build a framework for the interpretation of newly reported chemostratigraphic and geochronological data in the Swartpunt area by systematically describing the stratigraphy of measured sections across the full succession, from the base of the UTP through to the top of the LTP (Figs. 4B, 5B, expanded in Figs. S1 and S7). We also review the outcrop expression of intervening thrust displacements. This stratigraphy is described and discussed using the sequence stratigraphic descriptions of Saylor (2003) (e.g., medium-scale sequence B3, see Section 2.2), for ease of comparison to previous work.

4.1.1. Kuibis Subgroup of the Upper Thrust Plate (UTP)

The contact between siliciclastic rocks of the lower part of the Kuibis Subgroup and the underlying basement (either granite or Cryogenian

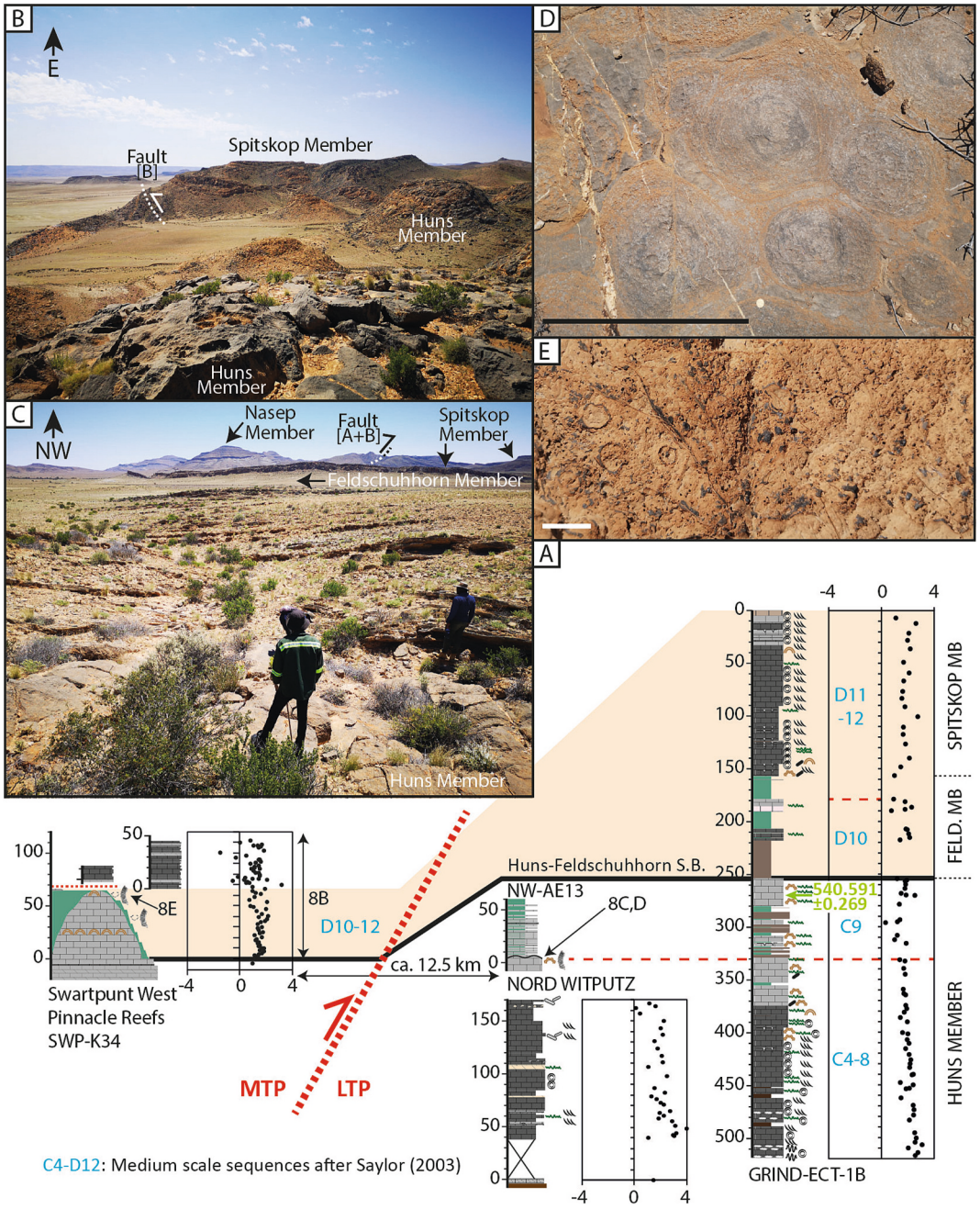

Fig. 8. **(A)** Measured sections of the Huns Member through lower part of the Spitskop Member of the Urusis Formation. Lithostratigraphy and $\delta^{13}C_{carb}$ data of the 'Nord Witputz' section after Bowyer et al. (2022). **(B)** Outcrop photograph of the middle thrust plate on the western edge of Farm Swartpunt, showing Huns Member pinnacle reefs and enveloping Feldschuhhorn Member shale deposited during medium-scale sequences D10–12 (Saylor and Grotzinger, 1996), and overlying Spitskop Member corresponding to E13–15. **(C)** Outcrop photograph showing the flooding surface of medium-scale sequence C9 in the uppermost part of the Huns Member of the lower thrust plate (section NW-AE13), with M. Shipanga standing on the stromatolitic surface in foreground. **(D)** Stromatolitic surface in C9 of the uppermost part of the Huns Member of the lower thrust plate (section NW-AE13). Scale bar = 50 cm. **(E)** Specimens of *Namacalathus* co-occur with dolomitized stromatolitic laminae in limestone at the summit of a pinnacle reef, measured section SWP-K34, middle thrust plate on the west side of Farm Swartpunt. Scale bar = 1 cm. Key to lithostratigraphic and sedimentological symbols provided in Fig. 7. S.B. – Sequence boundary; Mb. – Member.

Port Nolloth Group), is exposed in the central-west of farm Nord Witputz (Figs. 5B, 7A, B, S1). Here, Kuibis Subgroup strata have a consistent average structural dip of 25° due NNE, and locally exhibit large-scale folding and associated faulting, with the strike of fold axes and fault planes parallel to the strike of major fault planes that separate the UTP from the MTP and LTP (NW-SE or NNW-SSE, Figs. 4B, 5B). The contact between the basement and the Kanies Member is best exposed in section NW-N10 (Fig. 7B), where the Kanies Member consists of a basal ca. 4 m-thick unit of cross-bedded, matrix-supported pebble conglomerate with angular to sub-rounded quartz clasts, overlain by coarse cross-bedded sandstone and quartzite with straight-crested and bifurcating symmetrical ripples. The thickness of the Kanies Member increases eastward and reaches >70 m at section NW-X9 (Fig. 7B). A transgressive surface separates the lowstand Kanies Member from transgressive deposits of the lower part of the Mara Member and is distinguished by a prominent decrease in average grain size from sandstone to siltstone with mudstone interbeds and recessive exposure. Thin interbeds of buff-tan dolostone punctuate the siliciclastic-dominated lower part of the Mara Member,

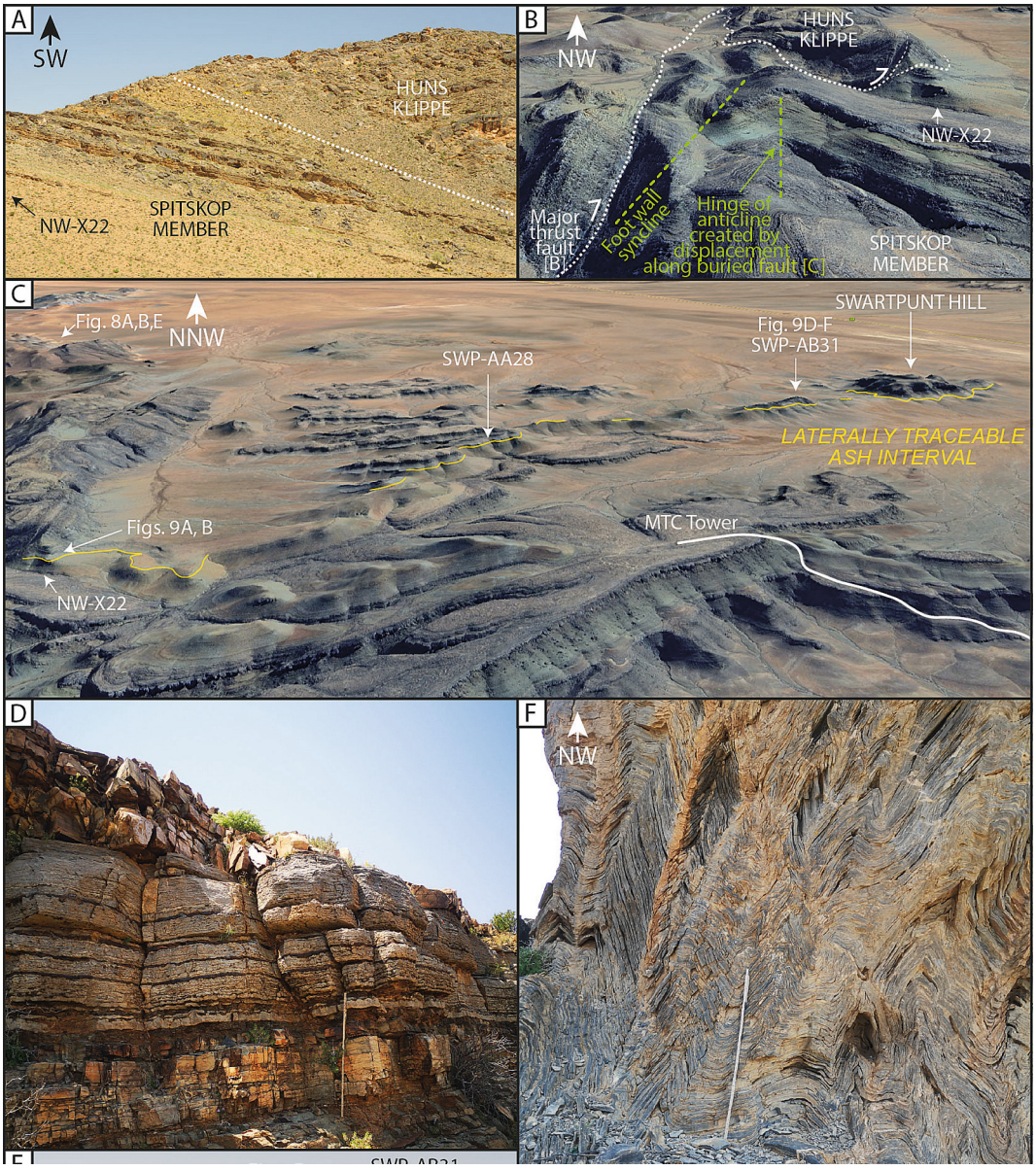

Fig. 9. **(A)** Outcrop photograph of the Huns Member klippe on Farm Nord Witputz (northern border with Farm Swartpunt). Klippe rests atop Spitskop Member limestone and corresponds to a remnant of the middle thrust plate. **(B)** Oblique satellite image showing the exposed cross-section of the thrust fault that separates the middle and lower thrust plates, with folded strata of the lower thrust plate to the east of the fault plane, overlain by the Huns Member klippe (Google Earth 2024, Maxar Technologies). **(C)** Oblique satellite image showing regional extent of correlatable ash horizon from section NW-X22 to the base of Swartpunt Hill, and dip of westernmost strata of the lower thrust plate in proximity to major thrust fault (Google Earth 2024, Maxar Technologies). **(D)** Outcrop photograph of laterally correlatable silicified ash beds, interbedded with microbial limestone. Meter rule for scale. **(E)** Outcrop photograph of section SWP-AB31, in the lower thrust plate, showing localized evidence for NE-directed compression. **(F)** Outcrop photograph of localized isoclinal folding in section SWP-AB31, with fold axes oriented NW-SE, and compressional direction due NE. Meter rule for scale.

which transitions to evaporitic dolostone of the middle part of the Mara Member that exhibits prominent vugs infilled by calcite after gypsum (Fig. 7C). Notably, while evaporitic dolostone is restricted to the middle part of the Mara Member, there is no clear transition towards limestone in the upper part of the Mara Member in measured sections on Farm Nord Witputz, which contrasts with outcrops of the Mara Member further north on the Ai-Ais map sheet (e.g., Tsaus Mountains, Fig. S1; Bowyer et al., 2023). Instead, the upper interval of the Mara Member on Farm Nord Witputz is dominantly dolomitic, with some interbeds of limey dolostone (Fig. 7B). Rare dolomitic interbeds containing small and poorly preserved, reworked cloudinids are found at the top of the uppermost part of the Mara Member (Fig. 7B, D), consistent with the broad stratigraphic position reported for the lowest occurrence of cloudinids in the Nama Group in sections to the north (Fig. S1; Kaufman et al., 2019; Bowyer et al., 2023). Overlying coarse, cross-bedded sandstones of the lowstand Kliphoek Member are up to ca. 80 m thick, and separated from interbedded siltstone, sandstone and thinly bedded limestone of the Aar Member by another transgressive surface (Fig. 7B). Cloudinids are abundant in limestone interbeds of the Aar Member, and overlying limestone of the Mooifontein Member, where some bedding planes expose *Cloudina* with cone-in-cone morphology preserved as an iron oxide coating interpreted as a weathering product after iron sulfide (e.g., pyrite, Fig. 7E).

UTP deposits of the Nudaus and Urusis Formations exposed to the north and west of sections NW-N10 and NW-P14 extend northwestward over an area of >300 km^2 towards the Tsaus Mountains of the Tsau

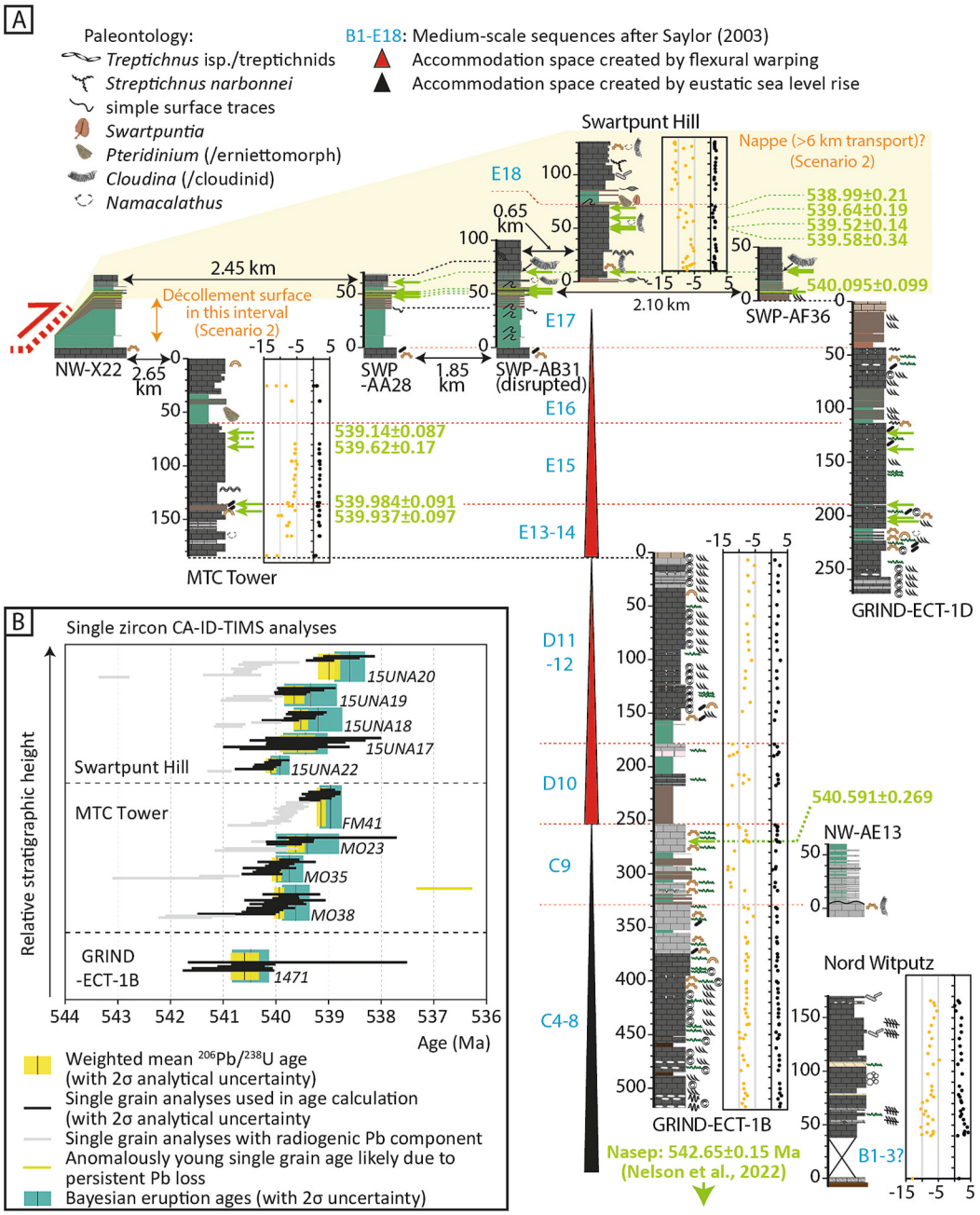

Fig. 10. **(A)** Measured sections from outcrop and drill core through the Huns, Feldschuhhorn and Spitskop Members of the lower thrust plate, showing medium-scale sequences C4–E18 after Saylor (2003). Accommodation space increase driven by eustatic sea level rise versus regional tectonic flexure follows full Witputs sub-basin stratigraphic correlation and interpretations of Saylor (2003). **(B)** Ranked zircon U-Pb plot, showing single grain analyses and age interpretations with 2σ internal/analytical uncertainty, in stratigraphic order. Note out-of-sequence ages between MTC Tower and Swartpunt Hill. Green vertical bars denote Bayesian eruption age estimates from bootstrapped distributions of all single grain ages in each sample (after Keller et al., 2018). Zircon U-Pb and $\delta^{13}C_{carb}$ data for MTC Tower (this study), zircon U-Pb data for Swartpunt Hill after Linnemann et al. (2019), and $\delta^{13}C_{carb}$ for Swartpunt Hill after Bowyer et al. (2022). Key to lithostratigraphic and sedimentological symbols provided in Fig. 7. (For interpretation of the references to colour in this figure legend, the reader is referred to the web version of this article.)

//Khaeb National Park (Fig. 4A, B, S1). The informal 'lower' Nomtsas Formation is also locally exposed on the UTP, on the western edge of Farm Swartkloofberg (Saylor and Grotzinger, 1996).

4.1.2. *Litho- and chemostratigraphy of the Huns to Spitskop Members of the Middle and lower thrust plates*

Outcrops on the western edge of Farm Swartpunt and the eastern edge of neighboring Farm Swartkloofberg include strata of the MTP (Figs. 5B, 8, S7). Here, numerous mid-ramp to slope thrombolite-stromatolite pinnacle reefs are exposed (Fig. 8A, B). These nucleated atop stromatolite sheet facies (e.g., Fig. 8D) during drowning of the upper part of the Huns Member carbonate platform (Saylor and Grotzinger, 1996; Grotzinger, 2000; Grotzinger et al., 2000; Saylor, 2003). Pinnacle reefs reach heights of >60 m and, alongside enveloping shale and siltstone of the Feldschuhhorn Member, have been correlated with medium-scale sequences D10–12 (Fig. 5A), which record rapid accommodation space increase driven by flexural warping (Saylor, 2003). On the LTP, an earlier pulse of platform drowning corresponds with the transition from stromatolitic limestone of C8 to interbedded limestone and shale of C9 (e.g., sections NW-AE13 and core 1B, Fig. 8A, C), and

final flooding is represented by overlying Feldschuhhorn Member siliciclastic rocks of D10 (core 1B, Fig. 8A).

Skeletal *Cloudina* and *Namacalathus* are common components of thrombolite-stromatolite surfaces of the MTP and LTP and are especially abundant near the summit of the Huns Member pinnacle reefs of SWP-K34 (e.g., Fig. 8A, E). Thin- to medium-bedded dark gray limestones and buff-tan dolomitized limestones of the Spitskop Member overlie Huns Member pinnacle reefs of the MTP, and correlate with medium-scale sequences E13–14 (possibly extending into E15) of the LTP (Figs. 4A, B, 8A; Saylor, 2003).

Samples from core 1B yielded $\delta^{13}C_{carb}$ from 0.32 ‰ to 3.09 ‰ (mean = 1.88 ‰), and $\delta^{18}O_{carb}$ from −15.13 ‰ to −5.23 ‰ (mean = −8.55 ‰). The lowest $\delta^{18}O_{carb}$ values are in limestones that are proximal to siliciclastic rocks in C9, D10 and lower D11 (Fig. S1, Table S1). There is an overall decreasing trend in $\delta^{13}C_{carb}$ throughout C4–C8 in core 1B, with initial values of ca. 2.50 ‰ that decrease to reach a nadir of 0.32 ‰ in the middle of C9 (Fig. 8A). Thereafter, $\delta^{13}C_{carb}$ values range between 0.76 ‰ to 2.76 ‰, with the lowest values in proximity to siliciclastic intervals and the core collar.

Samples from SWP-K34 yielded $\delta^{13}C_{carb}$ in the range − 1.45 ‰ to 3.19 ‰ (mean = 1.28 ‰), and $\delta^{18}O_{carb}$ from −11.84 ‰ to −5.82 ‰ (mean = −7.90 ‰). The lowest sample in SWP-K34, which corresponds with the stromatolite sheet facies of C9, yielded a $\delta^{13}C_{carb}$ composition of 0.96 ‰, whereafter values increase and stabilize between 0.72 ‰ to 2.17 ‰ (mean = 1.50 ‰) throughout the overlying pinnacle reef (Fig. 8A). Carbonates of the lower-middle part of the Spitskop Member in SWP-K34 yielded scattered values between −1.45 ‰ and 3.19 ‰ (mean = 1.05 ‰), with the lowest $\delta^{13}C_{carb}$ values in dolomitized limestone interbeds.

While no significant $\delta^{13}C_{carb}$ excursions are present to aid correlation, the magnitude and trend of $\delta^{13}C_{carb}$ data through the pinnacle reefs of SWP-K34 broadly align with the magnitude and trend of data through D10–12 in core 1B. Available chemostratigraphic and lithostratigraphic data from SWP-K34 and core 1B correspond well when using the sequence stratigraphic correlation of Saylor (2003) for medium-scale sequences between the MTP and LTP (Fig. 8A).

Carbonates of the Spitskop Member are folded and locally faulted in proximity to the major thrust fault that separates UTP from MTP deposits on the western edge of section SWP-K34, with parallel strike of fold axes and fault planes. As noted by Saylor and Grotzinger (1996), the MTP is only locally exposed further to the southeast, where Huns Member limestones outcrop as a klippe atop Spitskop Member deposits of the LTP (Fig. 9A, B, S6A). Saylor and Grotzinger (1996) also noted folding of the LTP in proximity to the major bounding thrust fault, which is evident where LTP limestones of the Spitskop Member are locally folded into a footwall syncline immediately to the west of an anticline that uplifts the western edge of the Huns klippe (Fig. 9B).

4.1.3. Stratigraphy and compression of the Urusis Formation of the lower Thrust Plate (LTP)

We present outcrop and core stratigraphy for the LTP that covers the entirety of the middle-upper part of the Huns Member, through Feldschuhhorn and Spitskop Members, corresponding to medium-scale sequences C4–E18 (Figs. 8–10). Strata of the LTP distant from major bounding faults exhibit a regional average dip towards the north/northwest. Consequently, the MTC Tower section and core 1D (Fig. 5B) both capture the same stratigraphic levels, which predominantly cover medium-scale sequences E13–E16 (Fig. 10A).

The MTC Tower section was measured in reverse stratigraphic order, beginning at a readily accessible and correlative level of laterally continuous stromatolitic limestone (upper surface of E16, Saylor, 2003). The base of the MTC Tower section begins tens of meters stratigraphically above the Feldschuhhorn/Spitskop boundary, which is best exposed ca. 3.8 km to the south/southwest of the base of section (Fig. 5B). The MTC Tower section begins with dark-gray to black thinly laminated limestone, with two prominent intervals of more thickly bedded limestone. Abundant *Namacalathus* were observed on bedding planes in an interval of massively bedded limestone near the base of the section (ca. 165 m below the section summit, Fig. 10A). Thinly bedded intervals in the lower part of the section commonly contain white limestone interbeds. At ca. 145 m below the top of the section, a dark limestone unit with abundant elongate stromatolites underlies the lowest identified ash bed (ca. 20 cm-thick sample MO38 at ca. 142 m below the section summit, Fig. S3B), which is separated from the second ash bed (ca. 80 cm-thick sample MO35 at ca. 136 m below section top, Fig. S3C) by a prominent sandstone bed between two layers of brecciated platy clasts (Fig. 10A). Both ash beds are laterally continuous for >3 km around the outcrop towards the NNE (Fig. 5B). The following ca. 75 m consists of a shallowing-up succession that begins with thinly bedded limestones with occasional wave ripples and wavy bedding, which grade into more thickly bedded limestones. Three ash beds are exposed near the top of the thickly bedded interval, of which two samples were analyzed in this study (ca. 10–15 cm-thick sample MO23 at ca. 83 m below the section summit, and ca. 50 cm-thick sample FM41 at ca. 70 m below the section summit, Fig. S3D–E). These ash beds are separated by black, thickly bedded, resistant stromatolitic limestone and an intervening ca. 20 cm-thick ash bed. The upper surface of the thick bedded limestone is overlain by a ca. 27 m-thick interval of olive-green shale and siltstone with intercalations of gray mudstone and siltstone. The boundary between the limestone and siltstone (ca. 61 m below the section summit) marks the transgressive surface of medium-scale sequence E16 (Saylor, 2003). Partial candidate erniettomorph specimens (Figs. S5A, S5B) and possible indeterminate ichnofossils (Fig. S5C) are present on the surfaces of several more resistant, pale-brown siltstone beds and in float material throughout this interval. The siliciclastic-dominated unit is overlain by black limestone, which starts with a thick bedded unit and transitions through a thinly bedded interval, before showing a gradual increase in bed thickness upwards to the top of the section (Fig. 10A). As noted above, the top of the section is a laterally extensive and generally planar limestone bed that marks the top of E16, with an upper surface exhibiting cross-sections of stromatolites that occasionally exceed 50 cm in diameter, with thrombolitic cores (Fig. S5D).

Four silicified ash beds were collected from the MTC Tower section. In stratigraphic order, these are samples MO38, MO35, MO23 and FM41 (Figs. 10A, 11, S3B–E). The top of the MTC Tower section (upper surface of E16) is traceable laterally along the section summit, but is buried beneath siliciclastics of overlying medium-scale sequence E17 towards the north and northwest (Fig. 5B). The top of E16 lies ca. 50 m beneath the ash bed at the base of Swartpunt Hill, which yielded an age of 540.095 Ma in Linnemann et al. (2019), with stratigraphic superposition throughout the succession confirmed by outcrop and drill core correlation, noting average stratal dip towards the NNW in this area (Fig. 5B).

Carbon isotope values show limited variability throughout the MTC Tower section (Fig. 10A). At the base of the section, $\delta^{13}C_{carb}$ values range from +0.3 ‰ to +0.8 ‰, with $\delta^{18}O_{carb}$ values as low as −14.2 ‰ (Fig. 10A, Table S1). Both $\delta^{13}C_{carb}$ and $\delta^{18}O_{carb}$ compositions increase thereafter to a mean value of +1.9 ‰ ±0.19 ‰ and − 6.6 ‰ ±1.41 ‰, respectively, up to the base of the olive-green siliciclastic horizon of lower E16. In the upper limestone interval of E16, $\delta^{13}C_{carb}$ and $\delta^{18}O_{carb}$ reach +2.1 ‰ and − 5.3 ‰, respectively, before decreasing to variable values as low as +0.1 ‰ ($\delta^{13}C_{carb}$) and − 14.2 ‰ ($\delta^{18}O_{carb}$).

In the vicinity of the Huns klippe, the lower siliciclastic part of E17 is exposed in section NW-X22 (Figs. 9B, C, 10A, S6A). The base of this section is at the base of the E17 transgressive surface that directly overlies the upper stromatolitic limestone of E16, thereby overlying the MTC Tower section and correlating with siliciclastics in the uppermost ca. 40 m of core 1D (Fig. 10A). NW-X22 consists of a lower unit of green siltstone and mudstone, an overlying unit of interbedded siltstone and fine sandstone, and finally a limestone-dominated upper unit (Fig. 10A). Silicified and resistant, buff-tan weathering ash layers are interbedded with fine sandstones and limestones near the base of the limestone-

dominated unit (Figs. 9C, 10A, S6A). Lateral correlation of measured sections confirms that this ash interval is traceable for >6 km from southwest to northeast, but is only locally exposed fully at the base of the southern and eastern edges of Swartpunt Hill (Figs. 9C, D, 10A).

The limestone-dominated upper half of E17, which correlates to the lower part of the Swartpunt Hill type section, locally shows signs of compressional deformation. This is especially evident in section SWP-AB31 and the western edge of Swartpunt Hill, where thinly bedded limestones of upper E17 are isoclinally folded, with fold axes aligned NW-SE, parallel to the strike of major faults (Figs. 9E, F, 10A). Northeast-vergent compression is also evident from the broader structure of SWP-AB31, where the southwest side is at notably higher elevation than the northeast (Fig. 9E).

4.2. Geochronology

Table 1 and Fig. 11A summarize all new U and Pb isotopic data, with average analytical uncertainty of individual zircon $^{206}Pb/^{238}U$ dates carried out at the University of Geneva of ±360 kyr (0.07 %). Accordingly, the internal uncertainties of the calculated $^{206}Pb/^{238}U$ weighted mean ages are all <200 kyr (<0.04 %). Ages for each volcanic ash bed were calculated based on the weighted mean of the statistically equivalent youngest cluster of $^{206}Pb/^{238}U$ dates within the limits of acceptable MSWD at the 95 % confidence level and for n-1 degrees of freedom defined by Wendt and Carl (1991, see selected zircon grain CL images in Fig. S8 and concordia diagrams in Figs. S9 and S10). Dates resolvably older than the youngest cluster for each sample were excluded from

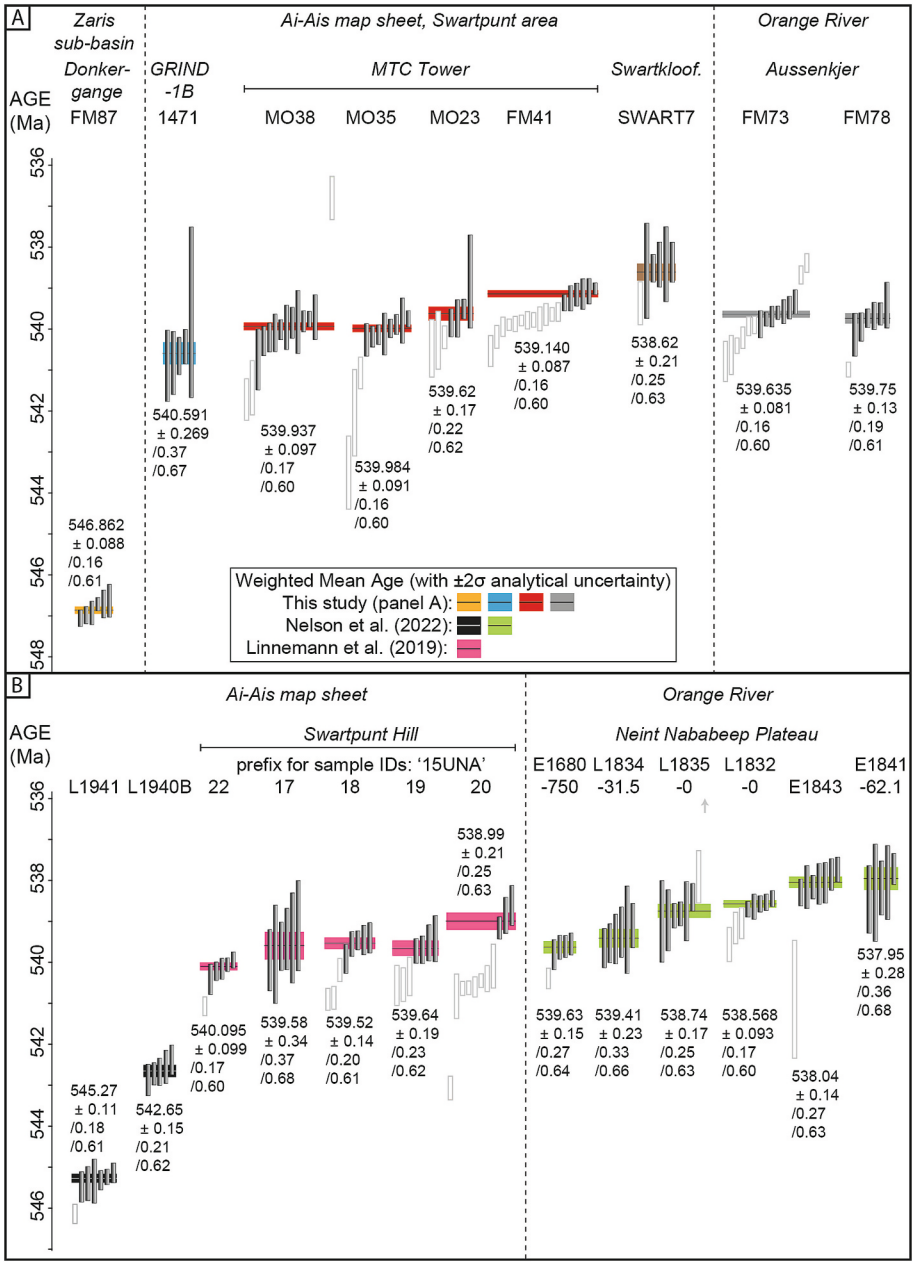

Fig. 11. Ranked age plots of analyzed zircon grains from sampled ash beds. Vertical bars show individual single grain zircon analyses with 2σ internal/analytical uncertainty. Filled gray bars show analyses used for weighted mean age determinations. Colored horizontal bands represent 95 % confidence level (2σ) analytical uncertainties of weighted mean dates. (A) Data presented herein from sampled ash beds of Donkergange, GRIND-ECT core 1B, MTC Tower and Aussenkjer successions. (B) Data presented in Linnemann et al. (2019) for samples from Swartpunt Hill, and in Nelson et al. (2022) from samples of the Ai-Ais map sheet area and the Neint Nababeep Plateau. In both panels, samples from distinct areas (i.e., Zaris sub-basin, Ai-Ais map sheet, Orange River sections) are ordered in stratigraphic superposition from left (lowest) to right (highest), demonstrating younging-upwards ages within analytical uncertainty for ash beds sampled and analyzed.

weighted mean age calculations, based on the interpretation that they represent xenocrystic or antecrystic zircon, or were incorporated during the volcanic eruption and deposition through surficial processes. Significantly younger zircon dates from samples MO38 and FM73 were also excluded from age interpretations, based on the interpretation that they may still reflect loss of radiogenic lead, despite chemical abrasion. As an additional approach to estimate eruption ages for the dated ash beds, $^{206}Pb/^{238}U$ dates were used to estimate a Bayesian eruption age (BEA) model using the algorithm of Keller et al. (2018). A bootstrapped prior distribution was used for all samples, and dates interpreted to have been affected by residual Pb-loss were omitted from BEA calculations. Normally discordant dates were also excluded from these calculations because they can artificially bias eruption estimates to inaccurate ages (e.g., Gaynor et al., 2023). This approach has the advantage of accounting for potential time between final zircon crystallization and the timing of eruption and therefore may be a way to account for potential geologic uncertainty in determining the age of stratigraphy. In all cases, the two age interpretations agree within uncertainty for each sample, however the BEA interpretations yield larger uncertainties (Fig. S11). Therefore, although we interpret weighted mean ages to approximate the age of deposition in the results section, prior to considering regional correlation throughout the following discussion, the larger uncertainties mean that modeled BEAs can be considered as conservative depositional age estimates, in each case.

The oldest ash bed from the Zaris sub-basin (sample FM87, Figs. 2B, 3, 11) was dated via six zircon analyses, all analytically concordant and yielding a weighted mean $^{206}Pb/^{238}U$ age of 546.862 ± 0.088 (0.16) [0.61] Ma (MSWD = 2.5, $n = 6$) and a BEA of 546.68 ± 0.23 Ma (n = 6, 2σ). This age is interpreted as a best estimate for the depositional age of the ash bed and, therefore, the age of the lower part of the Hoogland Member.

A total of six ash beds were analyzed from the Swartpunt area, including sample 1471 from GRIND-ECT drill core 1B (Figs. 10–11). The stratigraphic position of this ash interbed from core depth 269.9 m agrees with the known position of an ash bed in outcrop of medium-scale sequence C9 (Saylor, 2003). This ash bed is thin (≤2 cm-thick, Fig. S4A) but has a similar composition to the coarse bases of overlying ash beds (e.g., Fig. S4D), and selected zircon grains were small, prismatic and showed no sign of detrital abrasion or distinct inherited core morphologies. While the high temperature (210 °C) of chemical abrasion effectively eliminates zircon domains that have been subject to residual Pb loss, this occasionally results in very low concentrations of radiogenic Pb and therefore lower precision (Figs. 10B, 11; e.g., Gaynor et al., 2022). Nevertheless, all $^{206}Pb/^{238}U$ dates from single zircon analyses of sample 1471, analyzed at the NEIF, BGS, Keyworth, yielded a weighted mean age of 540.591 ± 0.269 (0.37) [0.67] Ma (MSWD = 0.63, $n = 5$ of 5, Figs. 10B, 11, S10) and a BEA of 540.48 ± 0.35 Ma (n = 5, 2σ). This age is resolvably older than those of overlying ash beds in MTC Tower section, and also resolvably older than the age reported from the ash bed at the base of the Swartpunt Hill type section (Linnemann et al., 2019).

Ash beds from MTC Tower and Swartkloofberg sections of the Swartpunt area (samples MO38, MO35, MO23, FM41, and SWART7, Fig. 11) are stratigraphically upsection of the drill core sample and yielded a sequence of ages through the MTC Tower section consistent with superposition. The lowermost sample, MO38, yielded a weighted mean $^{206}Pb/^{238}U$ age of 539.937 ± 0.097 (0.17) [0.60] Ma (MSWD = 1.9, $n = 11$), from eleven concordant zircon analyses, excluding one normally discordant youngest and two older crystals. This sample yielded a BEA of 539.62 ± 0.26 Ma ($n = 13$, 2σ). The next sample, MO35, yielded a weighted mean $^{206}Pb/^{238}U$ age of 539.984 ± 0.091 (0.16) [0.60] Ma (MSWD = 2.1, $n = 8$), from eight concordant zircon analyses, which excluded three older and normally discordant grains. MO35 yielded a BEA of 539.74 ± 0.26 Ma (n = 8, 2σ). Next, sample MO23 yielded a weighted mean $^{206}Pb/^{238}U$ age of 539.62 ± 0.17 (0.22) [0.62] Ma (MSWD = 1.7, $n = 4$) from four youngest concordant analyses, which excluded three older and normally discordant grains. MO23 yielded a BEA of 539.4 ± 0.60 Ma (n = 4, 2σ). In the final sample from the MTC Tower section, FM41, the six youngest dates yielded a weighted mean $^{206}Pb/^{238}U$ age of 539.140 ± 0.087 (0.16) [0.60] Ma (MSWD = 2.0, n = 6), based on six concordant analyses and excluding twelve older, concordant analyses. Sample FM41 yielded scattered zircon dates, pointing to the presence of antecrystic zircon grains, and yielded a BEA of 538.96 ± 0.21 Ma ($n = 18$, 2σ). Finally, all six analyzed zircon grains from SWART7 of Swartkloofberg section yielded concordant analyses, and the youngest five of these yielded a weighted mean $^{206}Pb/^{238}U$ age of 538.62 ± 0.21 (0.25) [0.63] Ma (MSWD = 2.2, n = 5), and the full age spectra yielded a BEA of 538.34 ± 0.37 Ma ($n = 6$, 2σ).

The two ash beds from the Aussenkjer section (samples FM73 and FM78, Fig. 2D, 11, S3G-H) yielded zircon weighted mean $^{206}Pb/^{238}U$ ages of 539.635 ± 0.081 (0.16) [0.60] Ma (MSWD = 1.9, $n = 7$) and 539.75 ± 0.13 (0.19) [0.61] Ma (MSWD = 1.3, n = 6), respectively. Six older zircon grains from FM73 and one from FM78 were excluded from these weighted mean calculations. The youngest two zircon dates of the stratigraphically higher sample, FM73, are interpreted as having unmitigated residual post-crystallization Pb-loss and are thus excluded from the weighted mean and BEA calculations. Sample FM73 yielded a BEA of 539.37 ± 0.21 Ma (n = 13, 2σ), while FM87 yielded a BEA of 539.47 ± 0.26 Ma (n = 7, 2σ).

4.3. Hafnium isotopes

There is moderate variability between the Hf isotope compositions of zircon from different samples, as well as between grains of the same sample (Fig. 12; Table S3). Four single grain analyses from sample FM87 in the Hoogland Member of the Zaris sub-basin overlap at approximately εHf = 0.9. Zircon from the lowermost ash bed of the Swartpunt Hill type section of the Spitskop Member in the Witputs sub-basin (sample 15UNA22, Figs. 10A, 11B, 12, previously dated by Linnemann et al., 2019) largely overlap within uncertainty with a composition of εHf = −2.0, with outliers at 0.3 and − 0.7. Fourteen single zircon grain analyses of the stratigraphically highest sample in the MTC Tower section (sample FM41) of the Witputs sub-basin yielded an average composition of εHf = −2.4, with one outlier at −0.8. Sample FM78 from the Aussenkjer section yielded an average composition of εHf = −2.8, with significant scatter among five single grain analyses. The stratigraphically overlying ash bed at Aussenkjer (sample FM73) yielded an average composition of εHf = −2.3, with a single outlier at 0.3. Finally, the olistostrome-hosted tuff bed from the Swartkloofberg section of the Witputs sub-basin (sample SWART7) yielded an average composition of εHf = −2.8, with one outlier at −5.2.

5. Discussion

5.1. Implications and complications of new and published ages from the Urusis Formation

5.1.1. Stratigraphic correlation between the Swartpunt area and sections along the Orange River

We present an updated litho- and chemostratigraphic correlation framework for sections of the Ai-Ai map sheet area of the Witputs sub-basin, based on a combination of measured outcrop and GRIND-ECT drill core profiles, with relative stratigraphic superposition confirmed by geological mapping (Figs. S1, S2). This compilation presents all new and/or revised radioisotopic ages alongside published ages and aids discussion of chemostratigraphic and lithostratigraphic correlation between the Swartpunt area and sections along the Orange River.

Along the Orange River, the lower, carbonate-dominated part of the Urusis Formation (Huns Member after Nelson et al., 2022) contains three ash beds that yielded ages ca. 539.6–539.7 Ma (Figs. 11, 13, Nelson et al., 2022 and this study). However, our oldest age from the Urusis Formation of the Witputs sub-basin is 540.591 ± 0.269 Ma (BEA = 540.48 ± 0.35 Ma), which is from an ash bed in the upper part of the

Table 1
Summary of calculated U-Pb dates and associated uncertainties.

Core/Section ID	Sample ID	Latitude	Longitude	Unit	$^{206}Pb/^{238}U$ Age (Ma)	Error (2σ)[a]			MSWD[b]	n[c]	No.
		(S)	(E)			*X*	*Y*	*Z*			
Swartkloofberg	SWART7	27°26′38.5”	16°33′31.6”	Nomtsas	538.62	0.21	0.25	0.63	2.2	5	6
MTC Tower	FM41	27°31′03.9”	16°41′32.7”	Spitskop	539.140	0.087	0.16	0.60	2.0	6	18
MTC Tower	MO23	27°31′6.40”	16°41′40.00”	Spitskop	539.62	0.17	0.22	0.62	1.7	4	7
MTC Tower	MO35	27°31′7.40”	16°41′58.70”	Spitskop	539.984	0.091	0.16	0.60	2.1	8	10
MTC Tower	MO38	27°31′15.00”	16°42′4.70”	Spitskop	539.937	0.097	0.17	0.60	1.9	11	14
Aussenkjer	FM78	28°19′7.20”	17°22′34.10”	Urusis	539.75	0.13	0.19	0.61	1.3	6	7
Aussenkjer	FM73	28°18′38.70”	17°22′59.10”	Urusis	539.635	0.081	0.16	0.60	1.9	7	15
GRIND-ECT core 1B	1471	27°29′31.20”	16°44′38.40”	Huns	540.591	0.269	0.37	0.67	0.63	5	5
Donkergange	FM87	24°30′26.7”	16°12′5.0”	Hoogland	546.862	0.088	0.16	0.61	2.5	6	6

[a] *X* represents the internal (analytical) uncertainty in the absence of all external or systematic errors; *Y* incorporates the U-Pb tracer calibration error; *Z* includes *X* and *Y*, as well as error in the uranium decay constant.
[b] MSWD: mean square of weighted deviates.
[c] n: number of analyses included in the calculated weighted mean age out of the total number of analyses (No.).

Huns Member (medium-scale sequence C9, Huns-Feldschuhhorn transition) in core 1B (sample 1471), which lies >400 m above the base of the Huns Member in the Swartpunt area (Figs. 10, 11, S1, S2). The two ash bed ages from the base of MTC Tower are stratigraphically above this core sample and yielded analytically identical ages of 539.937 ± 0.097 Ma and 539.984 ± 0.097 Ma (BEA = 539.62 ± 0.26 Ma and 539.74 ± 0.26 Ma, respectively), younger than the age from sample 1471, and are also either older than or unresolvable from the stratigraphically lowest dated ash beds of the Orange River sections (Figs. 10, 11).

The entire Urusis Formation may have been deposited more rapidly in the Swartpunt area than the Orange River succession while still adhering to the law of superposition, indicating that all reported weighted mean ages from the Huns-Spitskop Members in the Swartpunt area (with the possible exception of sample FM41) are too old relative to those from sections of the Orange River, and that these ash bed ages do not represent the timing of deposition relative to their stratigraphic position (Fig. 13). Alternatively, the greater stratigraphic thickness of the Huns-Spitskop Members in the Swartpunt area relative to sections along the Orange River, and the multiple older ages recorded from the Swartpunt area, may suggest that deposition of the Huns Member largely occurred >540 Ma in the north (present co-ordinates) and that the carbonate-dominated Urusis Formation along the Orange River was predominantly deposited coeval with the Spitskop Member in the Swartpunt area (Fig. 14).

A recent cyclostratigraphic study of GRIND-ECT core 1A, immediately to the northeast of the Swartpunt area, extrapolated the age of 539.63 ± 0.15 Ma from the NNP as a temporal anchor for the lower part of the Huns Member in core 1A (e.g., Fig. 13, Gong et al., 2025). If the newly reported weighted mean age from the upper unit of the Huns Member in core 1B is assumed to approximate the age of deposition, then Bayesian age-depth modelling (Bchron R package, Haslett and Parnell, 2008; Parnell et al., 2008) suggests a significantly older age of 542 ± 0.6 Ma for the base of the Huns Member in the Swartpunt area (Fig. 14). This results in two notably different estimates for the age of the lowermost part of the Huns Member and the important ichnofossil and skeletal fossil assemblage of the Nasep-Huns transition in the Swartpunt area (Turk et al., 2022; Gong et al., 2025). Using radioisotopic data from a composite succession in one geographically restricted area, rather than extrapolation of ages between distant areas, would help to reduce uncertainty associated with the possibility for lateral diachroneity of units across greater distances (e.g., between Swartpunt and Orange River areas). However, this approach is only valid if the interpreted ages, including those from the Nudaus and Urusis Formation ash beds in the Ai-Ais map sheet area, approximate depositional ages.

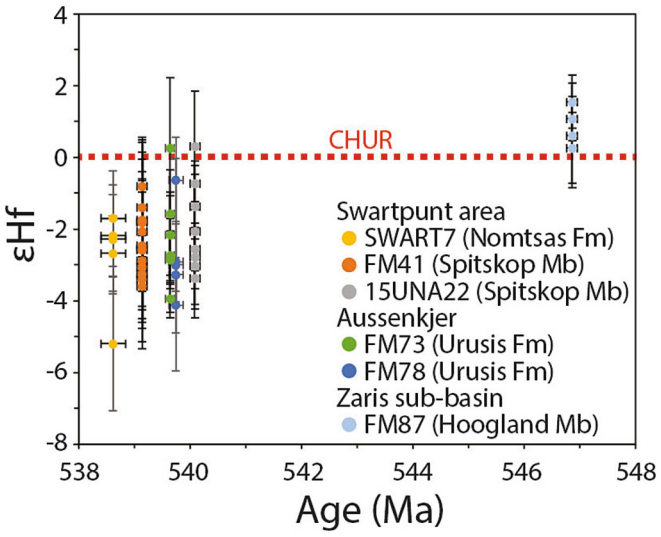

Fig. 12. Zircon εHf data relative to weighted mean dates derived from U-Pb CA-ID-TIMS analyses of the same samples. CHUR = bulk-silicate Earth chondritic uniform reservoir composition. Note decreasing εHf values with decreasing time. Fm. – Formation; Mb. – Member.

5.1.2. Systematic younging-upwards repetition of zircon U-Pb ages in the Swartpunt area

Compilation of published and new zircon U-Pb CA-ID-TIMS ages from ash beds in the Swartpunt area yields a sequence in agreement with the principle of superposition within individual sections, however comparison of these ages between sections suggests potential repetition of stratigraphy or inaccurate correlations (Fig. 10B). In ascending order, medium-scale sequence C9 contains an ash bed with a weighted mean age of 540.591 ± 0.269 Ma, E13–E14 contain ash beds with weighted mean ages of 539.937 ± 0.097 Ma and 539.984 ± 0.091 Ma (these may occur within one medium-scale sequence following merger of E13 and E14 after Spiering et al., 2023), and E15 contains ash beds with ages of 539.62 ± 0.17 Ma and 539.14 ± 0.087 Ma. Ash beds from Swartpunt Hill in overlying medium-scale sequence E17 yielded zircon U-Pb ages of 540.095 ± 0.099 Ma, 539.58 ± 0.34 Ma, 539.52 ± 0.14 Ma, 539.64 ± 0.19 Ma, and 538.99 ± 0.21 Ma (Linnemann et al., 2019). Together, this yields a sedimentary sequence from ca. 540 Ma to ca. 539.1 Ma between E13–E15, with ages that are repeated stratigraphically higher in E17. When instead interpreting this chronostratigraphic framework using BEAs to represent the depositional ages of these ash beds, this is still the case, albeit at coarser resolution, whereby uncertainty on the oldest age in C9 does not overlap with uncertainties on ages in E13–15, and the uncertainties of BEAs in uppermost E15 and lowermost E17 also do not

overlap. Therefore, the repetition of ages observed between E13–15 and E17 violates the principle of stratigraphic superposition, regardless of the age interpretation methods used here (Fig. 10B).

One of two hypotheses might explain the observed out-of-sequence ages of these tuff beds:

***Scenario 1*:** The dates of individual zircon crystals from many ash beds in the Urusis Formation of the Witputs sub-basin do not approximate their eruptive age, due to a host of potential factors such as (1) analysis of either antecrystic or subtly xenocrystic zircon, (2) incomplete sampling of complicated age spectra, or (3) unresolved Pb-loss. As a result, the interpreted ages of some or all of these horizons do not approximate their depositional timing.

***Scenario 2*:** A previously unrecognized cryptic thrust displacement between the top of E15 and below the stratigraphically lowermost ash bed of E17 has resulted in stratigraphic repetition.

Scenario 1 is consistent with the interpretation of Nelson et al. (2022) and would imply that zircon U-Pb ages from E17 (and possibly the majority from E13–15, see below) in the Swartpunt area only represent maximum depositional ages (e.g., Figs. 13, 14). Scenario 2 may resolve lithostratigraphic and age repetition but requires additional field evidence and adjustments to the tectonostratigraphic model for the uppermost part of the Spitskop Member in this area. Below, we investigate both scenarios, and their wider implications for Nama Group stratigraphic architecture and basin evolution.

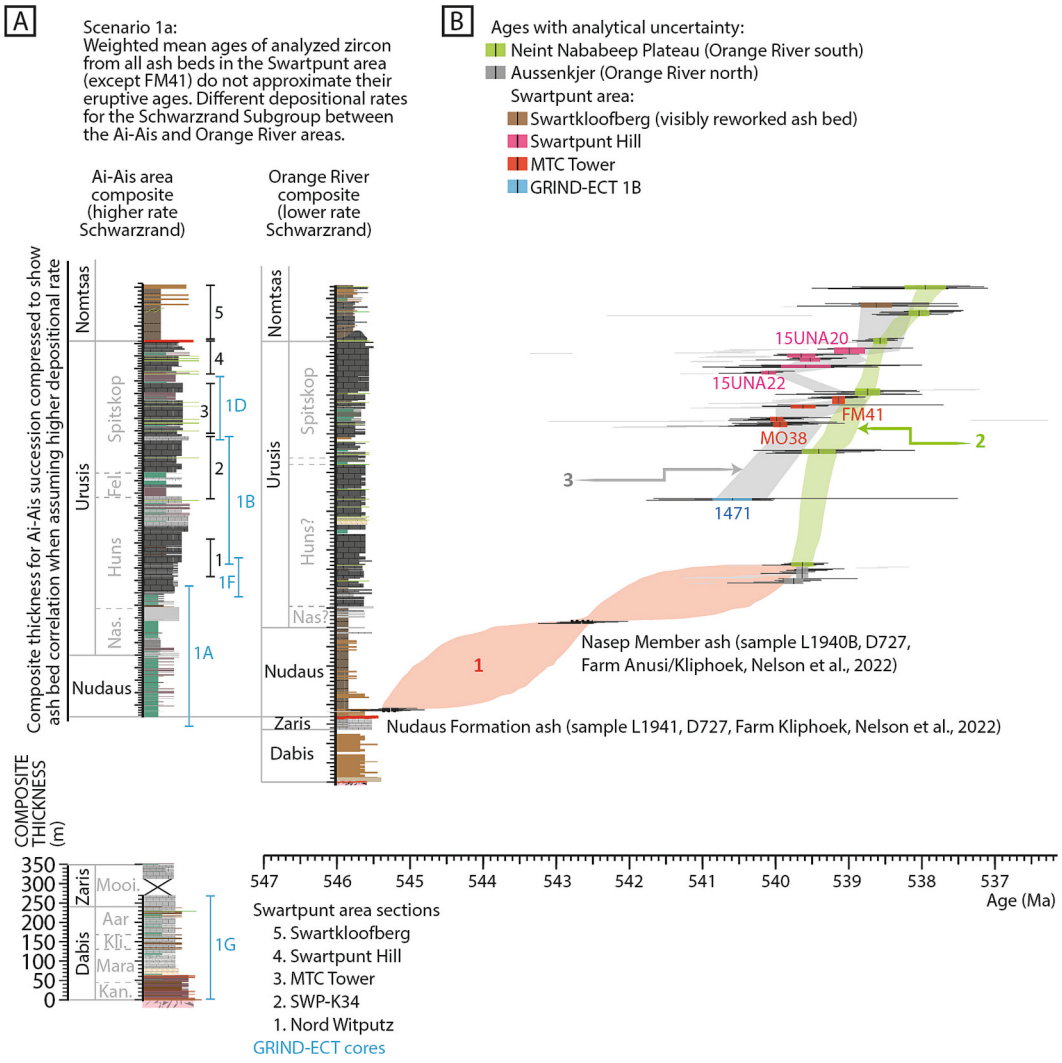

Fig. 13. Reconstructed correlation framework for the Urusis Formation following Scenario 1a. **(A)** Composite lithostratigraphic columns for the Ai-Ais map sheet area and the Orange River succession (expanded in Fig. S2). Framework extends from the depocenter to the seaward margin of the Witputs sub-basin, and southward to sections (Aussenkjer and the NNP) of the Orange River. Levels of Nudaus and Nasep ash beds in core 1A based on lithostratigraphic correlation to levels of dated ash beds in outcrop after Gong et al. (2025). **(B)** Weighted mean ages from ash beds presented in Linnemann et al. (2019), Nelson et al. (2022) and this study. Black horizontal lines are single grain analyses used in calculation of weighted mean ages; gray horizontal lines are single grain analyses not considered in weighted mean age calculations for the reasons stated in the text. Sample IDs are shown for key ash beds (refer to Fig. 11 for expanded ranked age plots). Shaded envelopes (for Bayesian age-depth models, these represent the 95 % confidence intervals): 1. Orange envelope shows the Bchron Bayesian age-depth model calibrated using a combination of extrapolated weighted mean ages and positions of associated ash beds in the Nudaus Formation and Nasep Member in the Ai-Ais map sheet area and the age of the lowermost dated ash bed of the NNP succession after Nelson et al. (2022); 2. Green envelope shows the Bchron Bayesian age-depth model for the NNP after Nelson et al. (2022); 3. Gray envelope represents Bayesian eruption age (BEA) estimates for all newly reported weighted mean ages from the Swartpunt area, using bootstrapped distributions of single grains after Keller et al. (2018). This correlation implies that all weighted mean ages reported from the Spitskop Member in the Swartpunt area represent maximum depositional ages only (with the exception of sample FM41), and that autocrystic zircon grain populations in these ash beds have been largely missed. It also implies that the Schwarzrand Subgroup in the Ai-Ais map sheet area was deposited more rapidly than the succession preserved in outcrops along the Orange River. (For interpretation of the references to colour in this figure legend, the reader is referred to the web version of this article.)

5.2. Possible solutions to resolve zircon U-Pb age discrepancies

5.2.1. Scenario 1: analyzed zircon from ash beds in the Swartpunt area do not approximate their eruptive ages

In total, high-precision, single-grain zircon U-Pb CA-ID-TIMS data from twelve ash beds have been published from the Urusis Formation and the informal 'lower' Nomtsas Formation in the Ai-Ais map sheet area (Fig. 11, Linnemann et al., 2019; Nelson et al., 2022, this study). Excluding the Nasep Member ash bed, which is older than the Bayesian age-depth framework for the NNP (Fig. 13B), and the informal 'lower' Nomtsas Formation ash bed which is visibly reworked, this amounts to 97 single grain analyses from ash beds of the Urusis Formation in the Swartpunt area, of which 52 have been used for the calculation of weighted mean ages based on the youngest coherent population of dates. Scenario 1 implies that many weighted mean ages from the Huns to Spitskop Members in the Swartpunt area are best interpreted as maximum depositional ages (Figs. 13, 14). This interpretation would better align with the Bayesian age-depth model derived from ash beds in the Urusis Formation of the NNP succession from Nelson et al. (2022), given that all ages derived from ash beds in this interval of the Swartpunt area succession, with the exception of sample FM41, are older than the predicated ages of the stratigraphy of that model (Fig. 13). If that

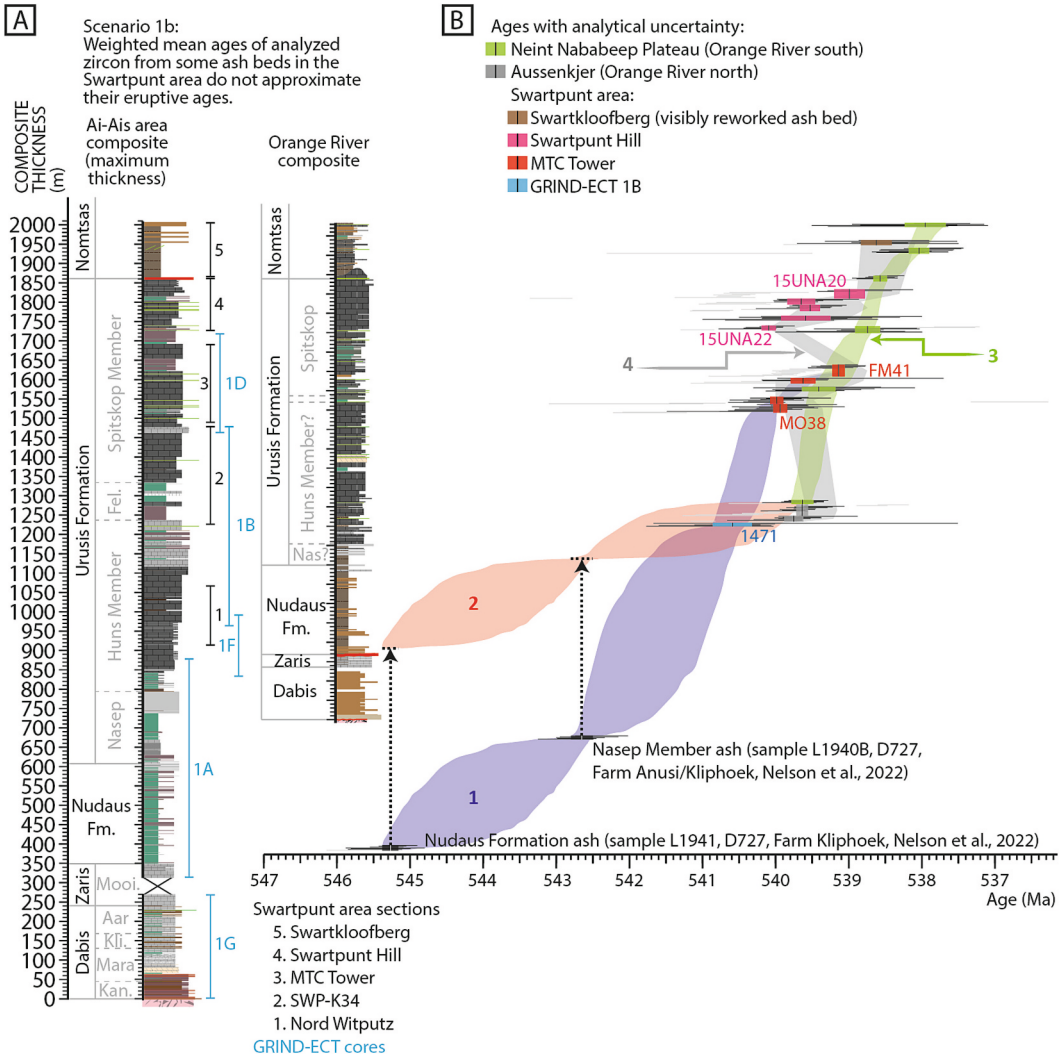

Fig. 14. Reconstructed correlation framework for the Urusis Formation following Scenario 1b. **(A)** Composite lithostratigraphic columns for the Ai-Ais map sheet area and the Orange River succession (expanded in Fig. S2). Framework extends from the depocenter to the seaward margin of the Witputs sub-basin, and southward to sections (Aussenkjer and the NNP) of the Orange River. Levels of Nudaus and Nasep ash beds in core 1A based on lithostratigraphic correlation to levels of dated ash beds in outcrop after Gong et al. (2025). **(B)** Weighted mean ages from ash beds presented in Linnemann et al. (2019), Nelson et al. (2022) and this study. Black horizontal lines are single grain analyses used in calculation of weighted mean ages; gray horizontal lines are single grain analyses not considered in weighted mean age calculations for the reasons stated in the text. Sample IDs are shown for key ash beds (refer to Fig. 11 for expanded ranked age plots). Shaded envelopes (for Bayesian age-depth models, these represent the 95 % confidence intervals): 1. Blue envelope shows the Bchron Bayesian age-depth model calibrated using weighted mean ages of ash beds from the Ai-Ais map sheet area, including those in the Nudaus Formation and Nasep Member of the Urusis Formation, in addition to the Huns and the Spitskop Members in GRIND-ECT core 1B and MTC Tower; 2. Orange envelope shows the Bchron Bayesian age-depth model calibrated using a combination of extrapolated weighted mean ages and positions of associated ash beds in the Nudaus Formation and Nasep Member in the Ai-Ais map sheet area and the age of the lowermost dated ash bed of the NNP succession after Nelson et al. (2022); 3. Green envelope shows the Bchron Bayesian age-depth model for the NNP after Nelson et al. (2022); 4. Gray envelope represents Bayesian eruption age (BEA) estimates for all newly reported weighted mean ages using bootstrapped distributions of single grains after Keller et al. (2018). Vertical dashed arrows show ash beds extrapolated between sub-basins for (2). This correlation implies that the majority of ash bed ages reported from the Spitskop Member in the Swartpunt area represent maximum depositional ages only, and that autocrystic zircon grain populations in these ash beds have been largely missed. However, it also implies that the Huns Member carbonate platform developed first in the vicinity of Swartpunt before migrating south (present co-ordinates). (For interpretation of the references to colour in this figure legend, the reader is referred to the web version of this article.)

Bayesian age-depth model, based on the geochronology interpretations of Nelson et al. (2022), accurately represents the chronostratigraphic framework, this suggests that only 11.5 % of all single crystal zircon dates used in the calculation of weighted mean ages (n = 6 of 52) from Urusis Formation ash beds in the Swartpunt area represent autocrystic populations that best approximate near-depositional ages.

If this model is accurate, it either implies: (1) that zircon distributions for the majority of ash beds in the Witputs sub-basin are skewed towards older ages by inheritance of either antecrystic or xenocrystic zircon domains, (2) inter-laboratory differences in pre-chemical abrasion optical zircon selection criteria led to biases in single crystal date populations and subsequent weighted mean ages of ash beds between studies and/or (3) the complete distribution of dates in individual ash beds was not sampled during analysis due to either insufficient analyses or biases associated with morphologies of zircon analyzed. Option 3 would imply that the zircon selection criteria employed by Nelson et al. (2022) more efficiently identified zircon morphologies that correspond to autocrystic grain populations, despite smaller n values per sample. Unfortunately, this is currently impossible to investigate fully, as zircon imagery was not provided in Linnemann et al. (2019) or Nelson et al. (2022). Regardless, any combination of these factors could offset the weighted mean ages to either older or younger than the ages of deposition, even when considering uncertainties on eruption age estimates using Bayesian methods (gray envelope on Figs. 13B and 14B). So, if Scenario 1 is true and many such ages are older than the ages of deposition, a cautious approach would be to consider all weighted mean ages and BEAs from ash beds to only ever represent maximum depositional ages.

5.2.2. Scenario 1: potential problems

The youngest autocrystic grains in an ash fall are commonly the least abundant and the smallest, because their crystallization pattern is restricted by the time spent in silica-rich melts prior to eruption (Crisp and Berry, 2022). Zircon grains from ash beds in the vicinity of Swartpunt that were selected for CA-ID-TIMS are small and show long prismatic, needle-like morphology (often with aspect ratios of <150:30), typical of later-stage zircon crystalized from silicic magma (Crisp and Berry, 2022). Therefore, it is extremely unlikely for differences in zircon grain size distribution based on volcanic processes (e.g., via density sorting during eruptive transport, Eychenne and Engwell, 2022) to be the cause of any differences in weighted mean ages between the Witputs and Orange River ash beds. Explaining the differences in zircon age populations between ash beds of the Swartpunt area and sections of the Orange River therefore could invoke: (1) post-depositional sedimentary reworking of ash beds in the Swartpunt area, for which no evidence has so far been reported, (2) an unconscious bias in optical zircon grain selection criteria, and/or (3) differing chemical abrasion procedures leading to variable efficiencies of Pb-loss mitigation. To fully discount sedimentary reworking would require a detailed sedimentological study of each ash bed in the Swartpunt area from outcrop, in addition to targeted intra-bed investigations that aim to verify and characterize vertical stratification or lateral variability of zircon age population distributions. If grain selection bias is not responsible, then a cautious approach would be to assume that weighted mean ages from ash beds in the Nudaus Formation and Nasep Member also represent maximum depositional ages derived from dominant antecrystic zircon populations or complex population distributions associated with sedimentary reworking. This would serve to increase the uncertainty on regional age-depth models, including those that rely on extrapolating ash bed data between the Ai-Ais map sheet area and Orange River succession. Finally, while all three studies did employ relatively rigorous conditions for chemical abrasion, due to the age and post-depositional history of these samples, there is potential for differing amounts of subtle Pb-loss to be present in each study. This is best demonstrated by the anomalously young dates in samples MO38 and FM73 in this study, and sample L1835–0 in Nelson et al. (2022) (Fig. 11). However, given the high frequency of overlapping dates at the youngest population within each sample from all three studies, we suggest that this is unlikely to have been the major mechanism causing differences between interpreted $^{206}Pb/^{238}U$ ages.

Based on the available evidence, Scenario 1 cannot easily account for the systematic repetition of younging-upwards ages recorded from the base of MTC Tower through to the top of Swartpunt Hill, especially given that the ages themselves form coherent clusters within analytical uncertainty between both units. Furthermore, based on published data, this appears to have only influenced zircon distributions in ash beds of the Swartpunt area and not sections of the Orange River, which is difficult to explain unless only the ash beds in the Swartpunt area underwent significant post-depositional reworking. Meanwhile, the corollary of invoking unconscious bias introduced during optical zircon selection would be that the stratigraphic repetition of dates is nothing but coincidental, and that adding more single grain dates may reveal true autocrystic populations for the Swartpunt area ash beds, given the tendency for larger numbers of single grain analyses to yield weighted mean dates that better approximate autocrystic populations (e.g., Condon et al., 2024).

5.2.3. Scenario 2: Gariep-related structural repetition and carbonate platform migration

Out-of-sequence ages in autochthonous successions may be more readily discounted as inheritance rather than a product of cryptic structural repetition. However, the same argument may be less valid for strata in allochthonous areas that are known to have experienced structural displacements in proximity to orogenic compression, such as the Swartpunt area. The MTC Tower and Swartpunt Hill sections are similar in lithostratigraphic architecture, the number and position of ash beds within each stratigraphic column, and ash bed ages. The Spitskop Member is comprised of alternating carbonate and siliciclastic units, and so any apparent lithostratigraphic repetition alone cannot be interpreted to reflect structural repetition due to overthrusting. However, ash beds were transported and deposited via a process entirely separate to carbonate-siliciclastic deposition, so the relative positions of ash beds within the stratigraphic architecture is notable. The lowermost ash interbeds of MTC Tower, core 1D and Swartpunt Hill are interbedded with carbonates and siliciclastics of variable thickness, whereas the upper ash beds in each profile occur across a short stratigraphic interval near the top of carbonate-dominated packages and immediately beneath thick siliciclastic units. When considering analytical uncertainty, the ages of the two basal ash beds in MTC Tower are indistinguishable from the 540.095 Ma age of sample 15UNA22 (basal Swartpunt Hill ash bed, Linnemann et al., 2019), and the ages of the two ash beds from the middle part of MTC Tower are indistinguishable from the ages of the four dated ash beds in the middle of Swartpunt Hill.

If each weighted mean U-Pb age faithfully approximates a near-depositional age, then the ten high-precision zircon U-Pb CA-ID-TIMS ages from the upper unit of the Huns Member through Spitskop Member of the LTP in the Swartpunt area lead to two conclusions. First, they would confirm that the Huns Member in the Swartpunt area was largely deposited prior to 540.591 ± 0.269 Ma. Second, that age repetition between E13–15 and E17 is associated with stratigraphic repetition. Visible thrust faults in this area strike NW-SE and dip to the WSW, consistent with northeast convergent compression driven by the Gariep orogeny (Saylor and Grotzinger, 1996). Compressional features in E17 (e.g., Fig. 9F) cannot, by themselves, be used to invoke long-range displacement within E17–18 given that they are also an expected result of Gariep-related compression, which would have affected the entire LTP. However, if each age is assumed to approximate the timing of deposition of each respective ash bed, then, considering the regional structural context, the observed age repetition may suggest that the entirety of E18 and at least the upper half of E17 on the LTP represent the remains of a nappe formed by overthrusting and long-range displacement of E13–E16 (Figs. 15, 16).

The Spitskop Member in the Swartpunt area was deposited as a mixed carbonate-siliciclastic ramp (Fig. 16A, Saylor and Grotzinger, 1996). In Scenario 2, compression and fault propagation culminated in delamination of E13–E16 in the hinterland, which were overthrust and transported across the top of a mechanically weak (incompetent) siliciclastic layer. The décollement surface in this scenario would therefore be invoked within the siliciclastic package that constitutes the lower part of E17, below the 540.095 Ma ash bed (Fig. 16B). The leading edge of the resulting nappe, which would have been situated to the northeast of Swartpunt Hill, has since been removed by erosion in this model. This displacement would then have been followed by continued out-of-sequence overthrusting of the Huns Member and lower part of the Spitskop Member (Fig. 16C), along fault 'B' and by splay along fault 'A' (after Saylor and Grotzinger, 1996, Fig. 16D). A localized, buried displacement along fault 'C' upwarped units to form an anticline beneath the Huns klippe, and progressive displacement along the leading edge of fault 'C' separated the LTP from the autochthon to the east of Swartpunt Hill (Figs. 15, 16D). Compression of the UTP led to broad-scale folding of the Kuibis Subgroup on Farm Nord Witputz and along strike to the northwest, and subsequent erosion of overlying units resulted in exposure of modern topography (Figs. 16E, S7b). Ultimately, the model suggested by Scenario 2 is consistent with that originally proposed by Saylor and Grotzinger (1996) but adds one step of in-sequence imbricate fault propagation (Fig. 16B) prior to their oldest fault displacement (Fig. 16C). Hypothetical fault 'D' would thus represent the oldest Gariep-related thrust fault in this area known to date.

If Scenario 2 is correct, it would also help to explain the considerable differences in lateral thickness of the Spitskop Member, which has long been recognized between the UTP, MTP and LTP, and which has been interpreted to result from an exaggerated distal steepening of the Spitskop Member carbonate ramp (Saylor and Grotzinger, 1996). This scenario may also explain the apparent absence of the carbonate-dominated upper half of E17 and the entirety of E18 from the autochthon to the east, if these units have not simply been removed by erosion (Saylor, 2003).

This model would resolve ash bed age repetition and cannot be easily discounted based on available data given the tectonic regime of the Swartpunt area, which was subject to northeast-vergent Gariep-related compression. This suggests that E17 (at least from beneath the lowermost dated ash bed) to the top of E18 could encompass repeated strata (E13–16) that were transported as a nappe. However, given that subsequent erosion has separated numerous cuestas, each of these would now be more accurately described as klippes (Fig. 15).

5.2.4. Scenario 2: potential problems

The considerable planar displacement required by Scenario 2 along décollement 'D' (ca. 7 km, Figs. 15, 16B) appears at first to be inconsistent with the generally high angle of exposed fault planes (e.g., faults 'A' and 'B' and the frontal displacement of fault 'C'). However, even faults 'A' and 'B' have been reconstructed with an initial ramp-flat geometry, and fault 'C' is primarily reconstructed as a buried thrust flat (Saylor and Grotzinger, 1996). In Scenario 2, the ramp of fault 'D' is not preserved, but décollement 'D' represents the thrust flat that underlies the hanging wall flat (consisting of E18 and upper E17) which formed at a time when the tectonic regime was dominantly thin-skinned, in advance of movement along out-of-sequence fault 'B'. Out-of-sequence thrusting is also evident in the model of Saylor and Grotzinger (1996), whereby displacement along fault 'B' and emplacement of the Huns klippe atop the LTP predated splay 'A'. The initial in-sequence model that led to décollement 'D' would be analogous to the development and morphology of thin-skinned imbricate thrust systems in frontal zones of other orogenic belts (e.g., Bally et al., 1966). If this scenario is correct, then the imbricate thrust system in the hinterland, which would theoretically have originally overlain deposits of the UTP and MTP (e.g., Fig. 16B, C), has since been removed by erosion.

The most significant issue with Scenario 2 is undoubtedly the absence of any visible evidence in outcrop for displacement within the lower half of E17, which is inferred to have been the footwall. Displacement distances on the order of kilometers would be expected to result in disrupted bedding of incompetent strata that underlie the décollement surface. If Scenario 2 is preferred, then the cryptic nature of this décollement is evident by the fact that it has not been identified in outcrop despite over 30 years of field study in the Swartpunt area. As noted in Section 4.1.3, evidence for compression in section SWP-AB31 (Figs. 9E, F, 10A) is insufficient to argue for long-range nappe transport because compression of the LTP would also be expected during faulting of 'A' and 'B'. Slumping of siliciclastics in SWP-AB31 and Swartpunt Hill may similarly have resulted from distal slippage during formation of the anticline beneath the Huns klippe, which was driven by subsurface movement along fault 'C'. The 540.095 Ma ash bed is overlain by a thin unit of siliciclastic strata, which may also be expected to record evidence for disruption during long-range nappe transport. Unlike the middle fossil-bearing siliciclastic unit of Swartpunt Hill (lower part of medium-scale sequence E18), which has been described as a "mega-slump" (Narbonne et al., 1997; Darroch et al., 2015), the sedimentology of the siliciclastic interval at the base of Swartpunt Hill and neighboring sections has received comparatively little attention by sedimentologists but does show evidence for localized broad-scale folding to the southwest of Swartpunt Hill (e.g., SWP-AB31, Fig. 9E).

In the thought experiment of Scenario 2, in order to resolve age repetition, the décollement surface must underly the lowermost ash bed at Swartpunt Hill, dated to 540.095 Ma by Linnemann et al. (2019). The lack of clear outcrop evidence for displacement beneath this ash bed is either because it does not exist, or it may be due, in part, to bedding-parallel displacement along the décollement surface and cover of tectonically disrupted strata in the footwall by intense weathering of siliciclastic rocks in lower E17. Ideally, a décollement surface would be identifiable in unweathered core from the uppermost part of GRIND-ECT 1D (Figs. 5B, 10A). However, the core collar of 1D underlies the ash bed at the base of Swartpunt Hill by several meters (Fig. 10A) and the uppermost ca. 10 m of core are composed of brecciated calcrete where original bedding features and original lithological composition are obscured. The underlying unit of sandstone and siltstone in core 1B, which corresponds to the lower half of medium-scale sequence E17, contains thick intervals that lack clearly defined bedding planes and laminations in cross-section. It is therefore possible that the décollement surface is present but remains cryptic, even in available core material. Focused future field study is required to fully discount the possibility that the décollement surface has been missed, and this would also benefit from attempts to fingerprint the bulk geochemistry of ash beds using trace element concentration data (e.g., Saylor et al., 2005). Based on the lack of available evidence from outcrop, Scenario 2 can only be viewed as a thought experiment.

5.2.5. Indulging Scenario 2: relative timing of Gariep-related displacements

Seven ash beds through the Urusis Formation in the Swartpunt area and Orange River successions yielded weighted mean ages of ca. 539.6 Ma, unresolvable from one another within analytical uncertainty (Figs. 11, S1, S2, ages reported herein, in Linnemann et al., 2019, and in Nelson et al., 2022). Ash beds with this age have been identified in the middle part of the Spitskop Member (E15) at MTC Tower, the Spitskop Member (E17) at Swartpunt Hill, the middle part of the Urusis Formation at Aussenkjer, and the lower part of the Urusis Formation of the NNP composite section (Figs. 11 and S1). Available ash bed ages also confirm ongoing mixed siliciclastic-carbonate deposition in the NNP succession until <538 Ma (Figs. 13B, 14B, 17B, Nelson et al., 2022). *Re*-analyzed zircon grains from the reworked ash bed on Farm Swartkloofberg (sample SWART7, Figs. 2C, 11, S1, S2, S3F) yield a weighted mean age of 538.62 ± 0.21 Ma, indistinguishable within analytical uncertainty from the age of the informal 'lower' Nomtsas Formation ash bed on the NNP reported by Nelson et al. (2022), sample L1832–0, Fig. 11). Thus, consistent with visible evidence for transport of silicified

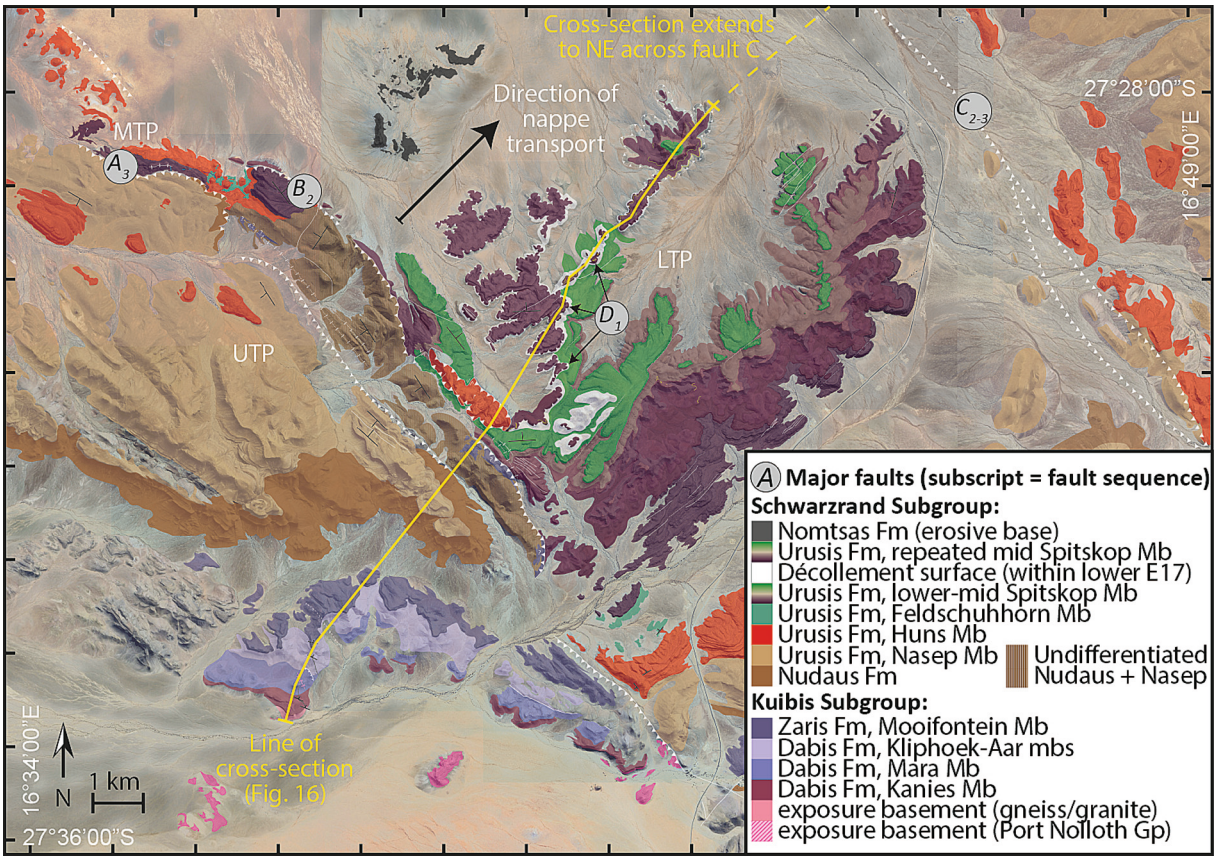

Fig. 15. Alternative geological map for the Swartpunt area inferred in 'Scenario 2' (expanded in Fig. S7b). Map shows the areal extent of outcrop that constitutes repetition of medium-scale sequences E13–16 in the Spitskop Member. The prominent darker green horizon is the top of medium-scale sequence E16. Hypothesized nappe transport along décollement [D] suggested by systematic zircon U-Pb age repetition through medium-scale sequences E13–E18 if all weighted mean ages are assumed to represent near-depositional ages. Mechanism for nappe emplacement is consistent with the regional tectonic regime associated with northeast-vergent Gariep-related compression, as discussed in the text. Yellow line marks cross-section of Fig. 16. Fm. – Formation; Mb. – Member; mbs. – Members. (For interpretation of the references to colour in this figure legend, the reader is referred to the web version of this article.)

ash material, we interpret the ash bed in the Swartkloofberg section to have been reworked and transported from underlying strata equivalent in age to the 'lower' Nomtsas Formation on the NNP. On farms Swartpunt and Swartkloofberg, in-situ 'lower' Nomtsas Formation deposits of this age (i.e., strata preserving the SWART7 ash bed in-situ) have been lost through erosion prior to or during deposition of the Nomtsas Formation conglomerate in this area (Figs. 13B, 14B, 16C, 17B, S1, S2, Saylor and Grotzinger, 1996).

No outcrops of E17 or E18 preserve direct evidence for an unconformable contact with the Nomtsas Formation conglomerate on the LTP. The contact is not exposed at the base of outcrops of the Nomtsas conglomerate to the west of Swartpunt Hill, largely due to structural dip and burial beneath alluvium (Figs. 5B, 15, S7). However, Saylor and Grotzinger (1996) proposed that this Spitskop-Nomtsas unconformity may correlate with a dolomitized and brecciated horizon near the base of the carbonate-dominated upper part of E17, which outcrops at the summit of section SWP-AA28 (Figs. 5B, 9C), thereby inferring up to 120 m of erosion on the LTP. In Scenario 2, nappe emplacement of E18 and upper E17 would have occurred prior to or broadly coincident with deposition of the Nomtsas conglomerate, because this model requires displacement along a planar décollement surface of minimal resistance.

The sub-Nomtsas Formation erosional unconformity has previously been linked with relative sea level fall on the order of several tens to even hundreds of meters, and the 'lower' Nomtsas Formation conglomerate itself has been interpreted as debris shed from incised valleys that formed during relative sea level fall, with sediment gravity flows depositing some material into deeper marine settings of the UTP (Saylor, 1993; Saylor et al., 1995; Saylor and Grotzinger, 1996). Saylor and Grotzinger (1996) suggested that the sub-Nomtsas Formation unconformity may, in part, reflect eustatic sea level fall, given its expression both on the uplifting eastern edge and rapidly subsiding western edge of the Witputs sub-basin, and through recognition that several globally distributed successions record erosive unconformities in carbonates that immediately underlie Cambrian strata (e.g., Runnegar et al., 1995). However, this remains highly speculative. Instead, increasing accommodation space during deposition of the Spitskop Member and submarine slope failure associated with the Spitskop-Nomtsas unconformity in the Swartpunt area may both have been driven by progressive flexural subsidence during Gariep orogenesis (Fig. 16C). Active flexural subsidence has also been invoked to explain relative deepening at the Spitskop-Nomtsas contact on the NNP (Nelson et al., 2022).

The youngest age from the Spitskop Member on the LTP is ca. 538.99 ± 0.21 Ma (Fig. 11B, Linnemann et al., 2019), and ash beds reworked from underlying units during deposition of the Nomtsas Formation on the MTP yielded an age of 538.62 ± 0.21 Ma. Radioisotopic and stratigraphic data from the NNP show that transgressive 'lower' Nomtsas Formation deposits, which either predate regional base level fall or coincide with a pulse of Gariep-related flexural subsidence in the Witputs sub-basin, are as young as 537.95 ± 0.28 Ma (Fig. 11B, Nelson et al., 2022). In Scenario 2, the available radioisotopic ages allow ≥1 Myrs for nappe transport on the LTP prior to the onset of regional base level fall.

Nomtsas Formation siliciclastic rocks in the Swartpunt area have

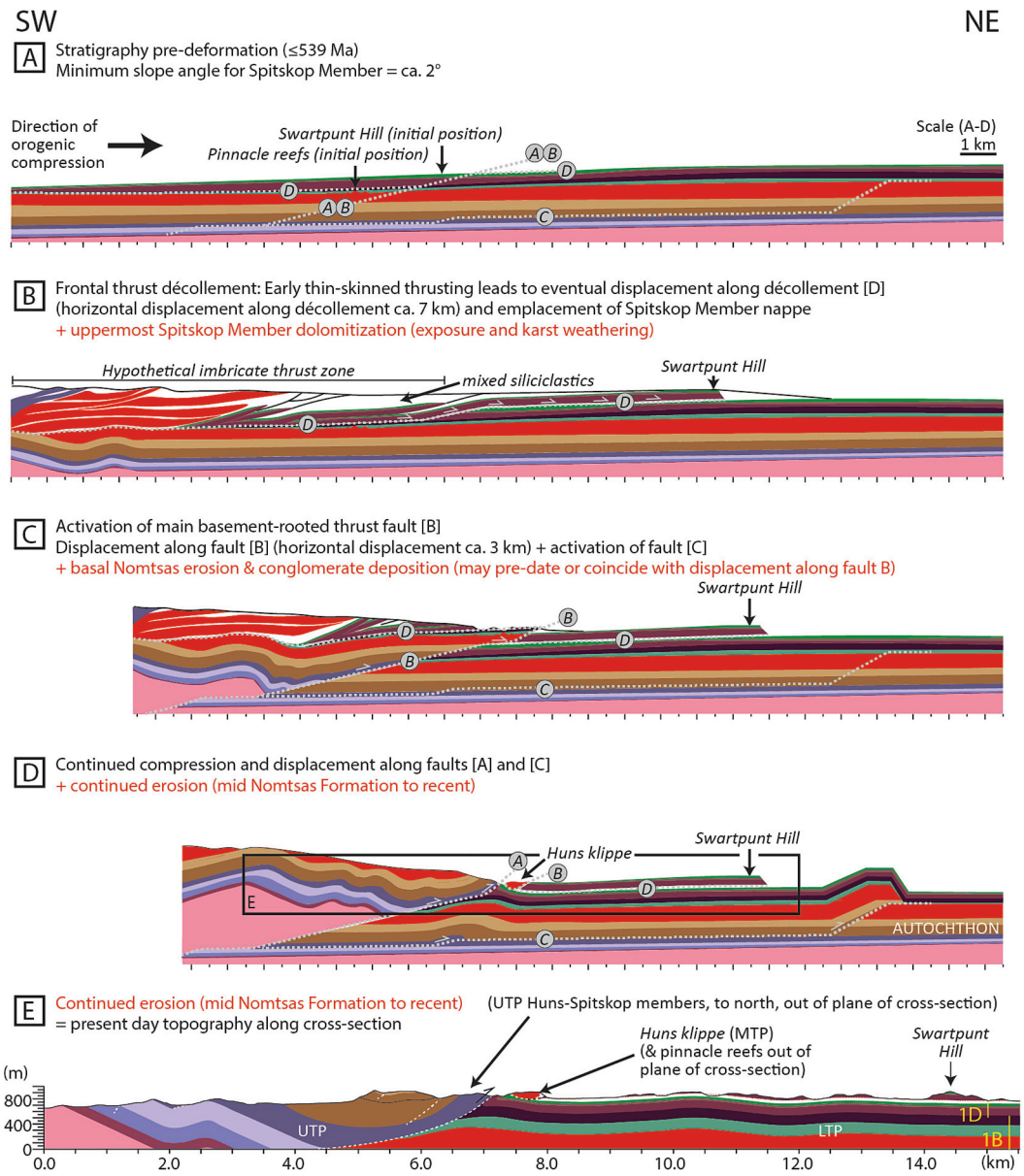

Fig. 16. Schematic illustration showing hypothesized tectonostratigraphic evolution in the Swartpunt area according to 'Scenario 2'. **(A)** Pre-deformational layer-cake stratigraphic architecture of the pre-Nomtsas succession in the southwestern Witputs sub-basin. **(B)** Incipient far-field Gariep compression results in a frontal zone of imbricated thrust faults and repetition of medium-scale sequences E13–16, with décollement surface [D] parallel to bedding along mechanically weak horizon that now constitutes the siliciclastic-dominated part of lower medium-scale sequence E17. **(C)** Major displacement along deeper-rooted fault [B] separates the MTP from the LTP. **(D)** Up-warp created via compression along fault [C] and displacement along splay [A] of fault [B] distinguishes the UTP from MTP and leads to the formation of the Huns klippe. Continued erosion removes overlying strata from the upper, middle and lower thrust plates. Erosion associated with the Spitskop-Nomtsas unconformity in this area initially occurred either via relative sea level fall, subaerial exposure and fluvial incision or submarine slope failure and mass wasting (Saylor and Grotzinger, 1996), but significant erosion and removal of material has continued over the subsequent ca. 538 Ma. **(E)** Geological cross-section, showing modern topography, with Huns klippe, upper part of the Spitskop nappe, and differential preservation of strata between the upper and lower thrust plates (full high-resolution map and cross-section provided in Fig. S7b). Fault evolution in panels (C) and (D) follow sequence described and illustrated in Saylor and Grotzinger (1996).

previously been interpreted to record diachronous deposition during marine transgression (Saylor and Grotzinger, 1996). In eastern sections of the Witputs sub-basin, siliciclastic rocks mapped as the Nomtsas Formation contain *T. pedum* above a series of nested erosional unconformities (Fig. S2; Wilson et al., 2012). Youngest detrital zircon ages from fossiliferous deposits in the Great Basin constrain the lowest regional occurrence of *T. pedum* to ≤533 Ma, near the base of the Laurentian Sauk transgression (Sloss, 1963; Nelson et al., 2023). If siliciclastic rocks above the Nomtsas Formation conglomerate on the MTP were deposited prior to lowest regional occurrence of *T. pedum*, and if currently available radioisotopic ages from Laurentia approximate the maximum age of global *T. pedum* first appearance, then these siliciclastic rocks were most likely deposited after 537.95 Ma and in advance of Sauk transgression. Therefore, we caution that, notwithstanding environmental and facies biases on habitability and fossil preservation, it is extremely difficult to confidently differentiate intervals of eustatic sea level rise within the Nomtsas Formation from active flexural warping associated with Gariep orogenesis. Future studies may benefit from integrating maximum depositional ages of *T. pedum*-bearing deposits in the Nama Group using youngest single grain detrital zircon CA-ID-TIMS

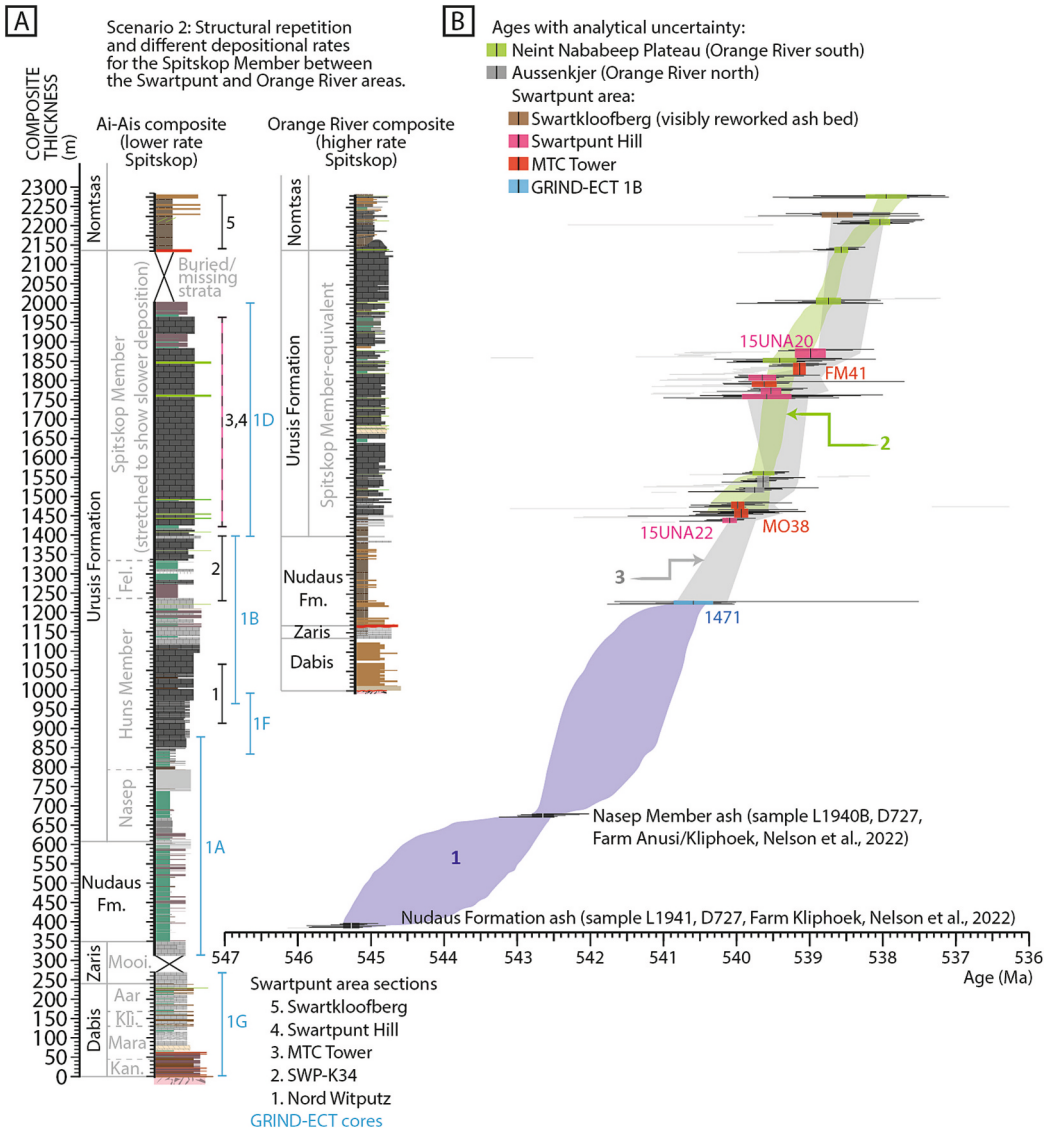

Fig. 17. Reconstructed correlation framework for the Urusis Formation following Scenario 2. **(A)** Composite lithostratigraphic columns for the Ai-Ais map sheet area and the Orange River succession. Framework extends from the depocenter to the seaward margin of the Witputs sub-basin, and southward to sections (at Aussenkjer and the NNP) of the Orange River. Levels of Nudaus and Nasep ash beds in core 1A based on lithostratigraphic correlation to levels of dated ash beds in outcrop after Gong et al. (2025). In this figure, the lithostratigraphic profile for the Spitskop Member in the Swartpunt area has been stretched to visualize the lower depositional rate inferred by weighted mean ages of ash beds from this area relative to the Orange River succession, allowing Swartpunt area ash beds to overlap with the Bayesian age-depth model for the NNP. **(B)** Weighted mean ages of ash beds from Linnemann et al. (2019), Nelson et al. (2022) and this study. Black horizontal lines are single grain analyses used in calculation of weighted mean ages; gray horizontal lines are single grain analyses not considered in weighted mean age calculations. Sample IDs are shown for key ash beds. Shaded envelopes (for Bayesian age-depth models, these represent the 95 % confidence intervals): 1. Blue envelope represents the Bchron Bayesian age-depth model calibrated using weighted mean ages from ash beds in the Ai-Ais map sheet area, including those in the Nudaus Formation and Nasep Member of the Urusis Formation, in addition to the Huns and the Spitskop Members in GRIND-ECT core 1B and MTC Tower; 2. Green envelope shows the Bchron Bayesian age-depth model for the NNP after Nelson et al. (2022); 3. Gray envelope represents Bayesian eruption age (BEA) estimates for all newly reported weighted mean ages in the Swartpunt area using bootstrapped distributions of single grains after Keller et al. (2018). This correlation permits all weighted mean ages of youngest grain populations to approximate the timing of deposition within analytical uncertainty but requires structural repetition of the Spitskop Member in the vicinity of Swartpunt, and lower depositional rates in the Swartpunt area relative to sections along the Orange River during deposition of the Spitskop Member. In this reconstruction, the Huns Member carbonate platform largely developed in more northerly areas (present co-ordinates) and migration of the locus of active tectonic subsidence, from large-scale sequences D and E -onward, led to progressive migration of the carbonate platform to the south during deposition of the Spitskop Member. (For interpretation of the references to colour in this figure legend, the reader is referred to the web version of this article.)

analyses.

5.3. Regional $\delta^{13}C_{carb}$ correlation and carbonate platform migration

Regional stratigraphic correlations between the Swartpunt area and the NNP that result from Scenario 1 (scenarios 1a and 1b, Figs. 13 and 14) and Scenario 2 (Fig. 17) yield significantly different regional composite chemostratigraphic profiles (Fig. 18 and Table S4). Each correlation follows the alignment of medium-scale sequences between sections of the MTP and LTP after Saylor (2003). The age framework for the NNP in each scenario is within the uncertainty envelope of the Bayesian age-depth model presented by Nelson et al. (2022). Given that carbon isotope data of the Urusis Formation lack distinctive positive/negative anomalies to aid correlation, it is not possible to use the chemostratigraphic data alone to favor one scenario over another. However, there is some consistency of structure in the $\delta^{13}C_{carb}$ composite, which is

replicated between sections of the Witputs sub-basin and evident in the comparison of composite sections between the Swartpunt area and sections along the Orange River (Fig. 18).

The first of these chemostratigraphic models follows the correlation of Members of the Urusis Formation after Nelson et al. (2022)- their Fig. 9), whereby the age of the base of the Huns Member is approximately equivalent between the Swartpunt area and NNP (Scenario 1a; Figs. 13, 18A). This scenario requires that all ash bed ages from the Huns-Spitskop Members of the Swartpunt area record maximum depositional ages only, with the exception of sample FM41, and that the average depositional rate of the Huns Member through lower part of the Spitskop Member in the Swartpunt area was greater than equivalent deposits of the NNP (Fig. 13B). An intermediate model that utilizes some of the tenets of that model is Scenario 1b, which still assumes that the majority of ash beds in the Spitskop Member of the Swartpunt area yield maximum depositional ages but allows for the age of sample 1471 from the upper part of the Huns Member to approximate the age of deposition (Figs. 14B, 18B). This alternative correlation does not require structural repetition in the Swartpunt area, or considerable differences in average depositional rate of the Huns through lower Spitskop Members between the Swartpunt area and sections of the Orange River. However, it would imply that the base of the Huns Member in the Swartpunt area is older than the lower carbonate-dominated unit of the Urusis Formation along the Orange River (i.e., the Huns Member was largely deposited in the north with minimal laterally equivalent carbonate deposition further to the south of present co-ordinates). Finally, as an alternative chemostratigraphic model, Scenario 2 allows all weighted mean zircon U-Pb dates from the Swartpunt area to represent near-depositional ages within analytical uncertainty, with the exception of the visibly reworked ash bed of sample SWART7, but this scenario requires structural repetition between MTC Tower and Swartpunt Hill (Figs. 17, 18C).

For chemostratigraphic alignments shown in Fig. 18B and C, the base of Nord Witputz and core 1B profiles are set to their respective minimum ages within the 95 % confidence interval of the Bayesian age-depth model shown in Figs. 14B and 17B (Table S4). Both scenarios 1b and 2 are therefore consistent with a model whereby deposition of the Huns Member carbonate platform was largely restricted to the Ai-Ais map sheet area > 540 Ma (Figs. 14, 17). Scenario 2 also requires that the mid-upper part of the Spitskop Member in the Swartpunt area was deposited more slowly than the Huns Member and lower part of the Spitskop Member, and also more slowly than equivalent strata of the Spitskop Member on the NNP (Fig. 17).

Large-scale sequences D and E, which encompass the Feldschuhhorn and Spitskop Members, are interpreted to record accommodation space increase driven by tectonic flexure (Saylor, 2003). The onset of this flexure may have led to progressive accommodation space increase from north to south (present co-ordinates) and gradual southward migration of the locus of carbonate platform development from the Swartpunt area to NNP, consistent with the original interpretations of Germs and Gresse (1991) and Gresse and Germs (1993). Subsequent activation of the Koedoelaagte arch, as well as the Pella arch further to the south, occurred prior to and during deposition of the Cambrian Fish River Subgroup, respectively (Fig. S2, Germs and Gresse, 1991). Orogenic compression, which drove a pulse of flexural subsidence and relative sea level rise recorded by deposition of 'lower' Nomtsas Formation in the NNP succession (Nelson et al., 2022), could also have driven incipient frontal thrust displacement in the Swartpunt area in Scenario 2 (e.g., between panels A and B of Fig. 16).

5.4. Ash bed provenance and orogenesis

The Hf isotope data reported herein from the same dated zircon crystals have a temporal shift from εHf values of +1 in the Hoogland Member at ca. 547 Ma, towards scattered and negative εHf values in zircon grains from the Urusis and Nomtsas Formation ash beds between ca. 540 Ma and 538.62 Ma (Fig. 12). The evolution of these zircon εHf compositions may reflect a transition from a magmatic-arc source with a proportionally greater contribution from the depleted mantle at ca. 547 Ma (Fig. 19A–C), towards a greater contribution of crustal melts during later-stage continental collision by ca. 540 Ma (Fig. 19D).

Units that formed during the multi-stage Damara orogeny to the (present) north of the Nama Group are geographically subdivided from north to south into the northern (Outjo) zone, central (Swakop) zone, southern (Khomas) zone, and Hakos zone (Fig. 19A; Barnes and Sawyer, 1980; Johnson et al., 2006; Miller, 2008; Foster and Goscombe, 2013). The Outjo zone records initial collision of the Swakop terrane with the Congo craton, to the north, while the Khomas zone represents a SSE-facing accretionary prism that formed during continental collision of the Swakop zone with the Kalahari craton to the south (Hoffman et al., 2021). The Hakos zone represents deformed Kalahari basement (Miller, 2008; Hoffman et al., 2021).

The Zaris sub-basin represents a foredeep that formed as a result of flexural subsidence, which persisted until at least ca. 547 Ma, based on the age of the Hoogland Member ash bed and localized rapid subsidence of the underlying Omkyk Member in the vicinity of the Driedoornvlakte bioherm to the present northeast (Figs. 19E, S1; Smith, 1999). The Hoogland Member ash bed was likely derived from a magmatic arc that formed during closure of the narrow Khomas seaway between the Kalahari craton and Swakop zone (de Kock et al., 2000; Miller, 2008; Hoffman et al., 2021). This series of events is consistent with geochemical characteristics and paleocurrent data from sedimentary rocks that record subsequent infill of the Zaris sub-basin driven by gradual unroofing of the Damara hinterland (Fig. 19C; Germs, 1983; Gresse and Germs, 1993; Blanco et al., 2009, Blanco et al., 2011). Analyses of detrital chromian spinels (Blanco et al., 2009) indicate that some detrital materials in the lower part of the Nudaus Formation (ca. 545.27 Ma after Nelson et al., 2022) were derived from an arc setting which, together with paleocurrent data (Germs, 1983), implies exhumation and erosion of a relic arc that existed within the Damara orogenic belt (Fig. 19C).

The negative zircon εHf compositions in the Urusis Formation may support an origin of the volcanic zircon from a continental arc-type setting during gradual closure of the Khomas Sea and with a significant melt contribution from continental crustal reservoirs (Fig. 19D, F). Importantly, this model does not necessarily require additional ash contribution from volcanism associated with the Gariep orogeny (e.g., Fig. 19G), although this cannot be discounted. An invariant ash bed provenance from the Damara orogenic belt may be further supported if zircon εHf values from the Nudaus Formation and Nasep Member ash beds are of intermediate composition relative to values reported herein from underlying and overlying ash beds.

5.5. Geochronological constraints on Nama Group carbonate platform migration

Full integration of all published high-precision zircon U-Pb CA-ID-TIMS data from the Nama Group, alongside stratigraphic and geochemical data that inform on the dynamics of basin formation and sediment infill, reveal a coherent pattern of evolving collision-related subsidence and associated carbonate platform migration through time (Fig. 20). Studies of Nama Group stratigraphic architecture have shown that the locus of carbonate platform development migrated southward as a consequence of gradual infill of the Zaris sub-basin and a southward shift in the locus of active subsidence (Fig. 19C; Germs, 1983; Gresse and Germs, 1993). Our compilation of high-precision zircon U-Pb dates, in addition to outcrop and core correlation, appears to support canonical reconstructions of carbonate platform migration from the Zaris to Witputs sub-basins, with the youngest carbonate-dominated units deposited in the vicinity of the NNP (Figs. 19, 20, S1).

Diachronous transgression across the crystalline Kalahari basement during deposition of the Kuibis Subgroup first led to deposition of coarse shoreface siliciclastic sediments, followed by shallow, semi-restricted

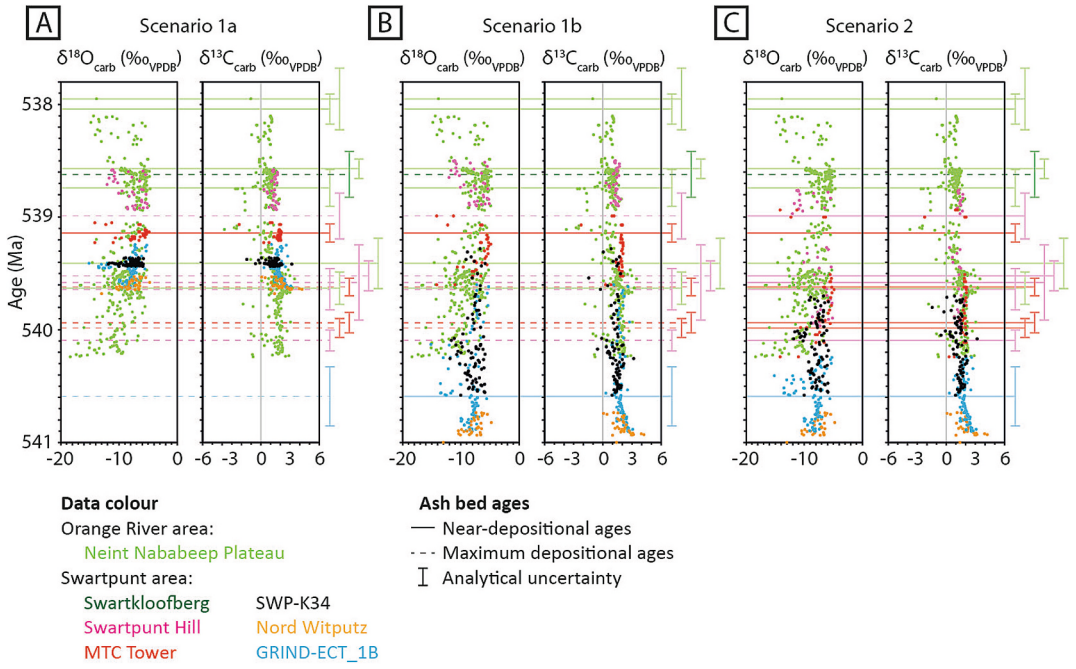

Fig. 18. Temporal alignment of all $\delta^{13}C_{carb}$ and $\delta^{18}O_{carb}$ data resulting from **(A)** Scenario 1a whereby all weighted mean ages from ash beds in the Huns-Spitskop Members in the Swartpunt area (with the exception of sample FM41) yield maximum depositional ages only due to dominant antecrystic zircon populations (correlation follows Fig. 9 of Nelson et al., 2022), **(B)** Scenario 1b whereby the majority of weighted mean ages from ash beds of the Spitskop Member in the Swartpunt area (with the exception of sample FM41) yield maximum depositional ages only due to dominant antecrystic populations, but sample 1471 from the uppermost part of the Huns Member yields a near-depositional age implying that the Huns Member is older in the Swartpunt area than in sections along the Orange River, and **(C)** Scenario 2, whereby all ash beds in the Witputs sub-basin (with the exception of reworked sample SWART7) yield near-depositional ages, assuming structural repetition in the Swartpunt area. Data and model ages for each scenario are provided in Tables S1 and S4. Carbon and oxygen isotopic data are from Bowyer et al. (2022), Nelson et al. (2022) and this study. Ash bed ages and uncertainties represent weighted mean ages of youngest single grain populations, not BEAs.

and often dolomitic carbonate, and finally by open-marine limestone and interbedded fine-grained siliciclastic sediments across the Zaris and Witputs sub-basins (Fig. 20A, B, Germs, 1983; Saylor et al., 1995; Bowyer et al., 2023). At that time, flexural subsidence was most pronounced in the northern Zaris sub-basin, as evidenced by continuous deposition of thick carbonate sequences proximal to ongoing collision along the Damara orogenic belt (Figs. 19B, 20B, C; e.g., Saylor et al., 1998; Smith, 1999; Wood et al., 2015). Zircon εHf compositions from the ash bed in the lower part of the Hoogland Member also indicate derivation from an active magmatic arc (Fig. 19B).

The lithostratigraphic architecture of the Zaris and Witputs sub-basins differ during deposition of the Zaris Formation, which is exemplified by carbonate-dominated deposition of the Hoogland Member in the Zaris sub-basin and possibly equivalent siliciclastic-dominated deposition of the lower interval of the Nudaus Formation in distal areas of the Witputs sub-basin (Figs. 3, 20B, S1, S2). This model suggests that siliciclastic sediments of the lower part of the Nudaus Formation in the deeper western areas of the Witputs sub-basin (e.g., core 1A) may have been deposited coincident with Urikos Member siliciclastics in the Zaris sub-basin, and that deposition of the lower part of the Nudaus Formation may have been diachronous from west to east until ca. 545.27 Ma (Nelson et al., 2022). Alternatively, shales of the lowermost interval of the Nudaus Formation in the Witputs sub-basin may represent condensed deposition, or a depositional hiatus exists in the Witputs sub-basin of up to ca. 1.5 Ma between the uppermost part of the Mooifontein Member and the 545.27 Ma ash bed of the lower part of the Nudaus Formation, equating to the estimated maximum duration of Hoogland Member deposition.

The onset of gradual Zaris sub-basin infill during narrowing of the Khomas Sea corresponded with a major southward shift in the position of the main Damara flexural foredeep into the Witputs sub-basin (Figs. 19C, 20D). This interval may also have been associated with major uplift parallel to the Koedoelaagte Arch, which may in turn have led to localized erosion and deposition of the lowermost conglomerate of the Nudaus Formation (so-called 'Vingerbreek diamictite') at Aussenkjer (Gresse and Germs, 1993). Importantly, this tectonic mechanism does not require a glacial origin for the Vingerbreek diamictite. However, the reconstructed timing of ca. 545 Ma for the erosional event also corresponds approximately to the onset of a possible hiatus in carbonate deposition across each sub-basin (Fig. 20B, D), which may also allow for a short-lived regional glaciation (e.g., Germs and Gaucher, 2012). After ca. 545 Ma, the locus of carbonate deposition permanently shifted towards the south of the Osis Arch, into open marine settings where accommodation space was created through ongoing flexural subsidence in areas and at times of lower relative siliciclastic input (Figs. 19C, D, 20D, E).

In the Swartpunt area, both scenarios 1b (Figs. 14, 18B) and 2 (Figs. 17, 18C) imply initial development of the Urusis Formation carbonate platform prior to 540 Ma, corresponding to deposition of the lower interval of the Huns Member. At that time, significant collision-related underplating of the Damara orogenic belt may also be suggested by lower zircon εHf values (Figs. 12). In Scenario 1b, earlier deposition of the Huns Member in the Swartpunt area is supported by the ages and younging-upward sequence of ash beds in the Huns Member through the lower-middle interval of the Spitskop Member of core 1B and MTC Tower, but maximum depositional ages are interpreted for out-of-sequence ages recorded by ash beds in the upper part of the Spitskop Member at Swartpunt Hill. In Scenario 2, all new and published ash bed ages are interpreted as near-depositional ages, but cryptic structural repetition is invoked between MTC Tower and Swartpunt Hill. While these two models are contingent upon at least some of the ages reported from the Swartpunt area to approximate near-depositional

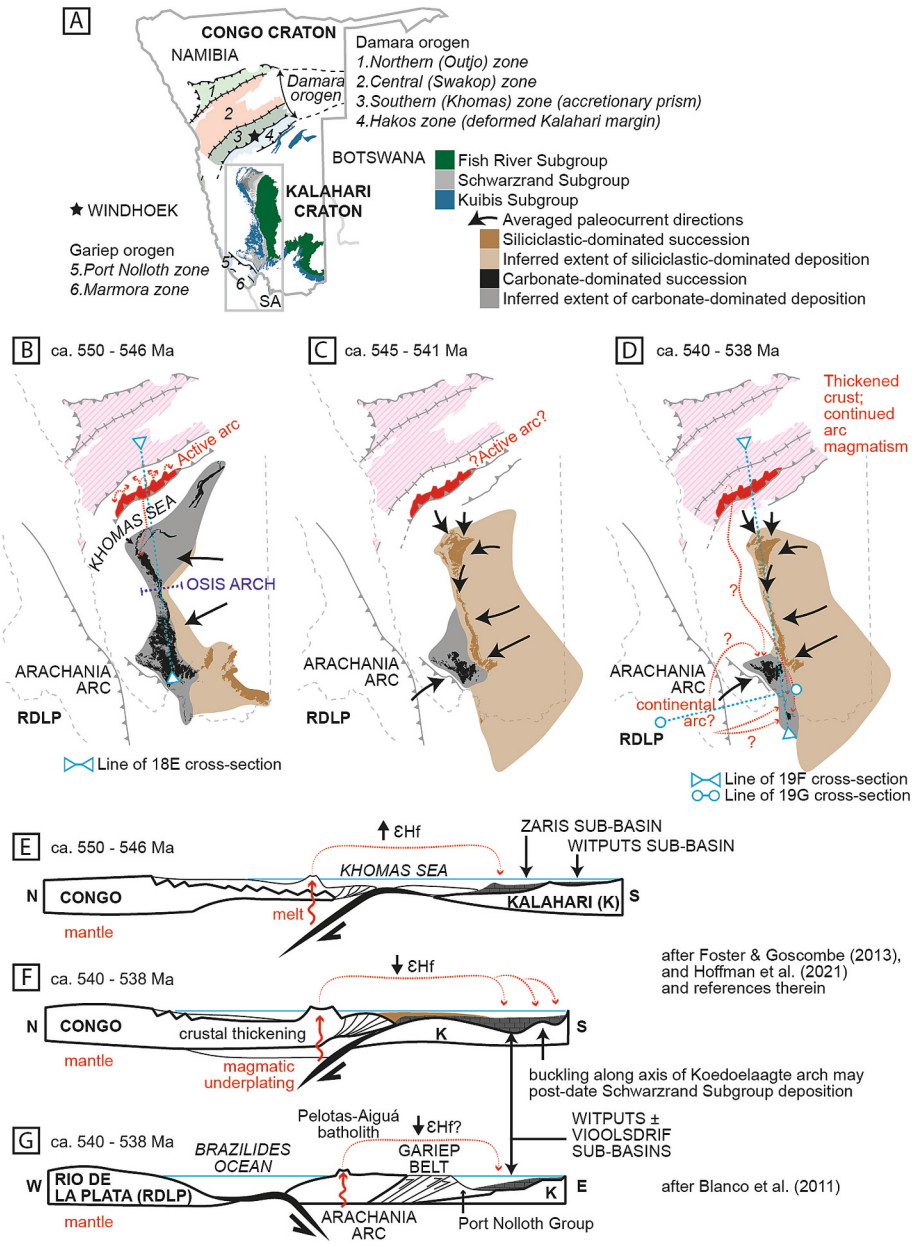

Fig. 19. **(A)** Preserved structure and subdivision of the Damara and Gariep orogenic belts, and the Nama foreland basin (after Germs, 1983; Hoffman et al., 2021 and references therein). **(B)** to **(G)** Interpretation of the tectonic evolution of the Nama foreland basin (modified after Miller, 2008; Blanco et al., 2009, Blanco et al., 2011; Foster and Goscombe, 2013; Hoffman et al., 2021). **(B)** Initial Damara collision along the Kalahari margin recorded in the Swakop zone (e.g., de Kock et al., 2000) accompanied by the development of an oceanic arc that supplied ash material during deposition of the Hoogland Member at ca. 547 Ma. **(C)** Progressive collision along the Damara orogeny resulted in migration of the flexural foredeep into the Witputs sub-basin and eventual uplift and erosion of the arc recorded by detrital chromian spinels and associated paleocurrent data (Germs, 1983; Blanco et al., 2009). Zaris sub-basin infill and foredeep migration also resulted in progressive southward-directed carbonate platform migration. **(D)** Progressive underplating of the Damara belt recorded by the shift in zircon εHf away from depleted mantle composition by ca. 540 Ma. Carbonate platform migration continues southward thereafter. **(E)**–**(F)** Idealized N-S Cross-sections illustrate closure of the Khomas seaway and flexural subsidence of the Zaris sub-basin during collision between the Congo and Kalahari cratons and progressive underplating associated with ongoing collision and migration of major flexural subsidence into the Witputs sub-basin during Schwarzrand Subgroup deposition. **(G)** Cross-section of the hypothesized tectonic structure of the Gariep orogenic belt (after Blanco et al., 2011). RDLP – Rio de la Plata craton.

ages, all models support initiation of carbonate deposition in sections along the Orange River prior to ca. 539.6 Ma (Fig. 20D; Nelson et al., 2022), and all models support the youngest carbonate deposition occurring on the NNP, consistent with available ash bed ages (Nelson et al., 2022). All models thereby appear to corroborate and temporally calibrate a dynamic model of carbonate platform migration driven by the southward migration of the main flexural foredeep, as initially reconstructed through detailed foundational stratigraphic logging and geological mapping (Germs and Gresse, 1991; Gresse and Germs, 1993).

6. Conclusions

New and published zircon U-Pb CA-ID-TIMS ages of tuff deposits in the Swartpunt area (southern Namibia), which are interbedded in the Schwarzrand Subgroup of the Nama Group, show systematic younging-upwards repetition, within analytical uncertainty, whereby the sequence of ages in the lower-middle interval of the Spitskop Member is repeated by ash beds in the upper part of the Spitskop Member of the Swartpunt Hill type section. This may be resolved in two independent

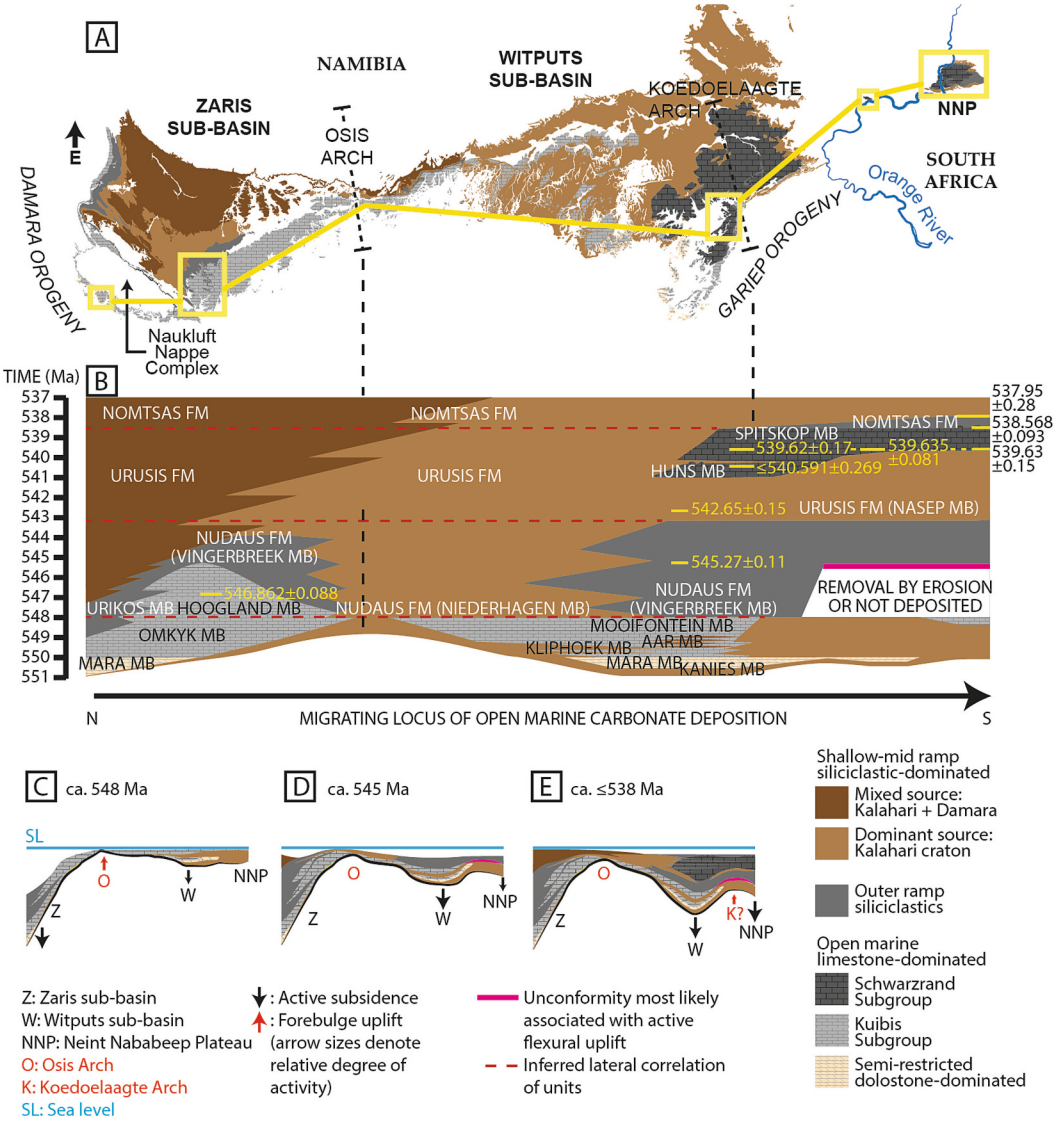

Fig. 20. Map view and cross-section of preserved Nama Group deposits from the Zaris and Witputs sub-basins. **(A)** Map of dominantly Ediacaran portions of the Nama Group (Kuibis and Schwarzrand Subgroups), showing the profile used in construction of simplified cross-sections and key regions used to reconstruct maximum stratigraphic thicknesses. **(B)** Cross-section reconstructed in the time domain, using a selection of key radioisotopic data from Nelson et al. (2022) and this study. This reconstruction assumes that the weighted mean age of the ash bed in core 1B represents a near-depositional age (but see discussion section 5.2.1). Detailed composite stratigraphic columns and full details are provided in Figs. S1 and S2. **(C)**–**(E)** Snapshots of evolving foredeep bathymetry along an idealized N-S cross-section at ca. 548 Ma, ca. 545 Ma and 538 Ma. Note extreme vertical exaggeration. Vertical arrows denote relative degrees of flexural subsidence and uplift associated with ongoing Damara compression. Timing of onset of flexural buckling along axis of the Koedoelaagte arch remains unclear but occurred prior to deposition of the lower part of the Fish River Subgroup based on southward overstepping of progressively older Nama units and unconformities by the Inachab Member of the Fish River Subgroup to the north of Koedoelaagte (Germs and Gresse, 1991; Gresse and Germs, 1993). Fm. – Formation; Mb. – Member.

ways. Either the majority of ages in this area reflect maximum depositional ages due to either pervasive inheritance or analytical biases (Scenario 1), or they correspond to depositional ages if a cryptic displacement related to Gariep compression led to the repetition of a part of the sedimentary succession in this area (Scenario 2). A corollary of Scenario 1 would be to invoke maximum depositional ages for all weighted mean tuff bed ages, which would have significant ramifications for global chronostratigraphy throughout the geologic record. Both scenarios warrant careful consideration in future studies but aspects that are common to both allow for a coherent reconstruction of the basin-wide depositional history of the Ediacaran portion of the Nama Group. Lastly, we propose that future studies aim to supply images of all individual zircon grains as supplementary metadata, which will aid future statistical investigations that aim to standardize inter-laboratory optical zircon selection criteria for the identification of autocrystic populations.

Our new data, alongside a compilation of published geochronological, litho- and chemostratigraphic data, show the influence of Damara-related orogenesis on Nama Group sedimentation. The onset of collision between the Swakop zone and Kalahari craton was associated with arc volcanism, development of the Khomas accretionary prism, and flexural subsidence of the Zaris sub-basin. Progressive collision led to gradual underplating of the Damara orogen and southward-directed migration of the locus of carbonate platform development. Flexural subsidence driven by Gariep orogenic compression was most pronounced during deposition of the Nudaus and Urusis Formations in the Swartpunt area and in sections exposed along the Orange River, of which the latter record a later pulse of accommodation space increase that documents progressive southward migration of active subsidence associated with zip-like closure of the Adamastor seaway. Together, this compilation temporally calibrates dynamic carbonate platform migration

isochronous with reconstructed pulses of basin-wide flexural subsidence during the amalgamation of southern Gondwana.

Thanks

We thank Lothar Gessert and Hennie Joubert for site access and Helke Mocke for contact support at the Namibian Geological Survey. MO thanks Lela and Bernd Roemer for the exceptionally comfortable stay in the field. We thank Melanie Mesli for GRIND-ECT database management, and U. Baranowski and S. Brooks for technical support. FB thanks Charlie (Karl-Heinz) Hoffmann, Taufeeq Dhansay, Tony Prave, Elias Rugen, Eric Breard, Florian Fusseis and Brennan O'Connell for enlightening discussions that helped to focus several aspects of the paper. M.O. and F.B. thank Urs Schaltegger for helpful suggestions on an earlier version of the manuscript. We thank members of the GRIND-ECT geochronology group. Lastly, we thank thoughtful and constructive reviews on earlier versions of the manuscript by Lyle Nelson, Andrey Bekker and three anonymous reviewers, as well as Neil Griffis, Alex Liu and Patricia Vickers-Rich, each of whom helped to greatly improve the manuscript. Any use of trade, firm, or product names is for descriptive purposes only and does not imply endorsement by the U.S. Government.

Declaration of competing interest

The authors declare that they have no known competing financial interests or personal relationships that could have appeared to influence the work reported in this paper.

Acknowledgements

Funding. MO and FM acknowledge funding from Swiss National Science Foundation grant 200021_182556. FB and RW acknowledge support from the Natural Environment Research Council (NERC grant NE/T008458/1). FB acknowledges support from UKRI Project EP/Y008790/1. BM acknowledges support from Genus: DSI-NRF Centre of Excellence in Palaeoscience under Grant No. 86073.

Appendix A. Supplementary data

Supplementary data to this article can be found online at https://doi.org/10.1016/j.earscirev.2025.105169.

Data availability

All new data are available in the Supplementary Materials.

References

Adams, E.W., Schroder, S., Grotzinger, J.P., McCormick, D.S., 2004. Digital Reconstruction and Stratigraphic Evolution of a Microbial-Dominated, Isolated Carbonate Platform (Terminal Proterozoic, Nama Group, Namibia). J. Sediment. Res. 74 (4), 479–497.

Adams, E.W., Grotzinger, J.P., Watters, W.A., Schroder, S., McCormick, D.S., Al-Siyabi, H.A., 2005. Digital characterization of thrombolite-stromatolite reef distribution in a carbonate ramp system (Terminal Proterozoic, Nama Group, Namibia). Am. Assoc. Pet. Geol. Bull. 89 (10), 1293–1318.

Bally, A.W., Gordy, P.L., Stewart, G.A., 1966. Structure, seismic data, and orogenic evolution of southern Canadian Rocky Mountains. Bull. Can. Petrol. Geol. 14 (3), 337–381.

Barnes, S., Sawyer, E., 1980. An alternative model for the Damara mobile belt: Ocean crust subduction and continental convergence. Precambrian Res. 13, 297–336.

Blanco, G., Rajesh, H.M., Germs, G.J.B., Zimmermann, U., 2009. Chemical composition and tectonic setting of chromian spinels from the Ediacaran-early Paleozoic Nama Group, Namibia. J. Geol. 117 (3), 325–341.

Blanco, G., Germs, G.J.B., Rajesh, H.M., Chemale, F., Dussin, I.A., Justino, D., 2011. Provenance and paleogeography of the Nama Group (Ediacaran to early Palaeozoic, Namibia): Petrography, geochemistry and U-Pb detrital zircon geochronology. Precambrian Res. 187, 15–32.

Bowring, S.A., Grotzinger, J.P., Condon, D.J., Ramezani, J., Newall, M.J., Allen, P.A., 2007. Geochronologic constraints on the chronostratigraphic framework of the Neoproterozoic Huqf Supergroup, Sultanate of Oman. Am. J. Sci. 307, 1097–1145.

Bowring, J.F., McLean, N.M., Bowring, S.A., 2011. Engineering cyber infrastructure for U-Pb geochronology: Tripoli and U-Pb Redux. Geochem. Geophys. Geosyst. 12 (6), 1–19.

Bowyer, F.T., Zhuravlev, A.Yu., Wood, R., Shields, G.A., Curtis, A., Poulton, S.W., Condon, D.J., Yang, C., Zhu, M., 2022. Calibrating the temporal and spatial dynamics of the Ediacaran-Cambrian radiation of animals. Earth Sci. Rev. 225, 103913.

Bowyer, F.T., Uahengo, C.-I., Kaputuaza, K., Ndeunyema, J., Yilales, M., Alexander, R.D., Curtis, A., Wood, R.A., 2023. Constraining the onset and environmental setting of metazoan biomineralization: the Ediacaran Nama Group of the Tsaus Mountains, Namibia. Earth Planet. Sci. Lett. 620, 118336.

Bowyer, F.T., Wood, R.A., Yilales, M., 2024. Sea level controls on Ediacaran-Cambrian animal radiations. Sci. Adv. 10 (31), eado6462.

Buatois, L.A., Almond, J., Mángano, M.G., Jensen, S., Germs, G.J.B., 2018. Sediment disturbance by Ediacaran bulldozers and the roots of the Cambrian explosion. Sci. Rep. 8 (1), 1–9.

Condon, D.J., Schoene, B., McLean, N.M., Bowring, S.A., Parrish, R.R., 2015. Metrology and traceability of U-Pb isotope dilution geochronology (EARTHTIME Tracer Calibration Part I). Geochim. Cosmochim. Acta 164, 464–480.

Condon, D., Schoene, B., Schmitz, M., Schaltegger, U., Ickert, R.B., Amelin, Y., Augland, L.E., Chamberlain, K.R., Coleman, D.S., Connelly, J.N., Corfu, F., Crowley, J.L., Davies, J.H.F.L., Denyszyn, S.W., Eddy, M.P., Gaynor, S.P., Heaman, L. M., Huyskens, M.H., Kamo, S., Kasbohm, J., Keller, C.B., MacLennan, S.A., McLean, N.M., Noble, S., Ovtcharova, M., Paul, A., Ramezani, J., Rioux, M., Sahy, D., Scoates, J.S., Szymanowski, D., Tapster, S., Tichomirowa, M., Wall, C.J., Wotzlaw, J.-F., Yang, C., Yin, Q.-Z., 2024. Recommendations for the reporting and interpretation of isotope dilution U-Pb geochronological information. Geol. Soc. Am. Bull. 136 (9/10), 4233–4251.

Cribb, A.T., Kenchington, C.G., Koester, B., Gibson, B.M., Boag, T.H., Racicot, R.A., Mocke, H., Laflamme, M., Darroch, S.A.F., 2019. Increase in metazoan ecosystem engineering prior to the Ediacaran–Cambrian boundary in the Nama Group, Namibia. R. Soc. Open Sci. 6, 190548.

Crisp, L.J., Berry, A.J., 2022. A new model for zircon saturation in silicate melts. Contrib. Mineral. Petrol. 177, 71.

Darroch, S.A.F., Sperling, E.A., Boag, T.H., Racicot, R.A., Mason, S.J., Morgan, A.S., Tweedt, S., Myrow, P., Johnston, D.T., Erwin, D.H., Laflamme, M., 2015. Biotic replacement and mass extinction of the Ediacara biota. Proc. R. Soc. B Biol. Sci. 282 (1814), 20151003.

Darroch, S.A.F., Smith, E.F., Laflamme, M., Erwin, D.H., 2018. Ediacaran Extinction and Cambrian Explosion. Trends Ecol. Evol. 33, 653–663.

Darroch, S.A.F., Cribb, A.T., Buatois, L.A., Germs, G.J.B., Kenchington, C.G., Smith, E.F., Mocke, H., O'Neil, G.R., Schiffbauer, J.D., Maloney, K.M., Racicot, R.A., Turk, K.A., Gibson, B.M., Almond, J., Koester, B., Boag, T.H., Tweedt, S.M., Laflamme, M., 2021. The trace fossil record of the Nama Group, Namibia: Exploring the terminal Ediacaran roots of the Cambrian explosion. Earth Sci. Rev. 212, 103435.

Darroch, S.A., Smith, E.F., Nelson, L.L., Craffey, M., Schiffbauer, J.D., Laflamme, M., 2023. Causes and consequences of end-Ediacaran extinction: an update. Cambridge Prisms: Extinct. 1, e15.

de Kock, G.S., Eglington, B., Armstrong, R.A., Harmer, R.E., Walraven, F., 2000. U-Pb and Pb-Pb ages of the Naauwpoort rhyolite, Kawakeup leptite and Okongava Diorite: implications for the onset of rifting and of orogenesis in the Damara belt, Namibia. Communicat. Geol. Surv. Namibia 12, 81–88.

Dibenedetto, S., Grotzinger, J., 2005. Geomorphic evolution of a storm-dominated carbonate ramp (c. 549 Ma), Nama Group, Namibia. Geol. Mag. 142 (5), 583–604.

Elliott, D.A., Vickers-Rich, P., Trusler, P., Hall, M., 2011. New evidence on the taphonomic context of the Ediacaran *Pteridinium*. Acta Palaeontol. Pol. 56, 641–650.

Elliott, D.A., Trusler, P.W., Narbonne, G.M., Vickers-Rich, P., Morton, N., Hall, M., Hoffmann, K.H., Schneider, G.I.C., 2016. *Ernietta* from the late Edicaran Nama Group, Namibia. J. Paleontol. 90 (6), 1017–1026.

Eychenne, J., Engwell, S.L., 2022. The grainsize of volcanic fall deposits: Spatial trends and physical controls. Geol. Soc. Am. Bull. 135 (7/8), 1844–1858.

Fedonkin, M.A., Gehling, J.G., Grey, K., Narbonne, G.M., Vickers-Rich, P., 2007. The Rise of Animals. Evolution and Diversification of the Kingom Animalia. Johns Hopkins University Press, Baltimore, p. 326.

Foster, D.A., Goscombe, B.D., 2013. Continental Growth and Recycling in Convergent Orogens with large Turbidite fans on Oceanic Crust. Geosciences 3, 354–388.

Gaynor, S.P., Ruiz, M., Schaltegger, U., 2022. The importance of high-precision in the evaluation of U-Pb zircon age spectra. Chem. Geol. 603, 120913.

Gaynor, S.P., Smith, T.M., Schaltegger, U., 2023. Tracing magmatic genesis and evolution through single zircon crystals from successive supereruptions from the Socorro Caldera complex, USA. Earth Planet. Sci. Lett. 616, 118236.

Germs, G.J., 1972. New shelly fossils from the Nama Group, South-West Africa. Am. J. Sci. 272, 752–761.

Germs, G.J.B., 1973. A reinterpretation of *Rangea schneiderhoehni* and the discovery of a related new fossil from the Nama Group, South West Africa. Lethaia 6 (1), 1–9.

Germs, G.J.B., 1983. Implications of a sedimentary facies and depositional environmental analysis of the Nama Group in South West Africa/Namibia. Special Publicat. Geolog. Soc. South Africa 11, 89–114.

Germs, G.J.B., Gaucher, C., 2012. Nature and extent of a late Ediacaran (ca. 547 Ma) glacigenic erosion surface in southern Africa. S. Afr. J. Geol. 115, 91–102.

Germs, G.J.B., Gresse, P.G., 1991. The foreland basin of the Damara and Gariep orogens in Namaqualand and southern Namibia: stratigraphic correlations and basin dynamics. S. Afr. J. Geol. 94 (2/3), 159–169.

Germs, G.J.B., Miller, R.M.G., Frimmel, H.E., Gaucher, C., 2009. Chapter 5.4 Syn- to Late-Orogenic Sedimentary Basins of Southwestern Africa. In: Developments in Precambrian Geology. Elsevier.

Geyer, G., 2005. The fish River Subgroup in Namibia: Stratigraphy, depositional environments and the Proterozoic-Cambrian boundary problem revisited. Geol. Mag. 142, 465–498.
Gong, Z., Baillie, I., Nelson, L.L., Gerasimov, S.H., Rose, C., Smith, E.F., 2025. Magnetic susceptibility cyclostratigraphy of the lower Schwarzrand Subgroup in southern Namibia refines temporal calibration of late Ediacaran bilaterian radiation. Glob. Planet. Chang. 245, 104668.
Grazhdankin, D., Seilacher, A., 2002. Underground Vendobionta from Namibia. Palaeontology 45 (1), 57–78.
Gresse, P.G., Germs, G.J.B., 1993. The Nama foreland basin: sedimentation, major unconformity bounded sequences and multisided active margin advance. Precambrian Res. 63, 247–272.
Grotzinger, J.P., 2000. Facies and paleoenvironmental setting of Thrombolite-Stromatolite Reefs, Terminal Proterozoic Nama Group (ca. 550–543 Ma), central and southern Namibia. Communicat. Geol. Surv. Namibia 12, 251–264.
Grotzinger, J.P., Bowring, S.A., Saylor, B.Z., Kaufman, A.J., 1995. Biostratigraphic and Geochronologic Constraints on early Animal Evolution. Science 270, 598–604.
Grotzinger, J.P., Watters, W.A., Knoll, A.H., 2000. Calcified metazoans in thrombolite-stromatolite reefs of the terminal Proterozoic Nama Group, Namibia. Paleobiology 26, 334–359.
Gürich, G., 1930a. Die bislang ältesten Spuren von Organismen in Südafrika. Int. Geol. Congr. South Africa 15, 670–680.
Gürich, G., 1930b. Uber den Kuibisquartzit in Südwest-Afrika. Z. Dtsch. Geol. Ges. 82, 637.
Gürich, G., 1933. Die Kuibis-Fossillien der Nama-Formation von Südwestafrika. Paläontol. Z. 15, 137–154.
Hahn, G., Pflug, H., 1985. Polypenartige Organismen aus dem Jung-Prakambrium (Nama-Gruppe) von Namibia. Geol. Palaeontol. 19, 1–13.
Hall, M., Kaufman, A.J., Vickers-Rich, P., Ivantsov, A., Trusler, P., Linnemann, U., Hofmann, M., Elliott, D., Cui, H., Fedonkin, M., Hoffmann, K.H., Wilson, S.A., Schneider, G., Smith, J., 2013. Stratigraphy, palaeontology and geochemistry of the late Neoproterozoic Aar Member, Southwest Namibia: reflecting environmental controls on Ediacara fossil preservation during the terminal Proterozoic in African Gondwana. Precambrian Res. 238, 214–232.
Haslett, J., Parnell, A., 2008. A simple monotone process with application to radiocarbon-dated depth chronologies. J. R. Stat. Soc.: Ser. C: Appl. Stat. 57 (4), 399–418.
Hiess, J., Condon, D.J., McLean, N., Noble, S.R., 2012. $^{238}U/^{235}U$ systematics in terrestrial uranium-bearing minerals. Science 335, 1610–1614.
Hodgin, E.B., Nelson, L.L., Wall, C.J., Barrón-Díaz, A.J., Webb, L.C., Schmitz, M.D., Fike, D.A., Hagadorn, J.W., Smith, E.F., 2020. A link between rift-related volcanism and end-Ediacaran extinction? Integrated chemostratigraphy, biostratigraphy, and U-Pb geochronology from Sonora, Mexico. Geology 49, 115–119.
Hoffman, P.F., Halverson, G.P., Schrag, D.P., Higgins, J.A., Domack, E.W., Macdonald, F. A., Pruss, S.B., Blättler, C.L., Crockford, P.W., Hodgin, E.B., Bellefroid, E.J., Johnson, B.W., Hodgskiss, M.S.W., Lamothe, K.G., LoBianco, S.J.C., Busch, J.F., Howes, B.J., Greenman, J.W., Nelson, L.L., 2021. Snowballs in Africa: sectioning a long-lived Neoproterozoic carbonate platform and its bathyal foreslope (NW Namibia). Earth Sci. Rev. 219, 103616.
Jaffey, A.H., Flynn, K.F., Glendenin, L.E., Bentley, W.C., Essling, A.M., 1971. Precision measurement of half-lives and specific activities of ^{235}U and ^{238}U. Phys. Rev. C: Coveri. Nuclear Phys. 4, 1889–1906.
Jensen, S., Saylor, B.Z., Gehling, J.G., Germs, G.J.B., 2000. Complex trace fossils from the terminal Proterozoic of Namibia. Geology 28, 143–146.
Johnson, S.D., Poujol, M., Kisters, A.F.M., 2006. Constraining the timing and migration of collisional tectonics in the Damara Belt, Namibia: U-Pb zircon ages for the syntectonic Salem-type Stinkbank granite. S. Afr. J. Geol. 109, 611–624.
Kaufman, A.J., Kriesfeld, L., Vickers-Rich, P., Narbonne, G., 2019. When life got hard: an environmental driver for metazoan biomineralization. Estud. Geol. 75, e101.
Keller, C.B., Schoene, B., Samperton, K.M., 2018. A stochastic sampling approach to zircon eruption age interpretation. Geochem. Perspect. Lett. 8, 31–35.
Knoll, A.H., Carroll, S.B., 1999. Early animal evolution: emerging views from comparative biology and geology. Science 284, 2129–2137.
Kröner, A., Germs, G.J.B., 1971. A re-interpretation of the Numees-Nama contact at Aussenkjer, South West Africa. Trans. Geol. Soc. South Africa 74 (2), 69–74.
Linnemann, U., Ovtcharova, M., Schaltegger, U., Gärtner, A., Hautmann, M., Geyer, G., Vickers-Rich, P., Rich, T., Plessen, B., Hofmann, M., Zieger, J., Krause, R., Kriesfeld, L., Smith, J., 2019. New high-resolution age data from the Ediacaran-Cambrian boundary indicate rapid, ecologically driven onset of the Cambrian explosion. Terra Nova 31, 49–58.
Maloney, K.M., Boag, T.H., Facciol, A.J., Gibson, B.M., Cribb, A., Koester, B.E., Kenchington, C.G., Racicot, R.A., Darroch, S.A.F., Laflamme, M., 2020. Palaeoenvironmental analysis of *Ernietta*-bearing Ediacaran deposits in southern Namibia. Palaeogeogr. Palaeoclimatol. Palaeoecol. 556, 109884.
Maloof, A.C., Ramezani, J., Bowring, S.A., Fike, D.A., Porter, S.M., Mazouad, M., 2010a. Constraints on early Cambrian carbon cycling from the duration of the Nemakit-Daldynian–Tommotian boundary $\delta^{13}C$ shift, Morocco. Geology 38, 623–626.
Maloof, A.C., Porter, S.M., Moore, J.L., Dudás, F.Ö., Bowring, S.A., Higgins, J.A., Fike, D. A., Eddy, M.P., 2010b. The earliest Cambrian record of animals and ocean geochemical change. Geol. Soc. Am. Bull. 122, 1731–1774.
Mattinson, J.M., 2005. Zircon U-Pb chemical abrasion ("CA-TIMS") method: combined annealing and multi-step partial dissolution analysis for improved precision and accuracy of zircon ages. Chem. Geol. 220, 47–66.
McKanna, A.J., Koran, I., Schoene, B., Ketcham, R.A., 2022. Chemical abrasion: the mechanics of zircon dissolution. Geochronology 5, 127–151.
McLean, N.M., Condon, D.J., Schoene, B., Bowring, S.A., 2015. Evaluating uncertainties in the calibration of isotopic reference materials and multi-element isotopic tracers (EARTHTIME Tracer Calibration Part II). Geochim. Cosmochim. Acta 164, 481–501.
Meyer, M., Elliott, D., Schiffbauer, J.D., Hall, M., Hoffman, K.H., Schneider, G., Vickers-Rich, P., Xiao, S., 2014. Taphonomy of the Ediacaran fossil *Pteridinium simplex* preserved three-dimensionally in mass flow deposits, Nama Group, Namibia. J. Paleontol. 88 (2), 240–252.
Miller, R.McG, 2008. Neoproterozoic to lower Paleozoic. In: The Geology of Namibia. Geological Survey of Namibia, Windhoek.
Mtonda, M.T., Le Roux, P., Taylor, W.L., Wilton, A., Tostevin, R., 2024. High resolution strontium isotope data from Nama Group, South Africa, constrain global stratigraphic relationships in the terminal Ediacaran. Precambrian Res. 404, 107339.
Narbonne, G.M., Saylor, B.Z., Grotzinger, J.P., 1997. The youngest Ediacaran fossils from southern Africa. J. Paleontol. 71, 953–967.
Nelson, L.L., Ramezani, J., Almond, J.E., Darroch, S.A.F., Taylor, W.L., Brenner, D.C., Furey, R.P., Turner, M., Smith, E.F., 2022. Pushing the boundary: A calibrated Ediacaran-Cambrian stratigraphic record from the Nama Group in northwestern Republic of South Africa. Earth Planet. Sci. Lett. 580, 117396.
Nelson, L.L., Crowley, J.L., Smith, E.F., Schwartz, D.M., Hodgin, E.B., Schmitz, M.D., 2023. Cambrian explosion condensed: High-precision geochronology of the lower Wood Canyon Formation, Nevada. Proc. Natl. Acad. Sci. USA 120, e2301478120.
Nowell, G.M., Kempton, P.D., Noble, S.R., Fitton, J.G., Saunders, A.D., Mahoney, J.J., Taylor, R.N., 1998. High precision Hf isotope measurements of MORB and OIB by thermal ionisation mass spectrometry: insights into the depleted mantle. Chem. Geol. 149 (3–4), 211–233.
O'Connell, B., McMahon, W.J., Nduutepo, A., Pokolo, P., Mocke, H., McMahon, S., Boddy, C.E., Liu, A.G., 2025. Transport of 'Nama'-type biota in sediment gravity and combined flows: Implications for terminal Ediacaran palaeoecology. Sedimentology 72 (2), 365–407.
Parnell, A.C., Haslett, J., Allen, J.R., Buck, C.E., Huntley, B., 2008. A flexible approach to assessing synchroneity of past events using Bayesian reconstructions of sedimentation history. Quat. Sci. Rev. 27 (19–20), 1872–1885.
Parry, L.A., Boggiani, P.C., Condon, D.J., Garwood, R.J., Leme, J.D.M., McIlroy, D., Brasier, M.D., Trindade, R., Campanha, G.A.C., Pacheco, M.L.A.F., Diniz, C.Q.C., Liu, A.G., 2017. Ichnological evidence for meiofaunal bilaterians from the terminal Ediacaran and earliest Cambrian of Brazil. Nat. Ecol. & Evolut. 1, 1455–1464.
Penny, A.M., Wood, R., Curtis, A., Bowyer, F., Tostevin, R., Hoffman, K.-H., 2014. Ediacaran metazoan reefs from the Nama Group, Namibia. Science 344 (6191), 1504–1506.
Pflug, H.D., 1966. Neue Fossilreste aus den Nama-Schichten in Südwest-Afrika. Paläontol. Z. 40, 14–25.
Pflug, H.D., 1970. Zur fauna der Nama-Schichten in Südwest-Afrika; I. Pteridinia, Bau und systematische Zugehörigkeit. Palaeontogr. Abt. A 134, 226–262.
Rose, C.V., Prave, A.R., Bergmann, K.D., Condon, D.J., Kasemann, S.A., Macdonald, F.A., Hoffmann, K.-H., Trindade, R.I.F., Zhu, M., 2019. Project Report: Grinding through the Ediacaran-Cambrian transition. Communicat. Geol. Surv. Namibia 21, 1–14.
Runnegar, B., Gehling, J.G., Horodyski, R.J., Jensen, S., Knauth, L.P., 1995. Base of the Sauk sequence is a global eustatic event that lies just above the Precambrian-Cambrian boundary. Geol. Soc. America, Abstract. Prog. 270, A-330.
Runnegar, B., Gehling, J.G., Jensen, S., Saltzman, N.R., 2024. Ediacaran paleobiology and biostratigraphy of the Nama Group, Namibia, with emphasis on the erniettomorphs, tubular and trace fossils, and a new sponge, *Arimasia germsi* n. gen. n. sp. J. Paleontol. 98, 1–59.
Saylor, B.Z., 1993. Report: Progress report on the sedimentology and stratigraphy of the Kuibis and Schwarzrand Subgroups, Witputs area, southwestern Namibia. Communicat. Geol. Surv. Namibia 8, 137–146.
Saylor, B.Z., 1996. Sequence Stratigraphic and Chemostratigraphic Constraints on the Evolution of the Terminal Proterozoic to Cambrian Nama Basin, Namibia. Ph.D. Thesis,. Massachusetts Institute of Technology, p. 355.
Saylor, B.Z., 2003. Sequence stratigraphy and carbonate-siliciclastic mixing in a terminal Proterozoic foreland basin, Urusis Formation, Nama Group, Namibia. J. Sediment. Res. 73, 264–279.
Saylor, B.Z., Grotzinger, J.P., 1996. Reconstruction of important Proterozoic-Cambrian boundary exposures through the recognition of thrust deformation in the Nama Group of southern Namibia. Communicat. Geol. Surv. Namibia 11, 1–12.
Saylor, B.Z., Grotzinger, J.P., Germs, G.J.B., 1995. Sequence stratigraphy and sedimentology of the Neoproterozoic Kuibis and Schwarzrand Subgroups (Nama Group), southwestern Namibia. Precambrian Res. 73, 153–171.
Saylor, B.Z., Kaufman, A.J., Grotzinger, J.P., Urban, F., 1998. A composite reference section for terminal Proterozoic strata of southern Namibia. J. Sediment. Res. 68, 1223–1235.
Saylor, B.Z., Poling, J.M., Huff, W.D., 2005. Stratigraphic and chemical correlation of volcanic ash beds in the terminal Proterozoic Nama Group, Namibia. Geol. Mag. 142, 519–538.
Schaltegger, U., Schmitt, A.K., Horstwood, M.S.A., 2015. U-Th-Pb zircon geochronology by ID-TIMS, SIMS, and laser ablation ICP-MS: Recipes, interpretations, and opportunities. Chem. Geol. 402, 89–110.
Schoene, B., Crowley, J.L., Condon, D.J., Schmitz, M.D., Bowring, S.A., 2006. Reassessing the uranium decay constants for geochronology using ID-TIMS U-Pb data. Geochim. Cosmochim. Acta 70, 426–445.
Sláma, J., Condon, D.J., Crowley, J.L., Gerdes, A., Hanchar, J.M., Horstwood, M.S.A., Morris, G.A., Nasdala, L., Norberg, N., Schaltegger, U., Schoene, B., Tubret, M.N., Whitehouse, M.J., 2008. Plešovice zircon—a new natural reference material for U–Pb and Hf isotopic microanalysis. Chem. Geol. 249 (1–2), 1–35.
Sloss, L.L., 1963. Sequences in the cratonic interior of North America. Geol. Soc. Am. Bull. 74, 93–114.

Smith, O., 1999. Terminal Proterozoic Carbonate Platform Development: Stratigraphy and Sedimentology of the Kuibis Subgroup (Ca. 550–548 Ma), Northern Nama Basin, Namibia. Unpublished Masters Thesis. Massachusetts Institute of Technology.
Smith, E.F., Nelson, L.L., Strange, M.A., Eyster, A.E., Rowland, S.M., Schrag, D.P., Macdonald, F.A., 2016. The end of the Ediacaran: two new exceptionally preserved body fossil assemblages from Mount Dunfee, Nevada, USA. Geology 44, 911–914.
Spiering, B.R., Bissick, A., Darroch, S.A.F., Davies, J.H., Gibson, B.M., Halverson, G.P., Laflamme, M., Hilgen, F.J., 2023. Initial cyclostratigraphy of the middle Nama Group (Schwarzrand Subgroup) in southern Namibia. Precambrian Res. 397, 107200.
Spötl, C., Vennemann, T.W., 2003. Continuous-flow isotope ratio mass spectrometric analysis of carbonate minerals. Rapid Commun. Mass Spectrom. 17, 1004–1006.
Topper, T., Betts, M.J., Dorjnamjaa, D., Li, G., Li, L., Altanshagai, G., Enkhbaatar, B., Skovsted, C.B., 2022. Locating the BACE of the Cambrian: Bayan Gol in southwestern Mongolia and global correlation of the Ediacaran-Cambrian boundary. Earth Sci. Rev. 229, 104017.
Turk, K.A., Maloney, K.M., Laflamme, M., Darroch, S.A., 2022. Paleontology and ichnology of the late Ediacaran Nasep–Huns transition (Nama Group, southern Namibia). J. Paleontol. 96, 753–769.
Turk, K.A., Wehrmann, A., Laflamme, M., Darroch, S.A.F., 2024. Priapulid neoichnology, ecosystem engineering, and the Ediacaran-Cambrian transition. Palaeontology 67 (4), e12721.
Vickers-Rich, P., Ivantsov, A.Yu., Trusler, P.W., Narbonne, G.M., Hall, M., Wilson, S.A., Greentree, C., Fedonkin, M.A., Elliott, D.A., Hoffmann, K.H., Schneider, G.I.C., 2013. Reconstructing *Rangea*: new discoveries from the Ediacaran of southern Namibia. J. Paleontol. 87, 1–15.
Wendt, I., Carl, C., 1991. The statistical distribution of the mean squared weighted deviation. Chem. Geol.: Isotope Geosci. Sect. 86 (4), 275–285.
Widmann, P., Davies, J.H., Schaltegger, U., 2019. Calibrating chemical abrasion: its effects on zircon crystal structure, chemical composition and UPb age. Chem. Geol. 511, 1–10.
Wilson, J.P., Grotzinger, J.P., Fischer, W.W., Hand, K.P., Jensen, S., Knoll, A.H., Abelson, J., Metz, J.M., McLoughlin, N., Cohen, P.A., Tice, M.M., 2012. Deep-water incised valley deposits at the Ediacaran – Cambrian boundary in southern Namibia contain abundant *Treptichnus pedum*. Palaios 27, 252–273.
Wood, R.A., Poulton, S.W., Prave, A.R., Hoffmann, K.-H., Clarkson, M.O., Guilbaud, R., Lyne, J.W., Tostevin, R., Bowyer, F., Penny, A.M., Curtis, A., Kasemann, S.A., 2015. Dynamic redox conditions control late Ediacaran metazoan ecosystems in the Nama Group, Namibia. Precambrian Res. 261, 252–271.
Wood, R., Liu, A.G., Bowyer, F., Wilby, P.R., Dunn, F.S., Kenchington, C.G., Cuthill, J.F. H., Mitchell, E.G., Penny, A., 2019. Integrated records of environmental change and evolution challenge the Cambrian Explosion. Nat. Ecol. & Evolut. 3, 528–538)">.
Wood, R., Bowyer, F.T., Alexander, R., Yilales, M., Uahengo, C.I., Kaputuaza, K., Ndeunyema, J., Curtis, A., 2023. New Ediacaran biota from the oldest Nama Group, Namibia (Tsaus Mountains), and re-definition of the Nama Assemblage. Geol. Mag. 160, 1673–1686.
Zhu, M.Y., Babcock, L.E., Peng, S.C., 2006. Advances in Cambrian stratigraphy and paleontology: integrating correlation techniques, paleobiology, taphonomy and paleoenvironmental reconstruction. Palaeoworld 15, 217–222.
Zhu, M., Zhuravlev, A.Y., Wood, R.A., Zhao, F., Sukhov, S.S., 2017. A deep root for the Cambrian explosion: Implications of new bio- and chemostratigraphy from the Siberian Platform. Geology 45, 459–462.
Zieger-Hofmann, M., Zieger, J., Gärtner, A., Mende, K., Sagawe, A., Mocke, H., Mhojeni, K., Marko, L., Albert, R., Gerdes, A., Linnemann, U., 2022. Correlation of Neoproterozoic diamictites in southern Namibia. Earth Sci. Rev. 233, 104159.